Structural Dynamics and Reaction Reversibility of Specific vs. Promiscuous Detoxification Enzymes

Lorela Paco

A dissertation

submitted in partial fulfillment of the

requirements for the degree of

Doctor of Philosophy

University of Washington

2022

Reading Committee:

William Atkins, Chair

Miklos Guttman

Abhinav Nath

Program Authorized to Offer Degree:

Pharmacy - Medicinal Chemistry

University of Washington

Abstract

Structural Dynamics and Reaction Reversibility of Specific vs. Promiscuous Detoxification Enzymes

Lorela Paco

Chair of the Supervisory Committee:
Sid Nelson Endowed Professor William M. Atkins
Medicinal Chemistry

Detoxification enzymes occupy a unique niche in biology. Unlike most enzymes with defined roles in biochemical pathways, detoxification enzymes have evolved to bind and metabolize many chemically unrelated structures – to be promiscuous – rather than to optimize catalysis towards a preferred substrate or set of substrates. It is likely that detoxification enzymes have unique properties that allow them to achieve their remarkable promiscuity. This thesis focuses on understanding some of these properties by contrasting the behavior of two highly promiscuous detoxification enzymes cytochrome P450 3A4 (CYP3A4) and glutathione transferase A1-1 (GSTA1-1) with that of structurally related, substrate-specific counterparts CYP19A1 and GSTA4-4. Two aspects of enzyme behavior are considered: (I) structural dynamics in the absence and presence of ligands, and (II) reversibility of catalysis.

Chapters 2 and 3 describe the substrate-dependent structural dynamics of membrane-embedded CYP3A4 and CYP19A1, respectively, via hydrogen-deuterium exchange mass spectrometry and molecular dynamics simulations. Comparison of the structural dynamics of CYP3A4 bound to eight ligands reveals subtle and ligand-dependent effects on dynamics that are primarily distributed in the flexible regions of the enzyme. No correlation with known ligand properties such as size, binding affinity, and CYP3A4 allosteric function is observed. The dynamic signatures of the two azole-based inhibitors are distinct from the rest of the examined ligands, though a correlation with ligand type needs to be further explored. The largest effects on dynamics are found in the important F-G region and the most typical effect is an increase in dynamics of the F-helix and connecting loops, suggesting a counterintuitive increase in flexibility when CYP3A4 is bound to ligands in a membrane environment.

By contrast, the native steroidal ligand of CYP19A1 causes a clear suppression of dynamics that is most pronounced at the substrate binding site, protein-membrane interface, and access channel. Suppression of dynamics is smaller with two nonsteroidal ligands, particularly at the membrane interface and access channel. The discrimination between the dynamic signatures of CYP19A1 bound to native and nonnative ligands contrasts with the ambiguous small effects observed with CYP3A4 ligands. Collectively, the results are consistent with the substrate selectivity profiles of the two isoforms.

Chapter 4 explores the reversibility of glutathione conjugation to a lipid alkenal substrate by two closely related GST isoforms, GSTA1-1 and GSTA4-4, via ^{1}H NMR, UV-VIS spectroscopy, and LC-MS. Unlike its promiscuous counterpart, GSTA4-4 more readily catalyzes the conjugation reaction of trans-2-nonenal in the reverse direction, introducing a novel differentiating aspect in the catalytic mechanisms of the two isoforms. A speculative implication of the chapter is whether

the reaction reversibility of GSTA4-4 contributes to regulation, in addition to detoxification, of endogenous lipid alkenal products.

TABLE OF CONTENTS

LIST OF FIGURES

LIST OF SUPPORTING FIGURES

LIST OF TABLES

ACKNOWLEDGEMENTS

I am proud to join other Atkins Laboratory alumni in thanking Dr. Bill Atkins for his unwavering support. This work would not have been possible without his mentorship, especially when times were tough.

I would like to thank my dissertation committee for their feedback and for always keeping the door open. Parts of this thesis would not have materialized without Michele Scian and our collaborator John Hackett.

I am thankful for my fellow lab members, as well as the students, postdoctoral fellows, faculty, and staff in the Department of Medicinal Chemistry who have provided a community I cherish.

Finally, I am grateful for my friends and family, especially my parents, who understood the value of higher education and supported me unconditionally in my pursuit to become a scientist.

DEDICATION

To my parents.

Chapter 1. INTRODUCTION

Specificity is the ability of an enzyme to discriminate between any two substrates [1]. High specificity towards substrates is critical, as evidenced by most enzymes acting as specialized catalytic machines with defined physiological roles in biochemical pathways. Growing evidence suggests that the "one sequence – one structure – one function" paradigm is too simplistic, and most, if not all, enzymes are capable of catalyzing promiscuous reactions with nonnative substrates. Although promiscuity has been appreciated as trait of detoxification enzymes for many decades, the contribution of promiscuity to signal transduction, protein folding, and evolution of new protein function has become more clear [2]–[7].

This thesis examines in detail the relationship between protein dynamics, catalytic mechanism, and functional promiscuity for two families of detoxification enzymes, the cytochrome P450s (CYPs) and the glutathione transferases (GSTs). Four enzymes, promiscuous isoforms CYP3A4 and GSTA1-1, and specific counterparts CYP19A1 and GSTA4-4, are chosen as model systems to probe the differences in structural dynamics and catalytic mechanism that differentiate substrate promiscuity and specificity within two distinct enzyme families.

An overview of specificity, promiscuity, and structure-function relationships for CYPs and GSTs is provided below.

1.1 SPECIFICITY AND PROMISCUITY

To best understand the features of enzymes that contribute to promiscuity it is useful to explain the concepts of specificity and promiscuity, and discuss the mechanisms used by enzymes to 'select' their substrates. Note that enzymes and proteins are used interchangeably, unless otherwise stated.

Enzymes are formidable catalysts that accelerate chemical reactions by up to 26 orders of magnitude [8]. The enzyme carbonic anhydrase, termed in the literature as 'evolutionarily perfect', completes 10^4-10^6 reaction cycles per second, accelerating the interconversion of carbon dioxide and water to carbonic acid by a factor of 10^7 compared to the uncatalyzed reaction. The enzymatic decarboxylation of orotidine 5' phosphate (OMP), a key step in the biosynthesis of pyrimidine nucleotides and therefore DNA, proceeds with a half-life of 39 s^{-1}, a dramatic enhancement from the corresponding half-life of 78 million years in the absence of enzyme [9]. Perhaps more impressively, enzymes discriminate between similar reactions and typically fail at accelerating reactions of noncognate substrates. For instance, isoleucyl-tRNA-synthetase binds valine 150 times more weakly than isoleucine, discriminating against lack of one methylene group on valine. Similarly, an alanyl-tRNA-synthetase discriminates against glycine in favor of alanine by a factor of 250 [9].

A definition of enzyme specificity refers to the discrimination by an enzyme between the reactions of two competing substrates. Formally, this is described by the specificity constant or the catalytic efficiency of the enzyme: k_{cat}/K_m. Discrimination between two equimolar competing substrates *A* and *B* is provided by the ratio of their specificity constants [9]:

$$\frac{v_A}{v_B} = \frac{(k_{cat}/K_m)_A \times [A]}{(k_{cat}/K_m)_B \times [B]}$$

where, v = rate of reaction, [A] = concentration of A, [B] = concentration of B.

A more nuanced interpretation of the specificity constant k_{cat}/K_m cautions against it being described simply as the ratio of the catalytic rate (k_{cat}) and the Michaelis Menten constant (K_m). Instead, k_{cat}/K_m should be thought of as a second-order constant that describes the flux of substrates to products and is exponentially related to the energy barrier between the ground state of the free species and the highest energy transition state of the reaction [1], [9], [10]. In other words, k_{cat}/K_m represents the true second-order rate constant of substrate binding to the enzyme multiplied by the probability of being converted to product. It then follows that substrate-specific enzymes have a superior k_{cat}/K_m for their preferred substrate, whereas promiscuous enzymes are expected to have similar k_{cat}/K_m for unrelated substrates [9], [11].

The use of the term ‘promiscuity’ is not restricted to a single definition. Evolutionary biochemists consider an enzyme to be promiscuous if it catalyzes a reaction that is not native to the enzyme’s biological function [2]. A key element of this view is that the promiscuous reaction is not selected by evolution and is therefore an adventitious byproduct, inconsequential to the survival of the organism. Accumulating reports of enzymes catalyzing reactions seemingly unrelated to their native function have established this ‘apparent promiscuity’ to be widespread [3]. In a representative example, a screening of a substrate library against >200 phosphatase enzymes across the haloacid dehalogenase (HAD) superfamily revealed that over 75% of the enzymes used at least 5 substrates [12]. Defining the ‘native’ function of a modern enzyme can be challenging in the absence of historical knowledge of the environment the enzyme was facing at the time it evolved. Therefore, ‘true promiscuity’ according to this view, can be assigned only when the selective pressures that lead to a ‘native’ function are known, such as with *de novo*

designed enzymes evolved in the lab, or when an enzyme metabolizes manmade compounds that are not found in nature, excluding the possibility that such reactions could have been selected for during evolution.

A less restrictive interpretation of promiscuity, and one adopted in this thesis, refers to the ability of an enzyme to interact with a whole range of substrates [5]. Such promiscuity may be manifested when enzymes react with chemically unrelated structures (substrate promiscuity) or carry out different types of chemical reactions (catalytic promiscuity). Also referred to as 'multispecific' or 'broad specificity enzymes', these enzymes include cytochrome P450s, glutathione transferases, glucuronosyltransferases, terpene cyclases, and methane monooxygenase, among others. In this interpretation, the promiscuous reactions with additional substrates faced selective pressures during evolution and are, by definition, part of the 'native' function of the enzyme. To understand how promiscuous enzymes achieve their promiscuity, it is important to highlight the most appreciated mechanisms that confer specificity to a typical enzyme.

1.2 MECHANISMS OF SPECIFICITY

Discussions of enzyme specificity are historically and inevitably linked to the fundamental issue of how enzymes function in general. The earliest proposed mechanism to account for the specificity of enzymes was the 'lock-and-key' model by Fischer, more recently referred to as the enzyme-substrate complementarity theory. It explains specificity as a straightforward consequence of the precise organization of the active site by complementary alignment of hydrogen bond donors/acceptors, charge pairs or hydrophobic surfaces in the enzyme-substrate complex. The three-dimensional alignment of these noncovalent interactions is a source of discrimination between the right cognate substrate vs. noncognate substrates. A more precise view originated by

Haldane and Pauling highlighted the importance of complementarity to the transition-state, rather than to the free substrate, remarking that an ideal enzyme with a maximized k_{cat}/K_m is one that has the highest affinity for the transition state of the reaction [13], [14]. In both theories, specificity is assigned to a rigid preorganized active site, ideally suited to interact with a specific substrate. Structure-based sources of substrate specificity are exemplified by thousands of crystal structures of enzymes from many sources that represent many structural folds and functional types.

The Fischer model intuitively explained why only substrates of a certain size could be accommodated in the active site but did not convincingly address how enzymes discriminate against substrates that are highly similar or smaller than the cognate substrates such as in the example of hexokinase, an enzyme that transfers a phosphate from ATP at a rate 4×10^5 faster to glucose than to the smaller hydroxylic acceptor, water. To address the discrepancy, Koshland invoked the concept that enzymes are not rigid, and proposed the now classic 'induced fit' theory (IF) which states that the 'right' substrate induces a conformational change to an 'active state' of the enzyme, driving catalysis (Figure 1.6.1). The 'active state' increases the residence time of the substrate on the enzyme and increases the forward flux of the reaction product from the cognate substrate. A key element of this model is that noncognate substrates may bind to the enzyme but not induce the active conformation.

The opposite limiting case that arises when the conformational change occurs *before* substrate binding is conformational selection (CS) (Figure 1.6.1). The CS model states that a substrate preferentially binds to the state in the free enzyme ensemble that is most optimal for catalysis. Here, the 'active' conformation already exists in the free enzyme ensemble. Thus, IF expands the conformational landscape by creating new substates, whereas CS narrows the landscape by excluding substates that do not form an 'active' ES complex.

The role of IF in specificity has at times been contested by Fersht, and then Herschlag, who showed that IF does not provide specificity relative to the uninduced enzyme when the conformational change (ES→E*S) is fast relative to the rate-limiting catalytic step [9], [15]. Under this assumption, the difference between a good and a poor substrate depends only on their ability to stabilize the transition state of the catalytic step and is therefore unaffected by the sequence of events in the thermodynamic cycle or whether binding involves a conformational change prior to catalysis. [Post and Ray introduced the concept that substrate-dependent conformational changes persist in the transition state of the chemical step, so that the 'active' form of the enzyme-substrate complex is different for different substrates [16]. However, as pointed out by Warshel and others, it is not clear why this would provide a specificity advantage since the uninduced enzyme would presumably face similar substrate-dependent differences that persist in the transition state [17]]. In the less common scenario where the conformational change or a binding step is rate-limiting, it is accepted that IF enhances specificity relative to an uninduced enzyme. A more recent objection to the classic Fersht analysis was raised by Johnson *et al* who argued that even when a chemical step is rate-limiting, the substrate-induced conformational change in IF will dictate specificity only if the rate of reversion of the *activated* enzyme-substrate complex back to the *initial* enzyme-substrate complex (E*S to ES) is slower than the catalytic rate (E*S to EP). [18], [19]. Since specificity depends on the energy barrier between the free enzyme and the highest energy transition state, a hypothetical scenario where the catalytic step is rate-limiting (a local maximum) but not the highest energy transition state overall (a global maximum) would relate k_{cat}/K_m to an energy barrier other than the chemical step and therefore provide specificity relative to an uninduced enzyme. It is unclear how common this scenario is in real enzymes.

Despite the controversy, IF is recognized as an important yet simplistic model for enzyme specificity. In reality, enzymes (and proteins in general) exist as ensembles of thermally accessible substates or conformations along a free energy landscape that are differentially populated according to the principles of statistical thermodynamics [20]. Disruptor events such as mutations or substrate binding reconfigure the conformational landscape by shifting the population of existing substates (CS) and/or populating new substates (IF). Benkovic and coworkers proposed the conceptual framework of enzymes as 'catalytic networks' in a multidimensional catalytic mountain range with substrates and products on opposite sides of a plane bisecting the energy landscape where free and bound forms of the enzyme are connected by parallel paths up and down the mountain [21].

The ensemble view of enzymes along with the advancement of solution and single-molecule techniques that detect lowly populated states in native conditions, have highlighted the role of conformational selection rather than induced fit as the dominant mechanism of molecular recognition. Based on kinetic arguments, Di Cera even argued that IF is mathematically a special case of CS [22]. The distinction between IF and CS is further blurred as the energy landscape becomes more rugged for complicated enzymes. Most likely, both mechanisms are operative in real enzymes and used in combination to achieve specificity and control [16]. This was recently demonstrated in a breakthrough study by Stiller and co-workers who showed that Adenylate Kinase (AdK) uses a mixed conformational selection and induced fit mechanism to phosphorylate ATP and AMP [23]. AdK has been extensively studied due to the open (inactive) to closed (active) conformational changes it undergoes during catalysis. The re-opening of the lid to release the phosphorylated product is the rate-determining step of the reaction. In the absence of substrate, AdK samples the low-energy open state and a high-energy partially closed state that was for the

first time directly characterized by NMR and computation methods in the Stiller study. The substrate binds initially to the high-energy state of the ensemble (CS) causing the enzyme-substrate complex to fully close (IF) and start the catalytic cycle. The reversible phosphorylation of substrate continues in the closed complex until the lid reopens to regenerate the partially closed state and release the product.

A turning point in the IF vs. CS debate was reached when Hammes *et al* highlighted the importance of net flux (instead of rate constants) in determining the mechanism of substrate binding and demonstrated that by considering both rates *and concentrations* of species present, enzymes can shift mechanisms from CS at low substrate concentration to IF at high substrate concentration. An important implication of the flux theory is that one must know the *in vivo* amounts of enzymes and substrates to accurately predict the biologically relevant mechanism of binding. Regarding specificity, the observed rate *in vivo* for two competing substrates may be very different if the substrates are present at different concentrations. Thus, a reaction can dominate *in vivo*, not because the enzyme is more specific for the reaction, but because the cell maintains a ratio of competing substrates that favors one reaction over another through spatial and temporal regulation of enzymes and substrates.

Lastly, *in vivo* specificity is also conferred by proofreading/proof-editing mechanisms such as those encountered in DNA and protein synthesis [9] and allosteric modulation of regulatory enzymes in metabolic networks, among other mechanisms.

1.3 MECHANISMS OF PROMISCUITY

Enzyme promiscuity is not as well understood as specificity. All enzymes are promiscuous to varying extent and ‘weak’ promiscuous activity appears to be the rule rather than the exception

[2]. An index of promiscuity developed by Nath and Atkins has been used to quantify promiscuous behavior of several classes of enzymes based their catalytic efficiencies toward a defined set of substrates [11]. It remains unclear whether promiscuous and specific enzymes are fundamentally different with respect to their structure, dynamics, and substrate interactions, and efforts to explain mechanistic aspects of promiscuity are ongoing.

1.3.1 Conformational dynamics and conformational diversity

Protein 'dynamics' includes their motion on a wide range of timescales from femtoseconds-nanoseconds (bond vibrations, side chain rotations) to microseconds-seconds (lid openings, domain/subunit rearrangements, etc.). The slower motions are the most relevant for biological function, although it has been suggested that rapid ps-ns fluctuations collectively affect catalysis and allosteric regulation [24]. All enzymes require a balance of flexibility and stiffness to sample different conformations, bind substrates, undergo conformational changes, perform catalysis, and release products. Flexibility is most important for substrate recognition, product release, and conformational changes, whereas stiffness favors catalysis by controlling the precise electrostatic environment required to stabilize the transition state.

Intuitively, conformationally flexible enzymes may interact with more substrates than rigid enzymes. Flexible enzymes populate more substates in the free state (CS) and change conformation more easily to accommodate diverse substrates in the bound complex (IF or IF-s). Implications for substrate recognition underline the role of conformational dynamics in substrate promiscuity. For example, the motion of a flexible active site loop in an aminoglycoside antibiotic resistance enzyme was identified as the molecular basis for the observed promiscuity towards structurally diverse antibiotics [25]. Studies on xenobiotic metabolizing CYP and GST enzymes

have shown that flexibility and promiscuity are correlated: among related enzymes, flexible isoforms are more promiscuous [26]–[28]. Molecular dynamics simulations of a resurrected ancestral TEM 1-β lactamase with broader substrate specificity than its extant successor revealed larger conformational fluctuations at the active site, despite both lactamases having nearly identical crystal structures [4], [29]. More recently, crystallographic and mutagenesis studies of an unusually promiscuous non-heme iron and alpha-ketoglutarate (Fe/aKg)-dependent oxygenase suggested that the plasticity of the loop region is responsible for the observed promiscuity [30].

Catalytic promiscuity sans conformational changes may result from the repurposing of side chains or waters in the catalytic machinery to interact with different functional groups on substrates and give rise to distinct Michaelis-Menten complexes in the transition state. The repurposing of the active site explains the ability of *Pseudomonas aeruginosa arylsulfatase* (PAS) to be a sulfatase and a phosphatase for different substrates [31].

Enzyme dynamics may indirectly affect the conformational sampling of substrates leading to large changes in specificity. In a recent example, Gade *et al.* rationalized through extensive structural and computational work that differences in conformational sampling by cognate and noncognate substrates are responsible for the substrate selectivity of two methionine adenosyltransferase (MAT) enzymes with nearly identical active sites [32]. Unlike the promiscuous MAT, the specific isoform did not allow for adequate conformational sampling of noncognate substrates, resulting in substrates being stuck in nonproductive binding modes. Since the active sites of the two enzymes are almost the same, the restrictions imposed by the specific MAT on binding modes of noncognate substrates were suggested to occur due to differential long-range stabilizing interactions from the second and third shell of the active site loop.

More controversial is the role of conformational dynamics in catalysis. Numerous examples in the literature have hailed dynamics to be an intrinsic property of enzymes that evolved to optimize catalysis, mostly based on evidence that rates of the chemical step correlate with motion of active site loops/domains [24], [33], [34]. Warshel has criticized the emergent role of dynamics in enzyme catalysis, arguing that dynamical effects have no significant role in catalysis when the chemical step is the rate-limiting step of the reaction. Some of the confusion stems from the use of the term "dynamical effects". Theorists describe a 'dynamical effect' as a time-dependent energy transfer driven by non-Boltzmann factors; the random motion of all atoms above 0 K does not constitute 'dynamics' because this motion is ruled by Boltzmann statistics. A dynamical effect for an enzyme means that the enzyme has evolved to optimize a bond vibration to move the complex to the transition state or the transition state to product. Warshel argues that an enzyme sampling the free energy landscape has nothing to do with 'dynamics' *per se*; it is instead exploring the energy surface according to Boltzmann principles without 'remembering' where it came from [35]. The excess binding energy released during *non-rate limiting* conformational changes dissipates before the complex crosses over the transition state. In other words, the complex does not get 'pushed' over the chemical step barrier by the conformational changes. Conversely, in an inertia-driven model where dynamical effects apply, the enzyme has a 'memory' of previous conformations and uses binding energy from conformational changes to propel the complex to the transition state of the chemical step. According to Warshel, the latter model is wrong for most enzymes and dynamics cannot modulate the free energy surface of enzymes since motion is a result of the energy surface, not the other way around. As the role of dynamics in catalysis, and by extension in substrate specificity and promiscuity, is still being

debated, we join here other experimentalists who use the term ‘conformational dynamics’ more broadly to include true dynamical effects *and* sampling effects on the energy landscape.

In the context of the energy landscape, flexible enzymes populate more states separated by low energy barriers and therefore uniquely exploit conformational selection to bind diverse substrates. For substrate-specific enzymes, a frustrated landscape with varied conformations separated by significant energy barriers in the unbound state may be a necessary cost to achieve substrate-dependent induced fit(s). The first direct measurement of the energy landscape roughness for nuclear receptor importin-β revealed a bumpy energy surface (>5k_BT) with multiple conformations in the free state consistent with the ability of impβ to interact with diverse partners [36]. Direct comparisons of the conformational landscape of related enzymes that display a spectrum of substrate selectivity (specific to promiscuous) remain limited, owing to the immense challenge of experimentally characterizing free energy landscapes.

A flatter energy landscape (wells separated by low barriers) has been attributed to some detoxification enzymes, based on reversible temperature-induced transitions of promiscuous GSTA1-1 vs. specific GSTA4-4 [37]. Honaker *et al* showed that unlike the fully cooperative unfolding of GSTA4-4 at higher temperatures, the disordered C-terminus of GSTA1-1 undergoes a reversible transition that is not coupled to the unfolding of the enzyme core, suggesting a more heterogenous ensemble of the promiscuous GST in the unbound state.

Considerations of the conformational landscape are also relevant to evolution of new protein function. A common view is that enzymes evolve new functions by exploiting minor portions of the conformational landscape that contribute to promiscuity, further evolving the landscape in favor of the minor conformers to optimize new specialized functions [38]. Promiscuous ‘generalist’ enzymes are easier to evolve than their less promiscuous counterparts

and more ancient enzymes are generally more promiscuous than newly evolved members in the same superfamily [2], [4], [20], [39]. Minimizing conformational sampling provides an advantage to specialist enzymes by freezing out of the landscape unproductive conformers that do not contribute to catalysis and limited conformational sampling has been shown for enzymes operating near the diffusion limit [40]. Altering conformational dynamics, particularly of loop or disordered regions, is considered the first 'stop' in the evolutionary path towards modifying enzyme behavior and altered conformational sampling is sufficient in some cases to change enzyme function [41].

The evolvability of enzymes from promiscuous generalists implies that there is a trade-off between catalysis and promiscuity: specialized enzymes have superior catalytic power towards their cognate substrate compared to their ancestral generalists. More recently however, directed evolution work has shown that it is possible to evolve promiscuous functions *without* compromising catalytic efficiency [42] and improving catalysis need not come at the expense of narrowing substrate specificity when there is no selective pressure for the enzyme to be specific.

The results of these studies reenforce the concept that specificity and promiscuity are selectable traits that enzymes adopt by tuning their sequence, structure, and dynamics in response to selective pressures.

1.3.2 Physicochemical attributes of the enzyme

It is unclear if substrate-specific and promiscuous enzymes have fundamentally different physicochemical attributes. Do size, depth, and hydrophobicity of the active site play a role in promiscuity? Are enzymes that adopt a certain fold or host a particular reactive center more prone to promiscuous reactions? What is the role of catalytic water in promiscuous outcomes? And finally, are activation of co-factors and allosteric modulators different for promiscuous enzymes

than specific ones? For the latter question, Jacoby proposed that detoxification enzymes (FMOs, GSTs, SULTs) may achieve promiscuity by stabilizing the reactive form of their cofactors in the absence of substrates [43]. The perpetually activated cofactors are presented indiscriminately to substrates, expanding the substrate interaction repertoire of detoxification enzymes. For instance, the pK_a of the thiol group of the glutathione cofactor in the active site of the promiscuous GSTA1-1 is low (pK_a~6.8) compared to the corresponding pK_a of glutathione in the specific GSTA4-4 (pK_a >9). Hence, the deprotonated glutathione (GS^-) in the active site of GSTA1-1 is 'ready' to react, unlike in GSTA4-4, where the thiol of glutathione remains protonated prior to any reaction with substrates. Drawing from Jacoby's proposal that readily activated cofactors are beneficial for promiscuity, the nature of the catalytic center itself may also contribute to promiscuity [44]. Catalysis in CYP enzymes hinges on formation of a highly reactive iron-oxo species that is one of the most powerful oxidants in nature. Once the catalytic cycle is set in motion, the iron-oxo catalyst is likely to react with any nearby oxidizable group. However, Jacoby's suggestion and similarly inspired proposals do not explain the routine use of highly reactive co-factors and catalytic machinery by substrate-specific enzymes and the promiscuity of enzymes lacking cofactors.

A straightforward contribution to promiscuity may be the size of the active site since enzymes with larger active sites can, in principle, accommodate more substrates. For instance, the highly promiscuous CYP3A4 has the second largest active site among drug-metabolizing enzymes that expands from 950 $Å^3$ in the free state to 2000 $Å^3$ with large substrates. In a large active site, substrates may sample greater conformational space and bind to different subsites, differentially engaging catalytic residues and water. As observed for CYP3A4, a large active site also accommodates multiple substrates at the same time which may result in promiscuous activity.

Extensive binding interfaces and multiple binding domains have also been credited with multispecific recognition in protein-protein and protein-DNA interactions [45]. In addition to size, hydrophobicity of the active site is likely favorable for promiscuity as fewer precisely orchestrated H-bonds and electrostatic interactions are needed. The interesting observation that cognate substrate binding for some enzymes is primarily enthalpic, whereas promiscuous binding is dominated by entropic contributions (hydrophobic interactions) alludes to the role of nonspecific hydrophobic interactions in promiscuity. Lastly, an active site dominated by hydrophobic forces may be more robust to mutations and more easily evolvable as demonstrated by directed evolution on bacterial P450s, recalling the promiscuity-evolvability connection described earlier.

Beyond the active site, promiscuous electrostatic interactions may be realized through charged binding interfaces on the surface of enzymes. For example, the interaction of Cytochrome P450 reductase (CPR) with a variety of P450 enzymes is mediated through electrostatic interactions between negatively charged residues on the FMN domain of CPR with positive residues on the proximal side of P450 enzymes (though recent reports suggest that the role of non-electrostatic interactions between CPR and P450s is underestimated).

The role of active site architecture in promiscuity is uncertain. However, examples in the literature point to flexible domain insertions [46], [47], an open active site cavity exposed to solvent [7] and enzyme folds exploiting flexible linkers [48] as advantageous for expanding interactions with substrates. The extent to which the conclusions of these studies can be generalized for most enzymes is unclear.

Recently, Thakur and Pandit reviewed the physicochemical attributes of active site and binding residues of 27 promiscuous and 19 substrate-specific enzymes [49]. Surprisingly, they found that promiscuous and specific enzymes are similar with respect to flexibility, size, non-polar

surface area (hydrophobicity), depth (distance of active site from the protein surface) and secondary structure character (helix/sheet vs. loop) of the active site. Promiscuous enzymes had more loops and hydrophobic residues in the active site, but the difference was not statistically significant. Despite the problematic comparison of a small set of unrelated enzymes based on crystal structure properties, the Thakur and Pandit analysis would suggest that there are not large differences in physicochemical attributes of the active sites of promiscuous and specific enzymes. This result is consistent with the widespread promiscuity of enzymes and promiscuity being on a continuum as opposed to a discrete characteristic that enzymes either have or lack.

1.3.3 Physicochemical attributes of substrates

In addition to the enzyme characteristics discussed in 1.3.1 and 1.3.2, attributes of substrates such as flexibility, hydrophobicity, size, and complexity, have been proposed to contribute to promiscuity, though such reports remain controversial [6], [50]–[53]. An early study on the conformation of drug-like molecules in bound complexes showed that flexibility of substrates correlates with the level of strain they tolerate when bound [54]. In principle, more flexible substrates may bind to more targets. For instance, the large number of rotational bonds in the HIV protease inhibitor drug ritonavir has been credited in part with the observed promiscuity of ritonavir in hydrolase and protease multifamilies [55]. A weak correlation between substrate flexibility and promiscuity was uncovered in a systematic analysis of PDB structures with 164 promiscuous drugs [56]. The same study found no correlation between substrate size, hydrophobicity, and promiscuity. Other groups have reported that promiscuous activity correlates with substrate hydrophobicity [57]–[59]

1.4 CYTOCHROME P450-S

Cytochrome P450 enzymes are a superfamily of heme-containing enzymes that activate and transfer molecular oxygen to a wide range of compounds to protect organisms from poisoning or supply essential molecules like sex hormones and brain neurotransmitters [60]. Typically, one oxygen atom is incorporated into the substrate, and the other is converted to water. The reaction proceeds via a *catalytic cycle* (Figure 1.6.2) that is supplied with two reducing and two proton equivalents to generate the primary catalytic species, a highly reactive heme-thiolate-oxo intermediate (Compound I) that catalyzes a plethora of reactions, including alkane and arene hydroxylation, heteroatom-dealkylation, alkene epoxidation, desaturation, isomerization, heteroatom oxygenation, alcohol and aldehyde oxidation, and C-C bond cleavage reactions, among others. P450 enzymes are ubiquitous in nature, particularly in eukaryotes, in which the majority of the >41,000 named P450 sequences are found [61]. In humans, 57 P450 isoforms are organized in 18 families conserved across mammals. Their functions are broadly categorized here into metabolism of xenobiotics and biosynthesis or transformation of sterols, fatty acids, eicosanoids, and vitamins (Table 1.7.1) [62]. In general, xenobiotic metabolizing P450s display broad substrate selectivity and high interindividual variability (5-10-fold, on average), whereas biosynthetic P450s have defined physiological roles and low interindividual variability. Xenobiotic metabolizing P450s also oxidize endogenous compounds, as evidenced by the 6β-hydroxylation of testosterone – one of the fastest reactions catalyzed by 3A4. However, the physiological relevance of these reactions, if any, is unknown. Some biosynthetic isoforms such as 11A1, 24A1 and 46A1 have been found to efficiently catalyze drugs, in addition to their native substrates, suggesting broader substrate selectivity than originally considered for these isoforms. Nevertheless, the substrate promiscuity of xenobiotic metabolizing P450s is unmatched – P450 3A4 alone accounts for ~45%

of P450-mediated metabolism or one third of (small molecule) drug metabolism overall, and just three such isoforms (3A4, 2C9, 2D6) oxidize ~75% of P450 xenobiotic substrates.

1.4.1 CYP structure and dynamics

Despite sharing modest sequence similarity, all CYPs have adopted a unique and conserved protein fold that presumably evolved to best support heme-thiolate-mediated catalysis, coupling with redox partners, and stereochemical requirements of substrate recognition (Figure 1.6.3) [60]. The fold accomplishes the daunting task of generating a catalyst powerful enough to oxidize unreactive saturated carbon centers of substrates, while maintaining the fragile protein environment intact. In general, the closer to the heme, the more *conserved* and *rigid* the structure, particularly at the I and L-helices that make direct contact with heme functional groups (Figure 1.6.3) [62]. The conserved β-bulge right before the L-helix contains the cysteine residue that axially coordinates to the heme iron and is essential for catalysis. The other most conserved feature is a portion of the I-helix near the heme iron that activates molecular oxygen. The precise position of the elements of the secondary structure varies considerably among different isoforms to provide substrate specificity and regiospecific orientation with respect to the reactive heme-oxo-intermediate [63].

Unsurprisingly, the regions associated with substrate recognition, primarily congregated at the substrate binding pocket on the distal face of the heme, are the most variable [64]. The highly variable F-G region is longer in eukaryotic P450s and often includes shorter helices F' and G' that connect to the longer F and G helices via flexible loops and together form the colloquial 'lid' or 'roof' of the active site that gates access to the heme and can rearrange to accommodate diverse substrates. Based on a comparison of P450 crystal structures and dynamic information from NMR and mass spectrometry, Pochapsky and coworkers concluded that features of the I-helix, β3 and

β5 at the active site determine which types of substrates will bind, whereas features of the B-C and F-G loop dictate the final orientation of substrates in the active site by changing conformation to accommodate the bound substrate [65].

A collection of crystal structures with diverse substrates has revealed marked conformational plasticity for xenobiotic metabolizing P450s. For example, the crystal structure of 3A4 bound to substrate midazolam featured a dramatic rearrangement of the F-G region that consisted of a one-turn extension of the F-helix, 20° rotation of the G'-helix, complete and partial unravelling of the F' helix and G-helix, and a 3-12 Å movement of the F-F' loop that along with a 5 Å movement of B-C loop and a 3 Å movement of the C-terminal loop, cause the partial collapse of the active site cavity around the substrate [66]. Pioneering work that examined the unusual plasticity of P450 2B4 structures with diverse inhibitors bifonazole and 4-(4-chlorophenyl)imidazole (CPI) assigned five "plastic" regions (PR-s): 1) the AA'-loop and most of A-helix, 2) the area from the B'-helix to the C-D loop, 3) the C-terminal end of the E-helix, 4) the area from the C-terminal end of the F-helix, to the N-terminal half of the I-helix, and 5) the C-terminal β5 loop (Figure 1.6.4A-B) [67]. These regions match well with the 10 flexible regions (FR-s) identified by MD [68]. Since then, the expanded collection of P450 crystal structures has confirmed the plasticity of PR-s for other xenobiotic metabolizing P450s [69]. It should be emphasized that structural features of P450s *across the substrate selectivity spectrum* are known to undergo large conformational rearrangements upon binding of substrates [70]–[74]. In a classic example, bacterial fatty acid hydroxylase P450-BM3 undergoes a large open to closed transition upon binding of native substrate palmitate [74]. Dubeik and Shayk performed long MD simulations (360 ns) and QM/MM calculations to show that the dramatic closing of the main access channel upon substrate binding is achieved by channel components A-helix, β1 sheet and the F

helix closing the distance from 15 Å to 2.5 Å (the β1 sheet moves as much as 11 Å towards the F-helix) [75]. A recent crystal structure of CYP51, a sterol 14-demethylase from yeast, showed a 3.5-6 Å movement of the F/G arm, H/I arm and C-helix upon binding of its native substrate lanosterol [73]. Furthermore, the static structures of the detergent-solubilized human P450 constructs do not account for the role of the membrane in the observed conformational plasticity and interactions with substrates. A rare crystal structure of a full-length CYP51 with an intact transmembrane domain showed smaller conformational changes due to lanosterol binding compared to previous lanosterol-bound structures of the soluble ectopic counterpart [76]. It was proposed that the transmembrane helix posed constraints on the orientation of the catalytic domain with respect to the bilayer and thus on the conformational landscape of the enzyme. Recently, long MD simulations on 3A4 bound to midazolam in a membrane model showed a smaller sinking of the F-F' loop towards the substrate compared to the dramatic shift observed in the crystal structure of the 3A4-midazolam bound complex [77], [78]. Wade and coworkers demonstrated through a series of simulations that the lipid bilayer affects dynamics and tunnel opening of membrane-bound P450s, which likely affects the extent of conformational changes and substrate-dependent distribution of conformers in a native environment [79]. (A detailed review of the role of the membrane in structure and function of xenobiotic metabolizing P450s is provided in [80].)

Since large and substrate-dependent structural rearrangements are *not* unique to the malleable xenobiotic metabolizing P450s, it becomes less obvious how to distinguish between the specific and promiscuous isoforms based on static structures with select ligands, without dynamic information. A range of computational [81]–[89][1], spectroscopic [90]–[94], solution NMR [72], [95]–[100], and mass spectrometry methods [78], [101]–[105] have been used to investigate the

[1] References are of notable examples or comprehensive reviews on the topic.

structural dynamics of primarily soluble bacterial P450 enzymes or detergent-solubilized constructs of human P450s. Some important findings are summarized below, with priority given to experimental investigations of conformational plasticity and effects of substrate binding in membrane bound human P450s.

The P450 ensemble is heterogeneous in the absence and presence of substrates, effectors, and redox partners. Ligands differentially stabilize discrete states of the ensemble, though abundant evidence of ligand-dependent induced fit on P450 structures exists. Conformational changes are most pronounced at the F-G and B-C regions of the protein, but otherwise globally distributed. In addition to ligands, dynamics are modulated by protein partners, solvent, and the membrane environment. Promiscuous P450s are reportedly more malleable, though the extent to which this can be generalized across isoforms is not known.[2]

The bulk of P450 structural dynamics information comes from the highly specific P450cam, a soluble bacterial isoform from *pseudomonas putida* that catalyzes the 5-exo-hydroxylation of camphor, and for which the conformational landscape in various conditions has been extensively investigated by x-ray crystallography [106]–[110] and multidimensional solution NMR methods [65], [111]–[118]. P450cam adopts at least three conformations in solution (closed, intermediate, open) that differ substantially in the position of the F-G region and B'-helix [106], [107], [119], [120] and are differentially distributed in the presence of substrates and redox partner, Pdx. Of note, the alternate conformers went undetected in early crystal structures of the substrate-free and substrate-bound enzyme [109], illustrating how investigation bias may influence our understanding of conformational plasticity in P450s, since more information is available for some isoforms than others. Multiple conformations in solution have also been characterized for

[2] Summary surmised by author based on an agglomeration of evidence with various P450 isoforms in past and recent literature.

thermophilic P450 119. Basudhar *et al* used two-dimensional $^{1}H,^{15}N$ HSQC mapping of ^{15}N-labeled Phe residues to show that substrates and imidazole-based inhibitors differentially stabilized discrete states of the P450 119 ensemble [72].

In a first application to human P450s, solution NMR was used to probe the conformational plasticity of steroidogenic P450 17A1, responsible for the C17-hydroxylation of pregnenolone and the subsequent 17,20-lyase reaction that produces dehydroepiandrosterone, an important intermediate in sex hormone synthesis. Few structural features could be assigned, nevertheless, unambiguous evidence was provided for multiple states and exchanging backbone conformations populating the 17A1 ensemble in both the free and abiraterone-bound states. Moreover, the distribution of states was shifted by temperature, two substrates, and the soluble component of redox partner cytochrome *b*5, which is known to stimulate the lyase reaction of 17A1 [95], [121]. Importantly, substrate binding in the studies above cause conformational changes that extend beyond the binding site. The effects of the redox partner binding on the P450 structure are also globally distributed beyond the binding interface, as shown by Pdx binding to P450cam [122], cytochrome *b*5 binding to 17A1 complex [95], and cytochrome P450 reductase (CPR) binding to 3A4 [105]. Due to primarily protein size limitations and high concentration requirements, NMR studies of structural dynamics remain limited and at the time of preparing this thesis, no such studies with membrane embedded xenobiotic metabolizing P450s have been published.

MD simulations with three xenobiotic metabolizing P450s (3A4, 2C9, 2A6) showed a flexibility pattern that correlated with their respective substrate specificities: the most promiscuous P450 was the most flexible and vice versa [26]. Hendrychova *et al.* reached a similar conclusion by using UV/VIS spectroscopy and resonance raman (RR) spectroscopy in combination with all-atomic MD simulations under normal and high pressure to show that the active site compressibility

(hence, malleability) correlated with the substrate specificity of five xenobiotic metabolizing P450s (3A4, 2C9, 2D6, 1A2, 2A6). The most promiscuous P450 isoform 3A4 had the most compressible active site, followed by 2C9 and 2D6 with intermediate compressibility, and 1A2 and 2A6 with the lowest compressibility [68]. (An earlier investigation comparing active site properties of 3A4 to those of bacterial P450BM3 by high pressure absorbance spectroscopy reported a *less* compressible active site for 3A4 than for P450BM3 [123], suggesting a more complex relationship between active site compressibility and substrate specificity than the one outlined in the Hendrychova *et al*. report, since 3A4 is reportedly more promiscuous than BM3). In a follow-up study, the same group used molecular dynamics simulations to report >50% variation in active site volume over 100 ns for six xenobiotic metabolizing P450s (3A4, 2C9, 2D6, 2A6, 2E1, and rabbit 2B4), in agreement with the plasticity of xenobiotic metabolizing P450s conferred by the crystal structures [124]. The variation in active site volume was mostly due to movement of main chains, as opposed to independent movement of side chains.

Finally, the role of structural dynamics in interactions with substrates has been explored by Hydrogen-Deuterium Exchange Mass Spectrometry (HDX-MS) for a limited number of P450s. HDX-MS probes the accessibility of amide hydrogens by deuterons in the solvent and is considered in detail in Chapters 2 and 3 of this thesis. Briefly, ordered hydrogen-bonded regions exchange deuterium more slowly than regions that are more disordered or solvent accessible. HDX-MS has been used to show that the reduced ferrous form of P450cam is more rigid than the oxidized ferric counterpart [125] and to map the binding interface between the P450 and reductase domains in full-length P450-BM3 [101]. The first example of HDX-MS used to probe the structural dynamics of a human P450 was provided in 2010 by Halpert and associates who investigated the plasticity of CYP2B4 in solution with two imidazole-based inhibitors. Only two

peptides (95-115, 225-243) spanning the B-C and F-G regions showed significantly different (lower) deuterium uptake in the presence of one inhibitor (4-CPI) but not the other [126]. Suppression of deuterium uptake in the substrate-bound complex was also observed for steroid metabolism P450 46A1 with native substrate cholesterol [104], and membrane-embedded steroid metabolism P450 aromatase with native substrate androstenedione in this work [103].

Pioneering work with membrane-embedded 3A4 carried out in the Atkins lab showed subtle substrate-dependent effects on 3A4 dynamics with inhibitor ketoconazole and substrate/allosteric effector, midazolam, discussed in detail in Chapter 2 [78], [102]. Recently, Ducharme *et al.* reported on the effect of CPR and three substrates (testosterone, progesterone, and 7-benzyloxy-4-trifluoromethyl-coumarin) on 3A4 in solution [105]. The study was carried out in parallel to the work described here and a comparison of the HDX results is included in Chapter 2.

1.4.2 CYP3A4

As mentioned in the section above, 3A4 is the most promiscuous human P450 isoform metabolizing nearly half of drugs transformed by xenobiotic metabolizing P450s [62]. Its extreme substrate promiscuity has been attributed to a large, open active site, and a flexible structure. At least 50 crystal structures of wild type 3A4 exist, over two thirds of which are of 3A4 bound to analogs of HIV protease inhibitor and strong 3A4 inhibitor, ritonavir. All the crystal structures lack the transmembrane helix at the N-terminus. Full-length 3A4 is a ~57 kDa protein anchored to the ER via a single pass helix that positions the globular domain towards the cytosol at a ~70° heme tilt angle with respect to the normal plane of the ER membrane [127].

Superposition of crystal structures with dissimilar substrates indicates modest global differences in main chain atoms, but large differences in the position of secondary structure

elements at or near substrate recognition sites (Figure 1.6.5). The F-G region is the most variable, followed by the H-I loop and N-terminus of the I-helix, the E-F loop, and the C-terminus loop. Unlike for CYP2 enzymes, the A'-A and B-C blocks in 3A4 are less flexible and undergo smaller conformational changes with substrates. The active site volume varies widely between 530 $Å^3$ [128] and 2000 $Å^3$ [129], second on average only to 2C8 among xenobiotic metabolizing P450s. The main difference in the topology of the active site between the two isoforms is the larger volume above the heme in 3A4, leaving the heme more exposed to substrates than in other xenobiotic metabolizing P450s. The active site consists primarily of hydrophobic residues and lacks deep grooves or pockets, features that likely contribute to the promiscuity of 3A4 with hydrophobic substrates. Unlike for most P450s, the F-helix in 3A4 is short and does not cross over the active site, connecting instead to the F'G' motif via a flexible loop (residues 211-218) known to dramatically rearrange upon binding of substrates [66], [69], [130], [131].

The active site can accommodate multiple substrates, as initially proposed by kinetic methods [132] and subsequently validated by doubly bound crystal structures [129]. No crystal structure with two non-identical substrates has been published. The capacity to bind multiple substrates provides one likely explanation for the unusual kinetic behavior of 3A4 with a wide range of substrates that display cooperative binding and metabolism observed both *in vitro* and *in vivo* [133]. By contrast, multiple ligand binding in 2C8 does not necessarily result in cooperative behavior [134]. Site-directed mutagenesis work has highlighted a possible role for residues F304 (I-helix), L211, F213 (F-F' loop) in cooperativity based on loss of cooperative behavior with select substrates in the respective mutants. However, the outcomes of such mutations on allosteric behavior are substrate-dependent, complicating the task of assigning a structural basis to the observed cooperativity. An interesting crystal structure with a progesterone molecule bound 17 Å

away from the heme iron (between the FF' and GG' loops) sparked a debate on whether a putative 3A4 allosteric site exits. Collective evidence thus far suggests that allosteric effectors are more likely to bind at subsites within the active site rather than at a completely distinct and designated allosteric site [62].

The enigmatic and unpredictable allosteric behavior in 3A4 reflects a shortcoming in our understanding of 3A4 behavior with substrates, in general. An often-used rationale for the observed unpredictability is the malleability of the protein structure. As mentioned earlier, MDS have shown that the 3A4 active site is more flexible than that of other xenobiotic metabolizing P450s. Recently, Becker *et al* demonstrated by computational methods that the structural flexibility of the important F-G region also correlated with substrate specificity: the more flexible the F-G region, the more promiscuous the P450 isoform [135]. Lastly, kinetic and spectroscopic methods have been used to indirectly detect multiple 3A4 exchanging conformers [62], though it is unclear whether the native conformational ensemble of 3A4 is more heterogeneous than that of other P450 isoforms.

1.4.3 CYP19A1

CYP19A1 or "aromatase" is a steroidogenic P450 responsible for converting androgens (androstenedione, testosterone, 16α-hydroxytestosterone) to estrogens (estrone, 17β-estradiol, and 17β,16α-estriol, respectively) (Figure 1.6.6) [62], [136]. The reaction involves two consecutive methyl hydroxylations at C19, followed by aromatization of the steroid A-ring, a step unique to 19A1. Deficiencies in this process that result from (rare) 19A1 gene mutations lead to abnormal physiology such as ambiguous genitalia and impaired puberty in women and indeterminate sexual characteristics and osteoporosis from estrogen deficiency in men [137]. Third generation

aromatase inhibitors exemestane, anastrozole, and letrozole constitute an important therapy for estrogen-dependent breast cancer in post-menopausal women and gynecomastia in men. Exemestane is a steroidal inhibitor that mimics the native androgen and inactivates 19A1 by forming a covalent adduct. Anastrozole and letrozole are nonsteroidal inhibitors that noncovalently block the active site by strong coordination of the azole nitrogen to the heme iron. The successful druggability of 19A1 stems from its high specificity for androgen substrates.

The structural basis for androgen specificity was revealed in 2009 when the first structure of androstenedione-bound 19A1 was solved [136]. It was the first P450 structure crystallized from a native source (term human placenta) and the first mammalian P450 to be crystallized full-length with an intact membrane anchoring domain. The active site of 19A1 consists of an androgen-specific, tight-fitting cleft (~400 $Å^3$) with polar and hydrophobic residues that perfectly complement the steroid backbone of the androstenedione substrate (Figure xx). Membrane integration has been proposed as essential for lipophilic steroid substrates to gain access to the active site [136], [138]. Subsequent structures with other steroidal substrates (testosterone) [139] and inhibitors (exemestane and related derivatives) [140] were nearly identical to the androstenedione-bound structure reflecting similar binding modes. No structures of 19A1 in the free state or bound to nonsteroidal ligands have been published.

Early computational work indicated that 19A1 is rigid and undergoes minimal conformational changes in the presence of substrates [141]. However, the role of conformational flexibility has been indirectly implicated in the allosteric modulation of 19A1 activity by tamoxifen metabolites [142]. The predominant tamoxifen metabolite, endoxifen, inhibits 19A1 by binding at a peripheral site that has been hypothesized to cause the remote closing of the substrate channel. More recently, long simulations (20 μs, cumulative) showed a large structural rearrangement of

19A1 upon binding of androstenedione and letrozole [143], a result that is consistent with work presented in chapter 3 of this thesis.

1.5 GLUTATHIONE TRANSFERASES

Glutathione transferases (GSTs) are a superfamily of enzymes that conjugate reduced glutathione (GSH) to soft electrophiles. The main functions of GSTs include metabolism of xenobiotics, detoxification of products of oxidative stress, biosynthesis of steroid hormones and eicosanoids, and regulation of signaling pathways. Depending on their cellular localization, eukaryotic GSTs are categorized into three families: cytosolic GSTs, mitochondrial GSTs, and microsomal GSTs, also known as MAPEG-s (membrane-associated proteins involved in eicosanoid and glutathione metabolism). Cytosolic and mitochondrial GSTs are soluble enzymes with a similar fold, whereas MAPEGs bare no structural similarity to the other two families.

Cytosolic GSTs constitute the largest of the families and are separated into classes based on sequence and structure similarity. In humans, members of seven classes of cytosolic GSTs are present: alpha (5 members), mu (5 members), pi (1 member), sigma (1 member), theta (2 members), zeta (1 member), and omega (2 members). Same-class members share ~40% sequence homology. Cytosolic GSTs are catalytically active as dimers of two subunits related by C2 symmetry. Isoforms are named according to the identity of the subunits, and the species they are found. For instance, hGSTA1-1 is the human GSTA1 homodimer. Each subunit consists of one-third N-terminal domain and two-thirds C-terminal domain. The well-conserved N-terminal domain contains the GSH binding site (G-site), also found in other GSH-binding proteins such as thioredoxin, glutaredoxin, and glutathione peroxidase. Substrates bind in the hydrophobic C-terminal domain (H-site) which varies substantially across isoforms. An active site tyrosine (alpha,

mu, pi, sigma), serine (theta, zeta) or cysteine (omega) in the N-terminal domain forms a critical hydrogen bond with GSH to stabilize the thiolate nucleophile GS^- needed for GSH transferase activity. The precise mechanism of GSH activation is isoform and substrate dependent.

In addition to the archetypal detoxification reactions of electrophilic substrates, cytosolic GSTs contribute to the intracellular transport of non-substrate ligands such as heme, bilirubin, PAHs, and steroids (ligandin function), and to the regulation of signaling pathways through enzymatic or physical modulation of signaling components. Class mu and pi GSTs inhibit MAPK pathway members ASK1 (apoptosis signal-regulating kinase 1) and JNK (c-Jun N-terminal kinase), respectively. GSTP1 further modulates JNK signaling by binding upstream activator TRAF2 (tumor necrosis activator factor 2), and more recently, has been identified as a key regulator of CDK5 (cyclin-dependent kinase) signaling, providing protection against neurodegeneration in AD patients. GSTs are overexpressed in various tumors, affect resistance to chemotherapy agents, and GST mutations have been associated with Alzheimer's, Parkinson's, and increased risk for cardiovascular disease, among other diseases.

Cytosolic GSTs are generally highly substrate and catalytically promiscuous. However, even within the same class, there are marked differences in substrate selectivity as exemplified by the four isoforms of the alpha class GSTs. Promiscuous GSTA1-1 and (to a lesser extent) GSTA2-2 conjugate GSH to diverse electrophiles, catalyze the GSH-dependent isomerization of steroids, and show peroxidase activity towards various hydroperoxides. On the other hand, GSTA3-3 shows specific activity towards the Δ^5-Δ^4 isomerization of steroids, and GSTA4-4 is highly efficient at detoxification of alkenal products of lipid peroxidation such as 4-hydroxynonenal (HNE), nonenal (NE), and 4-hydroxydecenal. Some of the characteristics that contribute to the different substrate selectivity are illustrated below for two isoforms: GSTA1-1 and GSTA4-4.

1.5.1 GSTA1-1 vs. GSTA4-4

GSTA1-1 and GSTA4-4 share 54% sequence identity and adopt very similar structures. Backbone alignment of the apo structures results in only a 0.91 Å root mean square deviation (RMSD). Sequence variations are mostly found on the alpha-class specific α9 helix at the C-terminus, and the α4-α5 helix-turn-helix 'tower' region above the H site at the dimer interface. The extreme promiscuity of GSTA1-1 has been attributed in part to the well-characterized conformational flexibility of the α9 helix. The helix is disordered in the apo state and becomes ordered upon binding of substrates, acting as a lid that closes the active site at a substrate-dependent location. Even when closed, the helix remains dynamic as indicated by the high crystallographic B-factors of the available GSTA1-1 complexes, and hydrogen-deuterium exchange data showing that GSTA1-1 is generally more flexible than GSTA4-4. The α9 helix in GSTA4-4 is ordered in both apo and bound forms. The helix is located along the side of the narrow hydrophobic cavity that accommodates long-chain lipid alkenal substrates. An edge-to-face aromatic interaction, absent in GSTA1-1, between a tyrosine in the α9 helix and a phenylalanine in the tower motif, is thought to stabilize the α9-helix in place. Structural justification for the specificity towards lipid alkenals was based on Tyr212 positioned to donate a H-bond to the enolate intermediate that results from the Michael addition of GS^- thiolate to the α,β-unsaturated lipid alkenals.

Less explored are the differences in reaction mechanisms between the two isoforms. Catalytic Tyr9 residues in alpha class GSTs are characterized by lower than usual pK_a values (< 10.3) to stabilize the reactive GS^- nucleophile. pK_a values of Tyr9 in GSTA1-1 and GSTA4-4 are 8.1 and 6.7, respectively, suggesting opposite protonation states in physiological conditions. A GSTA1-1 mutant redesigned to adopt the active site features of GSTA4-4 showed increased specificity towards alkenals and GSTA4-4-like acidic Tyr9 with a pK_a of 7.1, suggesting a

correlation between Tyr9 acidity and alkenal activity. The pK_a values of the bound GSH in GSTA1-1 and GSTA4-4 are also different. A network of H-bonds involving Tyr9 and other residues lowers the pK_a of the cysteine thiol hydrogen of GSH upon binding at the G-site. In GSTA1-1, bound GSH has a pK_a of 6.7, and is therefore deprotonated as the activated GS^- nucleophile in physiological conditions. As noted in section 1.3, perpetually activated cofactors in the absence of substrates were proposed by Jacoby as beneficial for promiscuous detoxification. Conversely, limited data on GSH bound to GSTA4-4 indicate that GSH largely retains its thiol proton in physiological conditions and needs to be activated for a nucleophilic attack on substrates to be initiated. Hubatsch and Mannervik proposed a theoretical mechanism for the Michael addition of GSH to lipid alkenals by GSTA4-4 that consisted of the deprotonated tyrosinate activating a bound water molecule in the active site that pulls a proton from GSH at the same time as the latter attacks the electrophilic substrate. The mechanism was suggested based on observations of bound water molecules in the crystal structures of GSTA4-4, and a longer distance between Tyr9 and GSH in GSTA4-4 compared to GSTA1-1 structures. An important consequence of such mechanism is that GSH activation is part of a substrate-dependent proton relay system, i.e., GSH is not pre-activated in the absence of substrates. Since its proposal over 20 years ago, the mechanism remains to be experimentally validated. However, the differences in pK_a values of GSH and key residues in the respective active sites suggest that activation of GSH and catalysis are distinctly orchestrated by the two enzymes, providing a ‘reaction mechanism’ avenue as the basis for the observed difference in substrate selectivity.

1.5.2 Reversibility as a component of specificity or promiscuity

Discussion of substrate 'specificity' has focused on the ability of an enzyme to select substrates, without acknowledging the ability of an enzyme to preferentially catalyze the forward vs. the reverse reaction. In as much as many enzymatic products are structurally similar to the substrates, the reversibility of an enzyme may be related to its 'specificity'. Afterall, the transition state of a reaction stabilized by a specific enzyme is identical in the forward and reverse directions. Although, all enzymes, in principle catalyze any specific reaction in both directions as postulated by the Haldane relationship [1], many have evolved to optimize flux in a single direction. This is often assumed for detoxification enzymes, perhaps based on the assumption that the substrate is more toxic than the product. However, many examples have been documented in which the product of a detoxification enzyme is more toxic than the product, also referred to as 'bioactivation'. Toxic drug metabolites are sufficiently common that the drug development efforts include screening for bioactivation. Based on the possibility of bioactivation, probabilistic models that assume an equal chance of toxicity from either substrate or product indicate that a reversible detoxification enzyme may have short-term advantages over one-way detoxification enzymes by distributing the toxic potential into two or more chemical forms. Thus, putative advantages for one-way catalysis by detoxification enzymes are not obviously real in all cases.

Regulatory enzymes, in contrast, allow flux in both directions. Since it is recognized that nonenzymatic conjugation of GSH to electrophiles is reversible, and GSTs are both canonical detoxification enzymes and known in some cases to regulate signaling pathways, the flux of substrates to products may have implications for the functional niches of related GST isoforms. The main substrate of the specific GSTA4-4, 4-hydroxynonenal (HNE) has emerged as a secondary messenger molecule that plays a dual role as protective against oxidative stress at low

concentrations and harmful at high concentrations. As the most efficient GST isoform that acts on HNE, it is conceivable that in addition to detoxification, GSTA4-4 contributes to regulation of HNE levels *in vivo*. Speculatively, the preferential formation of the GS^- thiolate at the active site of GSTA1-1 in the absence of substrates could be part of an evolutionary strategy to optimize 'one-way' catalysis and avoid regeneration of the toxin substrate. For such GSTs, the active site disfavors protonation of the leaving thiolate when a GS-conjugate is in the enzyme complex. If the GS^- thiolate is regenerated in the absence of a proton donor, the thermodynamic driving force will favor forward flux to the GS-conjugate. In contrast, a substrate-specific GST like GSTA4-4 that stabilizes a transition state for a complex-dependent proton relay system, may be catalytically efficient in both forward and reverse directions. It is known that some GSTs undergo reversible reactions, but little attention has been devoted to the topic, likely because the reverse reactions would be disfavored in the presence of the high millimolar quantities of GSH in the cell. Armstrong and Chen showed that rat class mu GSTs (rGSTM2-2 and to a lesser extent, rGSTM1-1) readily catalyzed the retro-Michael reaction of a GS-conjugate. Interestingly, like hGSTA4-4, rGSTM2-2 is highly efficient for α,β-unsaturated aldehydes.

The relationship between substrate specificity and reversibility has not been considered in the literature. A hypothesis considered in this thesis is that GSTA1-1 and GSTA4-4 are differentially 'reversible' because they stabilize a ground state reactive nucleophile or a transition state proton relay network, respectively. Chapter 4 explores these previously unconsidered aspects of detoxification catalysis and the relationship between substrate specificity and reaction reversibility.

1.6 FIGURES

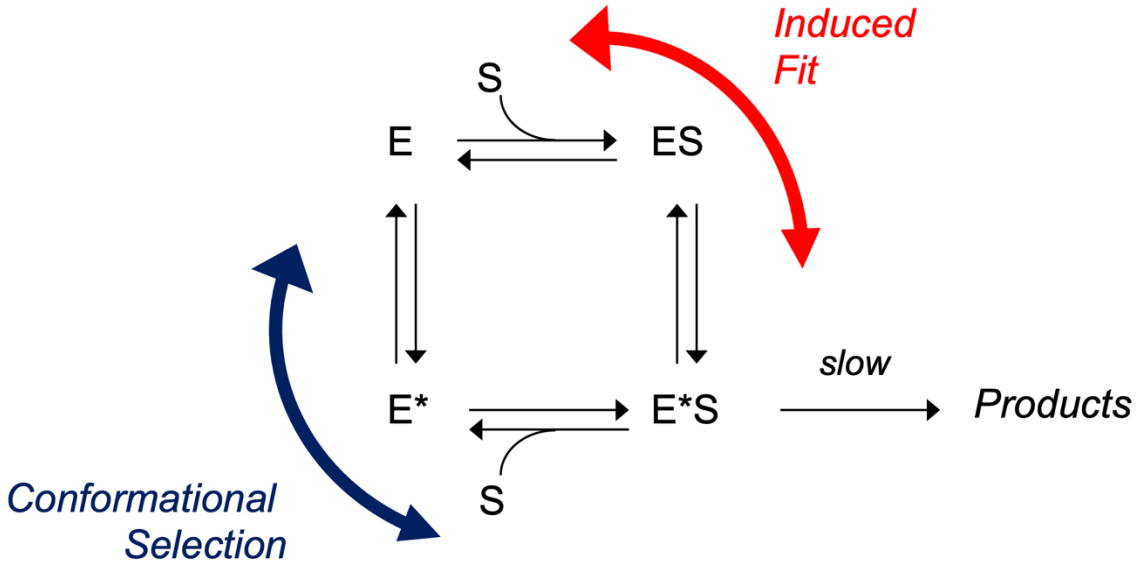

Figure 1.6.1. Induced fit vs. conformational selection. Schematic representation of two limiting-case scenarios of a substrate (S) binding to an enzyme (E). E* represents a more active conformer of E. **Error! Reference source not found.**.

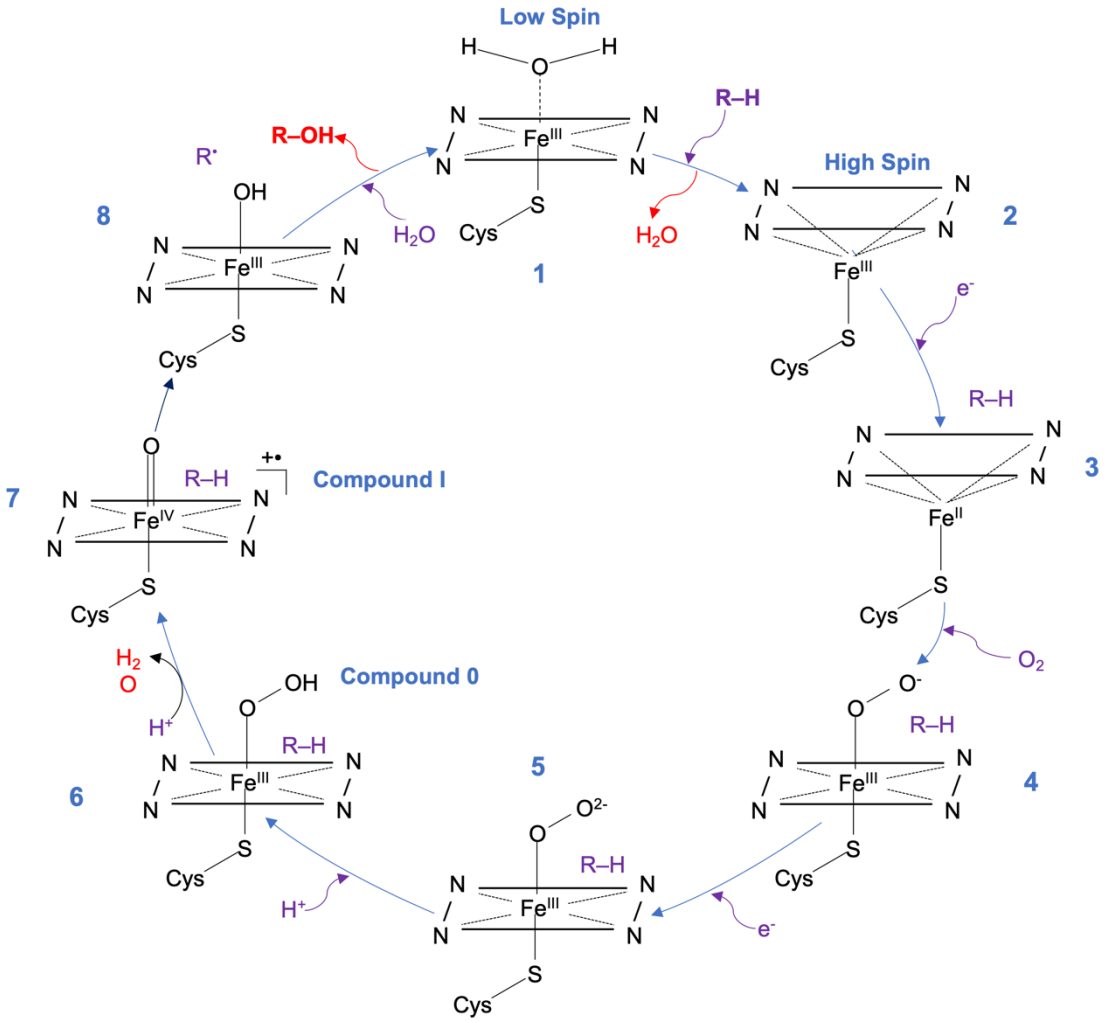

Figure 1.6.2. **Catalytic cycle of cytochrome P450 enzymes during hydroxylation of a type I substrate, R-H.** Species entering and exiting the cycle are shown in purple and red, respectively. The heme is shown in truncated form.

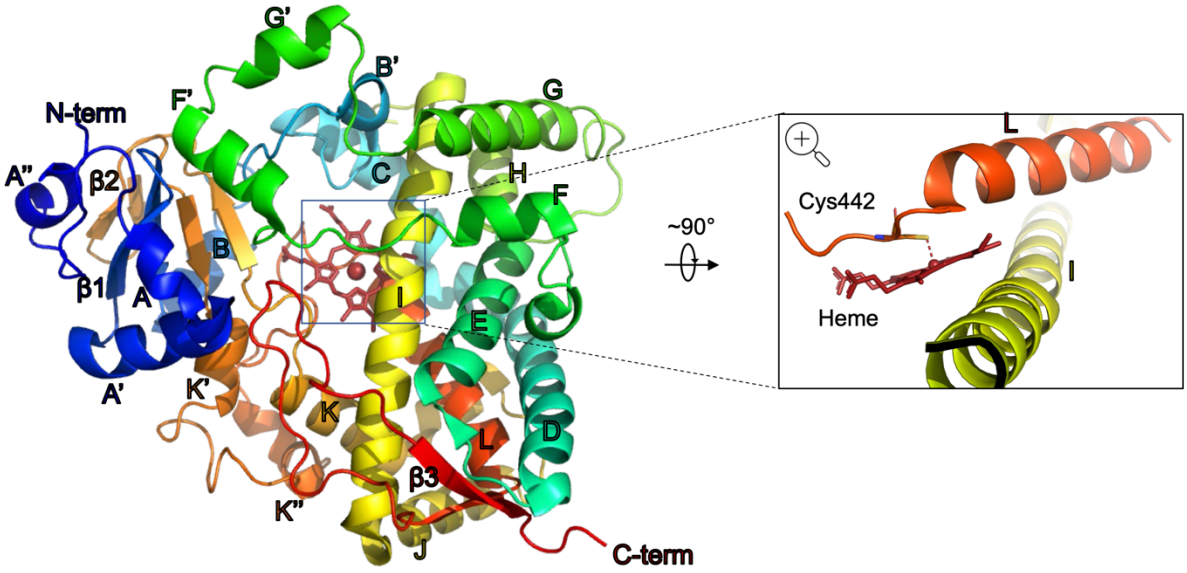

Figure 1.6.3. The cytochrome P450 fold. The ligand-free structure of CYP3A4 (PDB ID: 1TQN). is featured as a representative P450 enzyme in a bottom-up view (left). The heme porphyrin and iron are shown in brick-colored stick and sphere representation, respectively. The zoomed in area shows the conserved cysteine residue on the loop preceding the L-helix that coordinates axially to the heme iron (right).

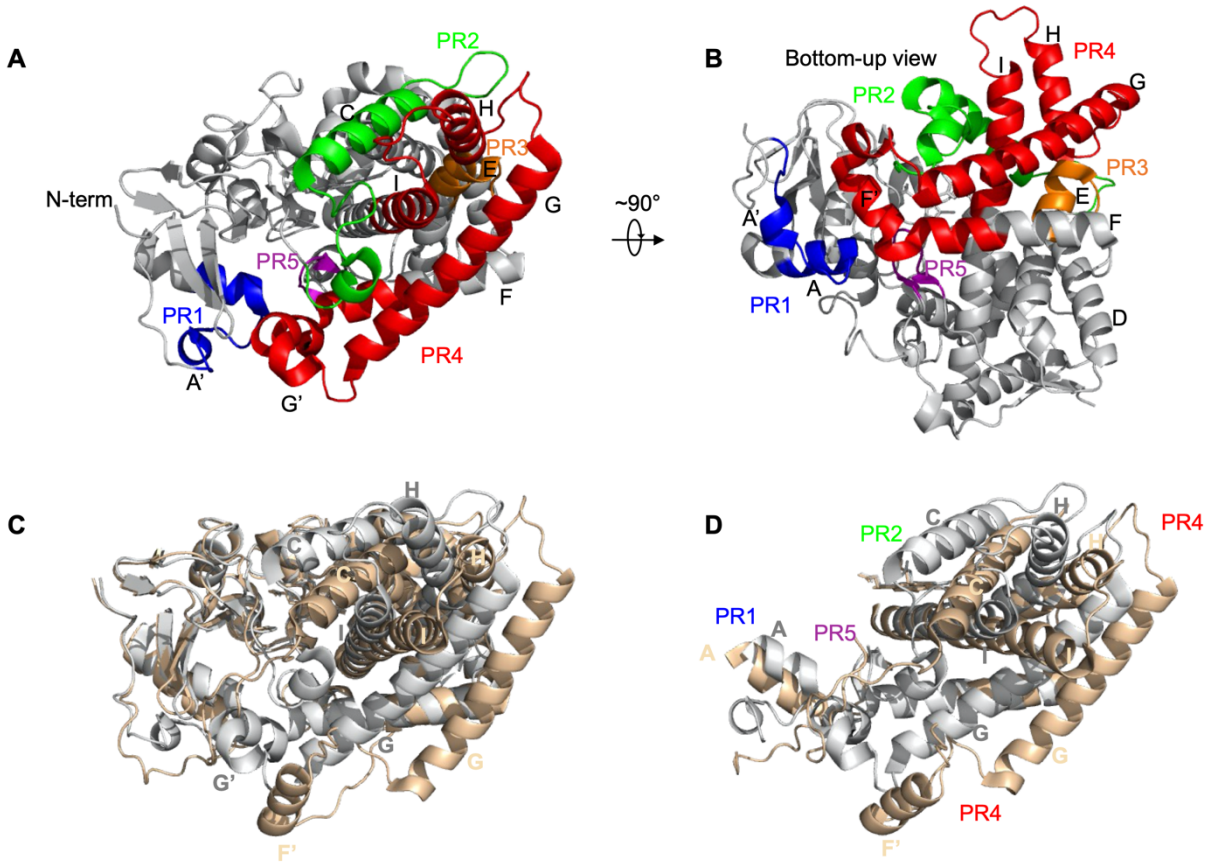

Figure 1.6.4. Conformational plasticity of cytochrome P450 2B4. A, B) The P450 plastic regions (PR-s) identified in CYP2B enzymes by Zhao *et al*. [67] mapped onto the crystal structure of CYP2B4 bound to 4-CPI (PDB ID: 1SUO) in two orientations. The plastic regions include: PR1 (residues 39-57) in blue, PR2 (residues 101-140) in green, PR3 (residues 177-188) in orange, PR4 (residues 203-298) in red, and PR5 (residues 474-480) in purple. **C**) Superimposed crystal structures of CYP2B4 bound to 4-CPI (gray, PDB ID: 1SUO) and bifonazole (wheat; PDB ID: 2BDM). **D**) The superimposition of structures in C is shown only at the PR-s where the largest conformational changes between the two bound CYP2B4 structures occur.

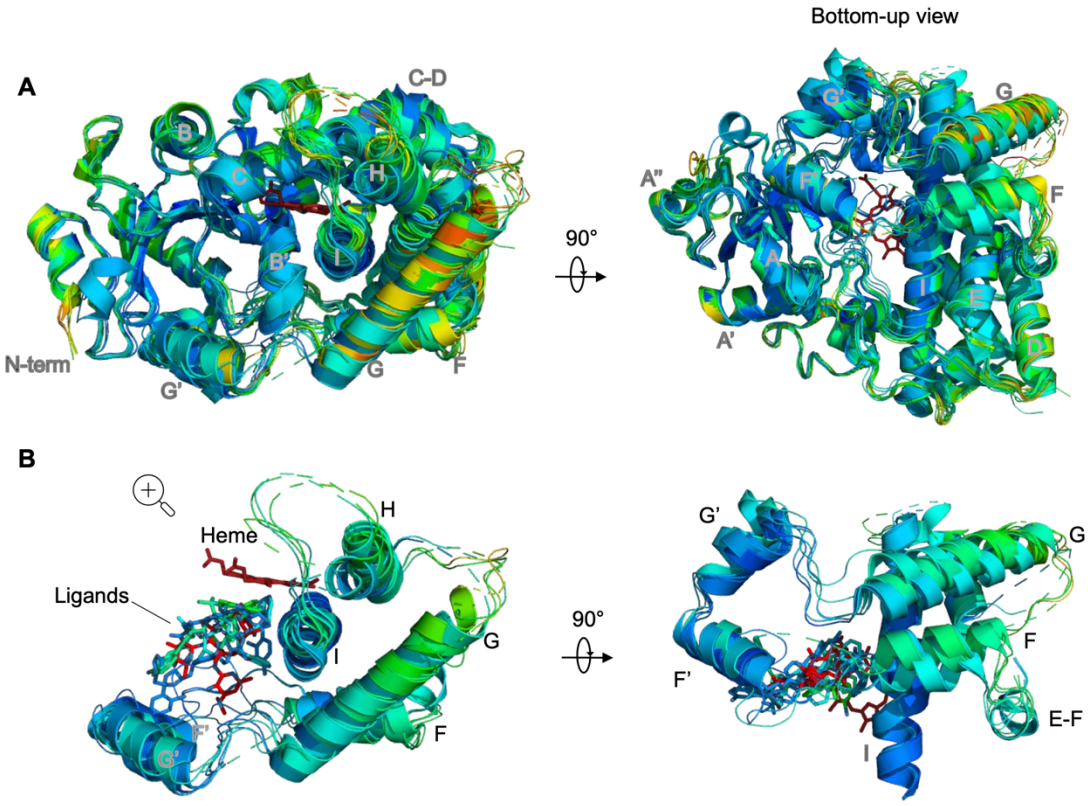

Figure 1.6.5. **Conformational plasticity of cytochrome P450 3A4. A)** Superimposed crystal structures of CYP3A4 in the free state and bound to bromocriptine, midazolam, ketoconazole, ritonavir, and erythromycin in two orientations (PDB ID-s in order: 1TQN, 3UA1, 5TE8, 2V0M, 3NXU, 2J0D). The structures are colored on a blue (low) to red (high) B-factor scale and the heme is shown in brick-colored stick representation. **B)** A zoomed in view of the F-G and H-I regions from the overlay of structures in A, where the most significant differences in CYP3A4 conformation occur. The ligands are shown in stick representation in their bound position.

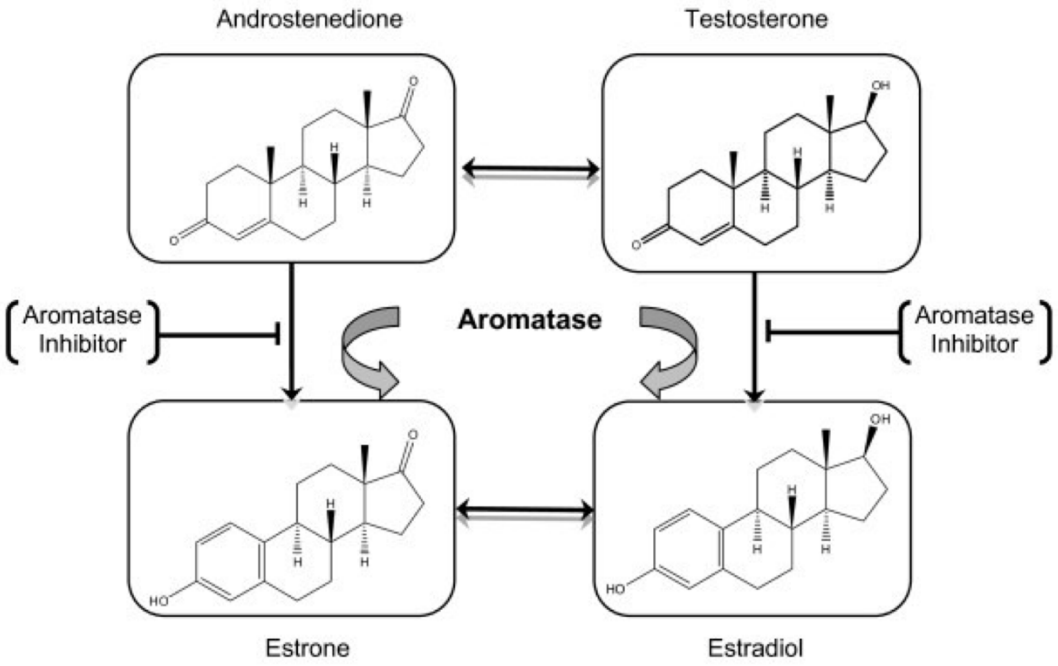

Figure 1.6.6. **The conversion of androgens to estrogens by P450 aromatase.** Scheme from [136]**.**

1.7 TABLES

Table 1.7.1. Classification and characteristics of human P450 isoforms.

Major substrate class	Xenobiotics	Sterols, Fatty acids, Eicosanoids, Vitamins
P450 isoforms	1A1, **1A2** 2A6, 2A13 2B6 2C8, **2C9**, 2C18, **2C19** **2D6** **2E1** 2F1 **3A4**, 3A5, 3A7, 3A43	1B1* 2J2*, 2U1, 2R1 4A11, 4B1, 4F11, 4F12, 4V2, 4F2, 4F3, 4F8 5A1 7A1, 7B1 8A1, 8B1 11A1*, 11B1, 11B2 17A1 19A1 21A2 24A1* 26A1, 26B1, 26C1 27A1, 27B1, 27C1 46A1*
Interindividual Variability	High	Low
Substrate Selectivity	Broad	Narrow
Phenotypic consequences of mutations	Less serious, substrate-dependent	Typically cause serious diseases

Chapter 2. LIGAND-DEPENDENT STRUCTURAL DYNAMICS OF NANODISC-EMBEDDED CYP3A4

2.1 INTRODUCTION

Human cytochrome P450 3A4 is a major detoxification enzyme, transforming ~45% of xenobiotics metabolized by P450 enzymes, and ~30% of small molecule drugs overall [62]. In addition to its contribution to xenobiotic metabolism, 3A4 also plays a major role in unwanted drug-drug and drug-food interactions, and as a result, is a critical consideration in drug design and development [144]–[148]. Despite the availability of numerous X-ray structures, it has been challenging to predict metabolism of drugs by 3A4 due to its extreme ligand promiscuity that may be affected by variables such as the oligomeric state of the enzyme [149], [150], presence or absence of redox partners [151], membrane composition [152]–[154], and co-solvent conditions [155], [156]. Each of these factors also affects the well-established homotropic and heterotropic allosteric properties of 3A4 that are also promiscuous and enigmatic [133].

One frequently suggested mechanism by which detoxification enzymes achieve ligand promiscuity is with their conformational 'flexibility' [157]. 3A4 has long been described as a flexible enzyme with a large hydrophobic active site that can accommodate multiple ligands and multiple ligand orientations [66], [129], [158]. Evidence for the flexibility of the enzyme primarily stems from crystal structures of 3A4 bound to various ligands showing large local deviations from the free structure that vary in direction and magnitude. The expanding collection of P450 crystal structures has revealed that significant local rearrangements in the presence of ligands are not

unique to 3A4, and P450s of varying substrate selectivity have been shown to inhabit diverse conformations [71], [74], [119], [159], [160], prompting a need for a more rigorous assessment of the role of conformational flexibility in promiscuous interactions with ligands. Beyond static structures, investigation of the dynamic properties of 3A4 has been primarily limited to computational and spectroscopic methods with select ligands and the range of ligand-dependent effects on the backbone dynamics is not established [27], [68], [102], [105], [161]–[166].

Previously, our laboratory has used hydrogen-deuterium exchange mass spectrometry (HDX-MS) to analyze 3A4 dynamics incorporated in lipid nanodiscs in the absence and presence of ligands [102], [163]. HDX refers to the exchange reaction of protein backbone amide hydrogens with deuterium from solution. When coupled with sensitive detection methods such as NMR or MS, HDX is a valuable tool that reports on the accessibility of amide hydrogens and provides insights into the conformational dynamics of proteins in different states [167], [168]. HDX-MS has been particularly advantageous in probing the dynamic behavior of proteins like 3A4 that are difficult to study by other methods, as it poses no size limitation, avoids invasive labeling methods, and allows for incorporation of membrane-bound proteins in model membrane systems. A disadvantage of the technique lies in the interpretation of HDX outcomes. While it is understood that the main factor that dictates slow exchange of an amide hydrogen with deuterium is whether the amide hydrogen is hydrogen-bonded, other factors such as solvent accessibility, residue packing density, and local electrostatic effects may influence the rate of HDX and make interpretation of results challenging. Nevertheless, when combined with other methods such as molecular dynamics simulations, HDX-MS is a powerful technique for corroborating local and global dynamic information at peptide resolution.

HDX-MS with 3A4 in nanodiscs revealed an HDX profile that was consistent with the expected flexibility pattern of 3A4 derived from crystal structures and MD simulations [102]. Slow exchanging peptides included parts of the protein core at the I, L, and K helices, and the membrane-embedded F'-G' motif, whereas fast exchanging ones corresponded to the C-terminal loop and connecting regions in the stretch of secondary structure between the E and I helices (H-I, G-H, E-F, and D-E) (Figure 2.5.1). The E-I fragment of 3A4 forms the largest P450 plastic region[3] (PR4) that along with PR5 at the C-terminus have the most variable conformations in crystal structures of 3A4 bound to ligands (Figure 1.6.5). Two 3A4 ligands, ketoconazole, a type II[4] inhibitor, and midazolam, a type I substrate and allosteric effector, had subtle but distinct effects on 3A4 dynamics that were globally distributed in the protein structure [102], [163]. Some peptides were affected by both ligands, whereas others were uniquely affected by either ketoconazole or midazolam. Based on the complex global HDX responses, we postulated that some dynamic responses of 3A4 may be essential for all ligand binding, while others are ligand dependent.

Here, we report the effects of six ligands on the conformational dynamics of 3A4 embedded in POPC lipid nanodiscs (NDs), as probed by HDX. Ligands were selected to represent a range of chemical structures and functions to reflect the vast repertoire of 3A4-ligand interactions (Figure 2.5.2, Table 2.6.1). We also included ligands for which crystal structures are available for their bound complexes to compare with behavior in a membrane. The ligands studied were ritonavir, nifedipine, bromocriptine, miconazole, azamulin and testosterone. Ritonavir (RIT) is an HIV antiviral protease inhibitor and potent 3A4 inactivator [169]. Nifedipine (NIF) is an

[3] Plastic regions are described as originally defined for the CYP2 enzymes [160].
[4] A type II ligand induces a red shift in the UV/VIS spectrum of the resting state P450 heme, by replacing water as the fifth axial ligand coordinating to the heme iron. A type I ligand induces a blue shift in the P450 spectrum by displacing the axial water and shifting the heme geometry from a hexa-coordinated to a penta-coordinated heme iron.

antihypertensive calcium channel blocker drug and a marker substrate of 3A4 [170]. Bromocriptine (BEC) is a dopamine receptor agonist that acts as substrate and inhibitor of 3A4 [171]. Miconazole (MIC) is an azole antifungal drug and inhibitor of 3A4 [172]. Azamulin (AZA) is a pleuromutilin antibiotic and suicide substrate of 3A4 that was discontinued after Phase I trials due to potent 3A inhibition [173]. Lastly, testosterone (TST) is a well-characterized marker substrate and allosteric effector of 3A4 [174]. With these ligands we performed a correlational analysis of HDX effects to screen for ligand-mediated correlated motions in 3A4.

2.2 METHODS

Materials and chemicals

Reagents were purchased from Sigma or Fisher unless otherwise stated. Ritonavir and bromocriptine were obtained from Apexbio and Santa Cruz, respectively. Deuterium oxide "100%" was obtained from Cambridge Isotope Laboratories. Solvents for LC-MS/MS were Optima LC/MS grade, other water used was from a Barnstead nanopure UV dispenser.

CYP3A4 and MSP1D1 expression and purification

Recombinant CYP3A4 and MSP1D1(-) were expressed and purified as previously described [102], [175]–[177]. *E. coli* C41(DE3) cells were transformed with a pCWori+ vector encoding genes for the Nf14 CYP3A4 construct and ampicillin resistance. The Nf14 construct has an N-terminal Δ3-11 deletion and a C-terminal 5xHis tag [178]. Following expression, cells were centrifuged at 6,650 x g at 4˚C for 30 min, and pellets were stored at -80°C until purification. Unless otherwise stated, the purification steps were carried out in the dark at 0-4°C with pH 7.4 buffers. β-mercaptoethanol (βME), TST and non-ionic detergents were added immediately before use. Cell pellets were gently resuspended in lysis buffer (20 % glycerol v/v, 100 mM KPi, 10 mM βME, 100 μM TST, 3% Emulgen 913, 20 mM imidazole) supplemented with 2 mg/ml lysozyme,

10 μl/ml protease inhibitor cocktail for His-tagged proteins and 0.1 μl/ml benzonase nuclease. Resuspended cells were stirred for 1 hour, passed (2x) through a handheld Potter-Elvehjem homogenizer, and stirred for 4 additional hours. After ultracentrifugation at 100,000 x g for 1 hour, the supernatant was loaded overnight onto a ~30 ml His60 Ni Superflow (Clontech) column pre-equilibrated with wash buffer 1. Following washing with 8-10 column volumes of wash 1 (20% glycerol (v/v), 50 mM KP_i, 2 mM βME, 50 μM TST, 0.2% Anapoe $C_{12}E_{10}$, 300 mM KCl, 20 mM imidazole [IMZ]), 8-10 column volumes of wash 2 (20% glycerol, 50 mM KP_i, 2 mM βME, 50 μM TST, 0.1% sodium cholate, 300 mM KCl, 20 mM IMZ, 100 mM glycine), and 20 column volumes of wash 3 (20% glycerol, 50 mM KP_i, 2 mM βME, 50 μM TST, 0.1% sodium cholate, 40 mM IMZ), 3A4 fractions were eluted with a linear IMZ gradient (20% glycerol, 25 mM KP_i, 2 mM βME, 50 μM TST, 0.1% sodium cholate, 50-500 mM IMZ). Red fractions were diluted 1:1 v/v with a cold solution of 20% glycerol and 0.1% cholate to lower the concentration of KP_i before loading onto a ~25 ml hydroxyapatite (HA) column pre-equilibrated with 20% glycerol, 10 mM KP_i, 0.1% sodium cholate, and 2 mM βME. After washing the HA column with 20 column volumes of 20% glycerol, 25 mM KP_i, and 2 mM βME, 3A4 fractions were eluted with 20% glycerol, 400 mM KP_i, and 2 mM βME. Fractions were analyzed via SDS-PAGE, pooled accordingly, and dialyzed into 3A4 storage buffer (100 mM KP_i, 20% glycerol, 0.5 mM tris-carboxyethylphosphine (TCEP), 1 mM EDTA). The 3A4 concentration was determined by measuring the difference in absorbance between the CO-bound ferrous (reduced) 3A4 and unbound ferrous 3A4 as follows: $\Delta Abs_{(450\ nm - 490\ nm)}$ of Fe^{2+}:CO – $\Delta Abs_{(450\ nm - 490\ nm)}$ of $Fe^{2+} = \varepsilon \times b \times c$, where $\varepsilon_{450} = 91\ mM^{-1}\ cm^{-1}$ [179]. No P420 was detected based on the absorbance at 420 nm.

E. coli BL21-Gold (DE3) cells were transformed with a pET vector encoding genes for MSP1D1 and kanamycin resistance. Cells were harvested at 6,650 x g at 4˚C for 15 min.

Purification steps were carried out at 4˚C. Cell pellets were resuspended in lysis buffer (20 mM KP_i, pH 7.4, 1% Triton X-100) supplemented with 2 mg/ml lysozyme, 10 µl/ml protease inhibitor cocktail, 0.1 µl/ml benzonase nuclease, and lysed twice with a French Press. After ultracentrifugation for 45 min at 45,000 g, the supernatant was loaded overnight onto a ~25 ml His60 Superflow Ni column pre-equilibrated with wash buffer 1 (40 mM Tris, pH 8.0, 300 mM NaCl, 1% Triton X-100). Following washing with 5-7 column volumes of wash buffer 1, 5 column volumes of wash buffer 2 (40 mM Tris, pH 8.0, 300 mM NaCl, 50 mM cholate, 20 mM IMZ), 5 column volumes of wash buffer 3 (40 mM Tris, pH 8.0, 300 mM NaCl, 50 mM IMZ), MSP1D1 was eluted with a linear IMZ gradient (40 mM Tris, pH 7.4, 300 mM NaCl, 40-400 mM IMZ). MSP1D1 containing fractions were pooled, concentrated, and dialyzed into MSP1D1 storage buffer (20 mM Tris, pH 7.4, 100 mM NaCl, 0.5 mM EDTA). The MSP1D1 concentration was spectrally determined using the extinction coefficient of 21 mM^{-1} cm^{-1} [177].

The His tag of MSP1D1 was cleaved to yield MSP1D1(-) as previously described [177], [180]. Following the cleavage reaction with Pro-TEV Plus Protease (Promega), the reaction mix was filtered through a 0.2 µm filter and buffer exchanged into column running buffer (40 mM Tris, pH 8.0, 300 mM NaCl, 50 mM cholate), before loading onto a ~8 ml His60 Superflow Ni column pre-equilibrated with running buffer, collecting the flowthrough. After washing with 3 column volumes of running buffer, the combined flowthrough with MSP1D1 (-) was buffer-exchanged into storage buffer (40 mM Tris, pH 8.0, 300 mM NaCl), concentrated to ~150 µM and stored at -80°C until nanodisc preparation. The pure MSP1D1(-) was characterized via SDS-PAGE and the concentration was spectrally determined using the extinction coefficient of 18.2 mM^{-1} cm^{-1} [177].

Nanodisc preparation

3A4-NDs containing POPC lipids were prepared as previously described with few modifications [102], [163], [177]. Briefly, POPC powder (Avanti Polar Lipids) was dissolved in chloroform (~2 g/ml) and the concentration of phospholipids was determined by measuring the total phosphorous [177]. To make the lipid film, POPC chloroform stock was placed under a gentle N_2 stream in a glass tube while twirling the tube at an angle until a thin layer of film was formed. The film was dried overnight in a vacuum desiccator to remove traces of chloroform and solubilized in cholate by intermittent sonicating, low heat, and vortexing, until the solution was clear. In the meantime, 3A4 was treated with 0.1 % Emulgen 911, and left to nutate in the dark at RT for 1 hr, before exchanging into disc-forming buffer (DFB; 100 mM KP_i, 50 mM NaCl, pH 7.4) supplemented with 0.1% Emulgen 911. To prepare the ND reaction mix, cholate-solubilized lipids, MSP1D1(-) and 3A4 were mixed in an empirically determined ratio (55:1:0.1). More cholate and DFB were added for a final 3:1 cholate: lipid ratio. The reaction mix was rotated at 4 ˚C for 1 hr and transferred to 2 x 10 ml capped centrifuge columns (Pierce) containing 1 g/ml pre-rinsed Amberlite XAD-2 beads to initiate the nanodisc assembly. The disc and beads mixtures were gently rotated at 4 °C for 6 hrs. To separate the NDs from the beads, the columns were uncapped and spun down at low speed inside 50 ml Falcon tubes. The beads were rinsed twice with DFB and the collected flowthrough containing the NDs was filtered with a 0.2 μm filter. To remove leftover detergents, NDs were dialyzed three times against 1 L of DFB with 2 mM βME (2 x 1 hr, overnight) before loading onto a 5 ml His60 Ni Superflow column pre-equilibrated with DFB. After washing with 3-5 column volumes of DFB and 3-5 column volumes of DFB+20 mM IMZ, red fractions were eluted with DFB+300 mM IMZ, and concentrated to 8-9 ml before injecting into a Superdex 200

10/300 GL column pre-equilibrated with DFB+2 mM βME for further purification by SEC. The pure fractions were combined, exchanged into DFB+10% glycerol, concentrated to ~10 μM and stored at -80˚C. The concentration and P420 content were spectrally determined as described for pure 3A4. No P420 species was detected.

HDX sample preparation

HDX was performed as previously described [102], [181] with six ligands in two groups (I) RIT, NIF, and BEC, and (II) MIC, AZA and TST. The split into groups was due to it not being experimentally feasible to prepare HDX samples for the six ligands together. Ligand-free 3A4-ND samples were included in each group. Free or bound 3A4-NDs were exchanged at 24˚C for 30 s, 5 m, and 90 m in duplicate, in random order. Details of the HDX reactions are reported in Tables 2.7.2 and 2.7.3. To initiate the exchange reaction, a 10 μl aliquot of free or bound 3A4-NDs, pre-incubated at 24˚C for 30 min, was mixed with 90 μl of deuterated HDX buffer (50 mM HEPES, pH 7.0, 50 mM NaCl, 2 mM TCEP). The concentration of ligands and 3A4-NDs in the 100 μl HDX sample were ~20× their reported K_D values and 0.9 -1.2 μM, respectively. Final deuterium content (D_{frac}) was 83.2%. The exchanged sample was quenched with 100 μl of ice-cold quench solution (1.2% formic acid and 0.4% TFA) and transferred to pre-rinsed immobilized pepsin beads (Pierce) on ice. To prepare the beads, a 200 μl aliquot of 1:1 pepsin slurry was spun at 14,000 g for 30 s in a chilled microcentrifuge. After discarding the liquid, 400 μl of 0.8% formic acid was added to the beads and the slurry was centrifuged for another 30 s. The liquid was decanted, and the rinsed beads were returned on ice. 4.2 μl of 250 mM cholate in HDX buffer was added to the cap of the pepsin tube. The quenched sample was digested on ice for 5 m with rapid vortexing every 30 s. At 4 m, 10 μl of 300 mg/ml ZrO_2-coated silica resin beads in 0.8% FA was added to facilitate POPC removal. At 5 m, the mix was transferred to a 2 ml centrifuge tube filter (Corning,

pore size 0.45 μm) and centrifuged at 14,000 g for 30 s. 200 μl of flowthrough was rapidly transferred, flash frozen in LN_2, and stored at -80°C until MS analysis.

HDX Mass Spectrometry

Samples were thawed on ice for 5 m and at room temperature for 80-100 s before injecting into an in-house mobile LC system kept at 1˚C [182]. Peptides were loaded onto a BEH Shield RP18 Vanguard trap column (Waters, 1.7 μm particle size, 2.1 x 5 mm) by flowing loading buffer (0.1% FA, 0.025% TFA in water) at 200 μl/min for 5 min and then separated on a Hypersil GOLD C_{18} column (1.9 μm particle size, 50 x 1.0 mm) at 40 μl/min for 10 min using a 2-50% gradient of solvent B (A: 2% CH_3CN, 0.1% FA, 0.025% TFA in water; B: 0.1% FA in CH_3CN). To minimize carry-over, the syringe, LC lines, and columns were extensively washed as previously described [103]. C_{18}-separated peptides were directed to a Waters Synapt G2-Si Q-TOF mass spectrometer with ion-mobility enabled for MS analysis. Source and StepWave ion guide settings were adjusted to minimize gas-phase deuterium loss [183]. A Thermo LTQ-Orbitrap (resolution 60,000) was used to analyze undeuterated samples by MS/MS.

HDX data and correlation analysis

Peptide assignments were made using MS^E data with PLGS Version 3 [102] and MS/MS data with Protein Prospector. Retention and drift times were identified with Drift Scope 2.0. HX-Express v2 was used to analyze and summarize deuterium uptake of peptides by binomial fitting of the raw spectra [184]. Multiple charge states and overlapping peptides were analyzed and manually curated to exclude noisy or hard to separate peptides. ΔHDX values were calculated by subtracting the deuterium uptake of peptides in the free state from the bound state. Fully deuterated samples were not obtained due to the primary goal of the study being to compare different bound states of CYP3A4. A statistical threshold for a significant difference in HDX between two states was

calculated in the form of a 95% confidence interval (CI) based on the average standard deviation of the pooled data [168], [185], as detailed in Tables 2.7.2 and 2.7.3.

Heatmap of correlation matrix of the sum ΔHDX for peptides in different bound states was generated in GraphPad Prism 9 using the correlation matrix analysis tool to compute Pearson correlation coefficients. Two-tailed p values were used to assess confidence. A Bonferroni correction was used to correct the standard p value of 0.05 to account for multiple comparisons (0.05/number of pairwise comparisons). Peptides that were not significantly affected according to the significance thresholds established in the HDX analysis were excluded to avoid false positives. The chiclet plot was manually constructed in PowerPoint (2021). Protein structures were generated in PyMOL 2.5.

2.3 RESULTS

Global dynamics of 3A4-NDs

HDX-MS was performed with 3A4-NDs mixed with co-solvent or six ligands: RIT, BRO, NIF, MIC, AZA, and TST. The 30 s – 90 m HDX reaction time course was chosen based on previous work and preliminary data corrected for back-exchange of the deuterium label showing that HDX proceeds to >70% for most peptides within 90 m (unpublished). Relative deuterium uptake is reported for 65 peptides that cover 89.3% of the Δ(3-11)-CYP3A4 sequence or 79.4% of the backbone amide hydrogens. (The first two residues of a peptide quickly back-exchange the deuterium label and are not detectable by HDX). Uncovered regions include the N-anchor-A'' loop and parts of the buried I and L-helices. Sequence coverage and deuterium uptake profiles are consistent with previous work.

General ligand-mediated effects on HDX of 3A4

The differences in the relative deuterium uptake of the bound and free states are summarized in a chiclet plot in Figure 2.5.3. Effects of ligands on 3A4 dynamics are globally distributed in flexible connecting elements of 3A4 between stretches of secondary structure. All the ligands affect the F-G, and to a lesser extent, the C-D, and H-I regions of the protein, suggesting that backbone fluctuations in these regions play a key role in accommodating the different ligands as suggested by the crystal structures.

The most common ligand-induced change is an *increase* in HDX or deprotection in the F-helix and loops that connect to the E-helix and F'-helix (peptide 193-213) (Figures 2.5.3, 2.5.4). This peptide is part of the flexible F-G cassette and contains part of the F-F' loop that along with G-G' loop, form the 'lid' of the active site and play a key role in accommodating diverse ligands in the binding pocket. The extent to which the F-helix peptide is affected by HDX is ligand-dependent, with ritonavir causing the smallest increase in HDX and azamulin the largest. An adjacent peptide containing the C-terminus of the E-helix and the E-F loop is also deprotected with ligands (Figure 2.5.4, peptide 2). In a recent HDX analysis by Ducharme *et al* of 3A4 in solution, the E-helix peptide 182-189 was one of the most protected peptides when 3A4 was bound to either CPR or ligands [105]. In the present work, the E-helix peptide undergoes very slow exchange until the 90 m time point in the exchange reaction, whereas it appears to exchange faster in the Ducharme analysis. In a comparison of 3A4 in solution and in NDs, Treuheit *et al*. reported that the exchange profiles were similar for most peptides, except for the E-F-G region which exchanged more slowly in the nanodisc-embedded 3A4 [102]. Thus, the E-helix is likely in a different conformation when 3A4 is in a membrane environment. Interestingly, various naturally occurring

SNPs are concentrated on the E-helix [186], [187], and it is known to adopt a different conformation in differentially expressed 3A4 [188].

On the other hand, the C-terminal half of the G-helix (peptide 249-261) typically shows a *decrease* in HDX or is protected, with 'type II' (i.e., heme-coordinating) ligands ritonavir and miconazole causing the largest protection, and azamulin the smallest (Figures 2.5.3). The G-helix was also strongly protected with ketoconazole, another type II ligand, in previous work [102]. Exchange profiles from overlapping peptides 249-271 and 262-271 indicate that the observed difference in HDX is likely due to the 251-263 portion of the G-helix since deuterium uptake of peptide 262-271 (G-H loop) is not significantly affected by ligands.

Another commonly affected region is the C-terminal half of the C-helix (Figures 2.5.3, 2.5.4). Overlapping peptides 126-133 and 126-137 show that the reported HDX difference is mainly due to the 133-137 portion of the C-helix that connects to the neighboring D-helix. The N-terminal half of the C-helix and the preceding B'-C loop that makes contacts with ligands in the active site exchange deuterium poorly and are characterized by low B-factors in the crystal structures. It is possible that the changes observed at the C-D region are propagated there via movements of the C-helix or B-C loop in the active site. Intriguingly, the HDX effect at the C-D region of CYP3A4, is most dominant for the type II ligands, ritonavir, and miconazole. Deprotection of the C-helix was also observed for ketoconazole [102] . The HDX effects of the type II ligands at the C-D region may be functionally relevant as it has been suggested that the C-D loop contributes to the binding interface with redox partner CPR for some P450 enzymes. The electron transfer from CPR to P450s is triggered by the change in redox potential of the heme iron upon binding of the substrate (typically, a type I ligand) which does not occur when the enzyme is inhibited with a type II ligand. Based on NMR of a complex of flCYP2B4 with the flavin-binding

domain of CPR in peptide 4F-lipid DMPC NDs, and previous site-directed mutagenesis, Prade *et al*. reported that most of the binding surface of flCYP2B4 with the FMN domain of CPR consists of residues R133, F135, M137, and K139 in the C-D loop, along with other residues in the proximal loop near the heme [189]. While the binding interaction with CPR has been studied for several mammalian P450s including 3A4 [152], [190], 17A1 [191], [192], 19A1 [193] 2D6 [81], 1A1 [194], 1A2 [195], 2B4 [189], [196], [197], and 2B6 [198], the specific 3A4 residues that interact with CPR have not been identified. The HDX effects at the C-D region suggest ligand-mediated modulation of dynamics at a potential interface with redox partner, CPR.

Lastly, the H-I loop region (peptide 275-292) is deprotected with all ligands in the early time points of the exchange reaction (Figures 2.5.3, 2.5.4). The H-I loop is highly flexible and not fully resolved in any of the 3A4 crystal structures. It is likely that changes are propagated at this loop via the N-terminus of the I-helix which is known to 'bend' or locally distort in structures with different ligands.

Except for the F-helix peptide that contains a portion of the F-F' loop (peptide 193-213), the ligand-mediated HDX effects on 3A4 are not in the active site (Figure 2.3.4). Four of the five peptides are in PR4. Each of the peptides flank substrate recognition sites (SRS) and is characterized by high B-factors in available crystal structures. Collectively, the results suggest that the E-F, G-H, and C-D regions act as "adjustable straps" that tailor their conformation in response to disrupting events in the protein environment to maintain their relative packing.

Specific ligand-mediated effects on HDX of 3A4

Peptides that are significantly affected by only one of the ligands studied are typically located in the active site between the heme and membrane-interface (Figure 2.5.4), reflecting differences in

the specific binding modes of each ligand. For instance, azamulin causes the deprotection of several peptides spanning the F'G'-G region (Figures 2.5.3, 2.5.4) as expected based on a crystallographic model. A crystal structure of the azamulin-3A4 complex showed little deviation from the free state except for the disordering of the F'-helix due to a steric clash of azamulin with the F-F' loop [199]. Consequently, the F-F' loop does not seal the active site and is exposed to the bulk solvent. In this work, the F'-G' motif is deprotected by azamulin suggesting that the F'-helix is indeed at least partially disordered in near-native conditions. In unpublished MD simulations performed by Hackett, azamulin strongly activates the dynamics of the F-F' region. MD simulations with ritonavir revealed no such effect in the same region.

Other uniquely affected peptides are found in the B-C loop that contains the long B-B' loop, B'-helix and shorter B'-C loop. The region is part of PR2 and contains the functionally important Ser119 residue which is known to make side chain-mediated contacts with ligands in the active site and helps dictate their final configuration in the bound complex [84], [164]. In our analysis, PR2 is characterized by medium-low exchange and a similar trend can be seen by the medium-low B-factors in the crystal structures. Peptides 114-122 and 114-125 that contain the B'-C loop exchange slowly for all the ligands but miconazole. The exchange profiles of the B'-C loop peptides in the miconazole complex appear bimodal, indicating at least two conformations of the loop in the presence of miconazole (Data not shown).

The longer BB' loop is modestly protected from exchange with bromocriptine (Figure 2.5.4). Despite its large size, bromocriptine fits in the active site without significantly affecting the backbone configuration of 3A4. The crystal structure of the bound complex is almost identical to that of the free 3A4 (Cα RMSD = 0.29 Å) [200]. Similarly, the HDX data show modest changes in the 3A4 bromocriptine complex. The protection of the BB' loop may be due to an orthosteric

interaction with the indole end of bromocriptine that extends towards the loop. It should be emphasized that the BB' loop readily exchanges deuterium, yet is minimally affected by most ligands, suggesting that the backbone of the BB' loop does not significantly change conformation in the presence of ligands.

Peptides 34-51 and 34-52 that contain the A''-A' loop and part of the A'-helix are the only peptides that, depending on the ligand, are either protected (ritonavir, bromocriptine), deprotected (azamulin), or not significantly affected (nifedipine, miconazole and testosterone). (Figures 2.5.3, 2.5.4). The loop is part of PR1 which in 3A4 is not flexible [68] and is characterized by medium-low B-factors. In our HDX analysis the loop is dynamic and readily exchanges with deuterium. The dynamics of the loop are likely linked to the neighboring A'-A turn motif that contributes to contacts with larger ligands in the active site. In the case of azamulin, where such contacts are absent as azamulin points away from the A'-A turn in the crystal structure, the deprotection of A''-A' loop may be due to the increased disorder and solvent exposure at the nearby F'-G' motif upon azamulin binding as discussed above. Finally, MD simulations of full-length 3A4, place the A''-A' loop in the membrane [201], [202]. It is therefore likely that the dynamics of this region are sensitive to the surrounding lipid environment and the partitioning of hydrophobic ligands between the membrane and protein domains.

Modest ligand-dependent HDX differences are observed in the K-β1 loop (peptide 364-371), C-terminus loop (471-491), the D-E region (peptides 138-151, 157-176, 173-182), J-J' loop (337-351), and proximal loop near the heme (429-444). The protection at the K-β1 loop is likely due to orthosteric contacts with ligands in the active site, as observed with ketoconazole and midazolam. The HDX effect of ligands at the K-β region in the active site is likely underestimated due to the 364-371 peptide exchanging very slowly at all states.

Correlated motions of the G-helix and C-D region

To determine whether correlated motions are present in different forms of ligand-bound 3A4, we performed a correlation analysis of the sum of differences in deuterium uptake at 30 s, 5 m, and 90 m for the peptides that were significantly affected by ligands. To avoid false positives, correlation factors for peptides that were affected by at least 5 ligands are reported. As expected, overlapping peptides (157-176 and 157-178, 190-213 and 193-213, 249-261 and 249-271) showed the strongest correlation (Figure 2.5.5A). More interestingly, there is a strong anti-correlation between non-overlapping peptides in the G-helix (peptide 249-261) and the C-D region (peptide 126-137) (Figure 2.5.5A-C). Despite being more than 13 Å apart, the strong protection at the G-helix correlates well with deprotection of the C-D region (R^2=0.91, p = 0.0033). The anti-correlation is most pronounced with type II ligands ritonavir and miconazole, but other ligands including previously published midazolam, ketoconazole and ANF (unpublished) follow this trend.

This anti-correlation indicates that the ligands that protect peptide 249-261 the most, do so at the expense of deprotecting peptide 126-137, and vice-versa. The observed anti-correlation is intriguing, especially since the C-D region and G-helix do not display similar dynamic profiles in ligand-free 3A4, as evidenced by a lack of correlation in absolute HDX at the two regions.

2.4 DISCUSSION

It is widely accepted that the conformational flexibility of 3A4 is important for its extreme ligand promiscuity, but detailed models for ligand-dependent dynamics in a membrane have until now been limited to MD simulations [152], [161]. Here, we performed HDX-MS on CYP3A4 in lipid

NDs bound to six ligands to understand how the dynamics of the monomeric enzyme in a membrane bilayer respond upon binding diverse ligands. The results demonstrate that the effects of ligands are the largest in the most flexible elements of the secondary structure that do not contact the ligands directly in the bound state. This suggests that ligands differentially engage some of the flexible elements of the structure (C-D, E-F, G, H-I) via long-range communication pathways emanating from the active site to accommodate the ligands accordingly. Speculatively, by delegating most of the conformational rearrangement to the flexible regions of the protein, the enzyme avoids the entropic and functional cost of reconfiguration of the rigid heme core.

The largest effects on dynamics were the deprotection of the F-helix and connecting loops and the protection of the C-terminal residues 251-261 of the G-helix. The results highlight the fact that the changes in the F-G region are not unique to allosteric ligands such as midazolam and testosterone. Patterns emerge in which type II ligands ritonavir and miconazole have similar HDX effects. Both ligands cause a pronounced protection of the G helix and deprotection of the C-D region, which is also observed with type II ligand, ketoconazole. This is an intriguing result as it has been suggested that the type I and type II ligand binding modes for bacterial CYPs reflect a structural response of the protein and not merely the occupancy of the sixth axial ligand [99]. Even though type II ligands ritonavir, miconazole, and ketoconazole 3A4 complexes show a similar HDX profile, the observed HDX effects do not cleanly partition into type I or type II ligand responses. For instance, the HDX profile of testosterone (type I) is more like miconazole (type II) than azamulin or nifedipine (type I). In the Ducharme *et al*. analysis of 3A4 in solution by HDX, 100 μM testosterone had no apparent effect on the G-helix and caused protection of the F- (193-213) and F'-helices (221-226) [105]. Additional protective effects were observed at the B'-C loop (114-122), E-helix (182-189) and loop connecting to β1-4 strand (389-396). The latter peptides

exchange deuterium more slowly in nanodisc-embedded CYP3A4 than in solution and appear unaffected by ligands in the present analysis. The faster exchange in solution indicates that 3A4 is more dynamic when removed from a membrane environment. This observation indirectly supports the gain in stability that occurs when the enzyme is embedded in lipid NDs [203]. Thus, the discrepancies in the HDX results of testosterone-bound 3A4 in solution and in NDs highlight the important role of the lipid environment in the dynamic behavior of 3A4 and interactions with ligands. Lastly, several peptides in the Ducharme analysis appear bimodal, indicating greater population heterogeneity for 3A4 in solution, as previously observed [165].

It is notable that the HDX effects observed here are a mixture of deprotective and protective effects, with some ligands such as azamulin and nifedipine causing almost exclusively de-protective effects. An increase in HDX relative to the free state was also the most dominant effect on 3A4 dynamics with midazolam [163] and ANF (unpublished), contrasting the more intuitive decrease in HDX that results when a ligand makes stabilizing contacts with the protein backbone [167], [204]. The modest increase in HDX observed with 3A4 in complex with various ligands is in stark contrast to the sharp decrease in HDX observed with androgen-specific P450 enzyme 19A1 (Aromatase) [103]; see Chapter 3. In the case of 19A1, the native ligand androstenedione has a clear stabilizing effect on dynamics (HDX is suppressed in the bound state) that is most pronounced at the active site, access channel, and membrane interface. A similar suppression of HDX with a preferred ligand has been reported for another steroidogenic P450, 46A1, where the native ligand cholesterol suppresses HDX globally upon binding [104]. Conversely, the F-helix and C-D regions of 3A4 exhibit increased HDX with *all* ligands examined. Thus, the modest and mixed effects of diverse ligands on the dynamics of CYP3A4 likely reflect the promiscuous behavior of the enzyme and its lack of preference toward any ligand.

2.5 FIGURES

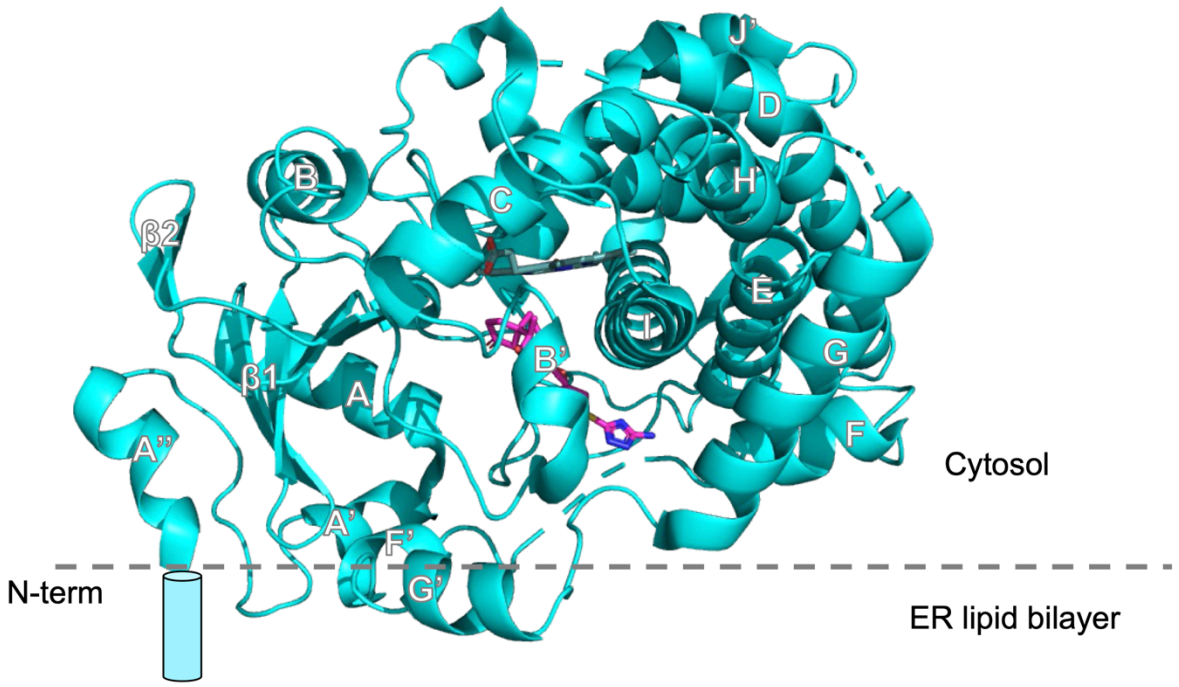

Figure 2.5.1. Structure of cytochrome P450 3A4 bound to azamulin. PDB ID: 6OOA**.** Heme and azamulin are shown in cyan and magenta stick representation, respectively.

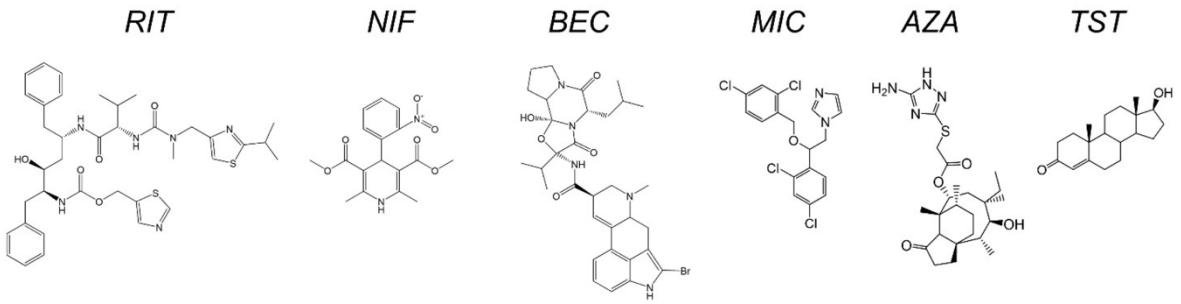

Figure 2.5.2. **Structures of CYP3A4 ligands analyzed by HDX-MS.**

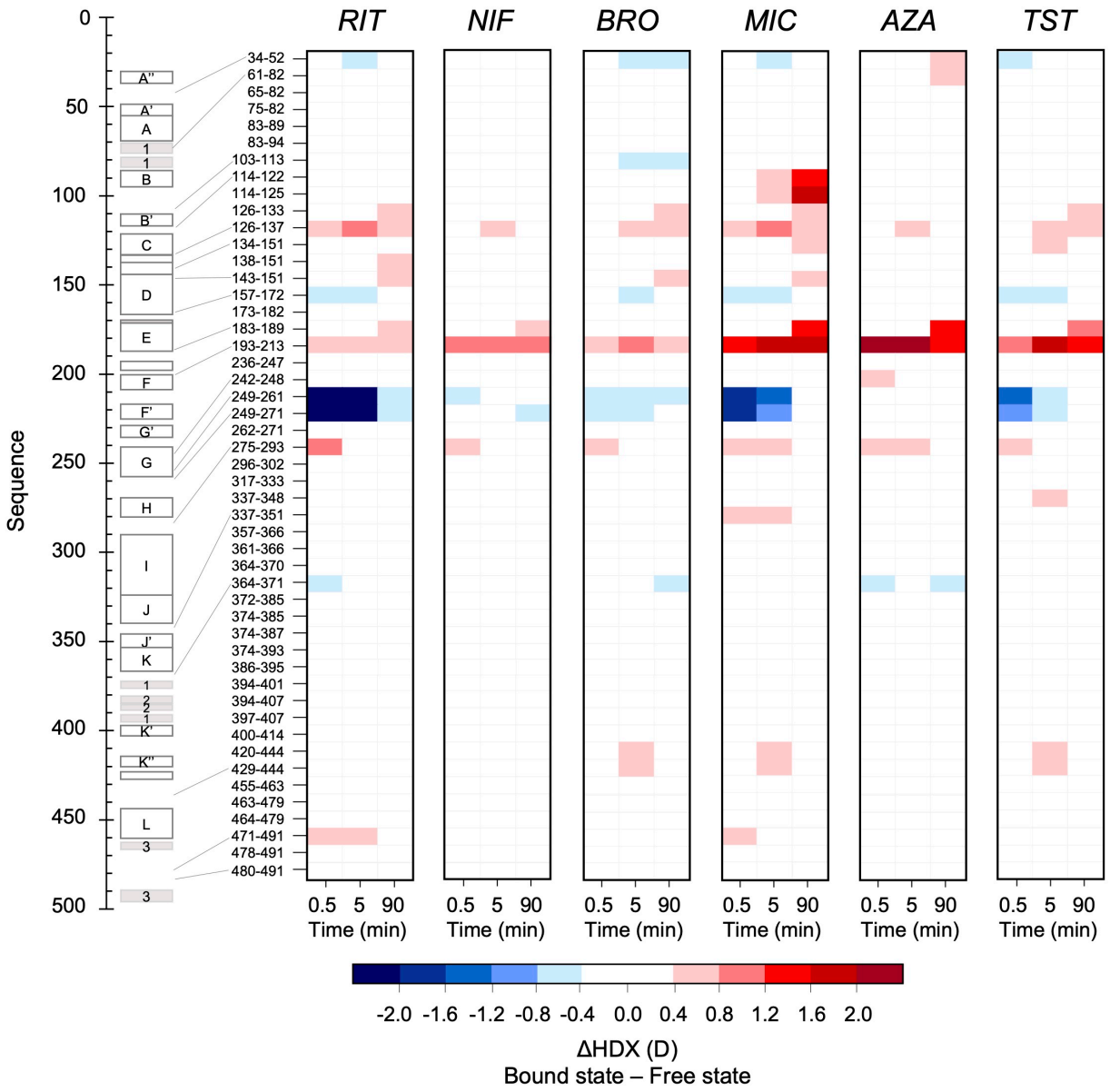

Figure 2.5.3. Chiclet plot of HDX differences between the bound and free states. Location of the peptides that display a significant difference in HDX is shown onto the primary CYP3A4 sequence on the left. The beta sheets are shaded gray.

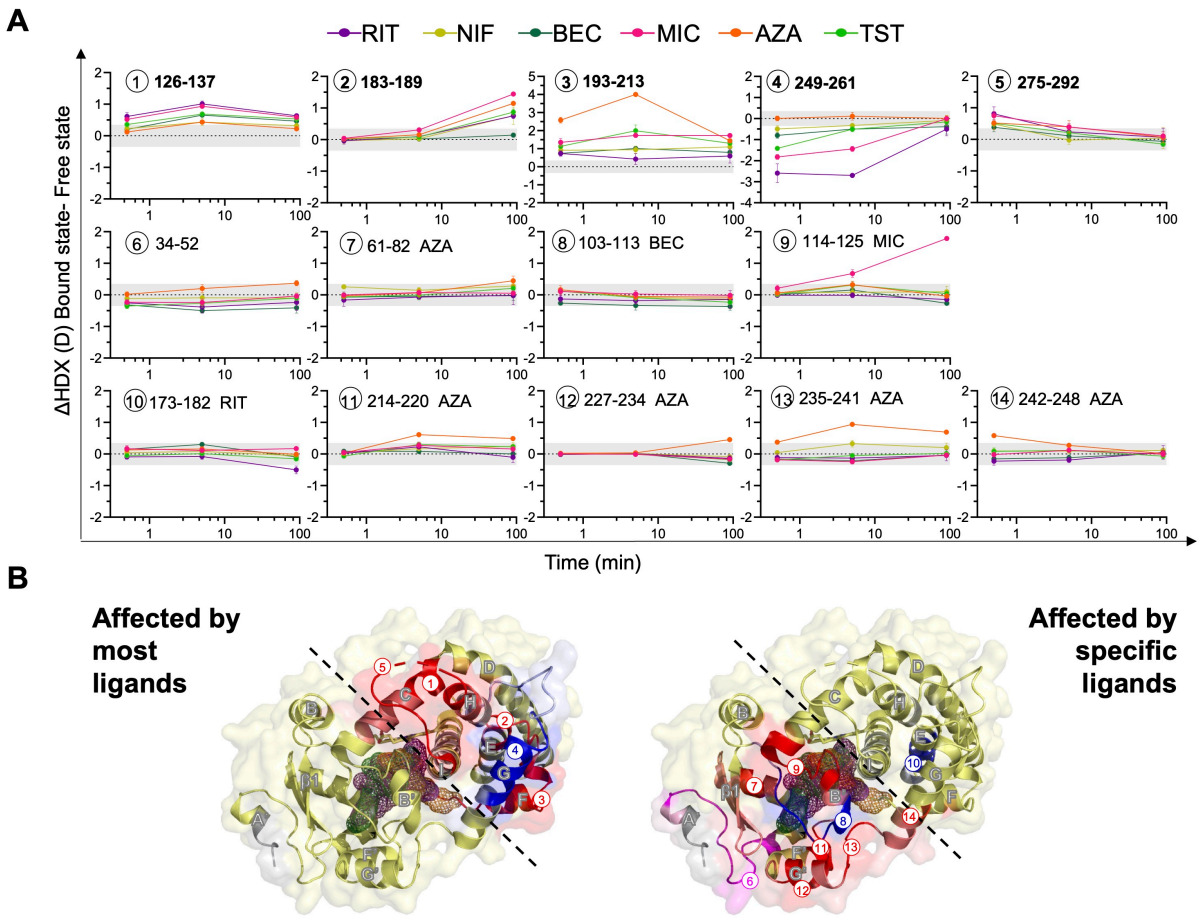

Figure 2.5.4. H/DX changes that are common to all ligands vs. H/DX changes that are ligand specific. A) ΔHDX plots of peptides affected with at least five ligands (in bold), or by one ligand only. B) Peptides in A mapped onto the crystal structure of CYP3A4 (PDB: 1TQN) represented as a pale-yellow surface and partially visible cartoon. BEC, RIT and AZA are represented as a mesh surface in the active site in dark green, purple, and orange, respectively. Uncovered regions are shaded gray. Deprotected peptides are shaded red. Protected peptides are shaded blue. Residues in the highlighted peptides that do not contribute to the observed ΔHDX are shaded lighter. Peptide 34-52 is in magenta as it is protected for some ligands and deprotected with others.

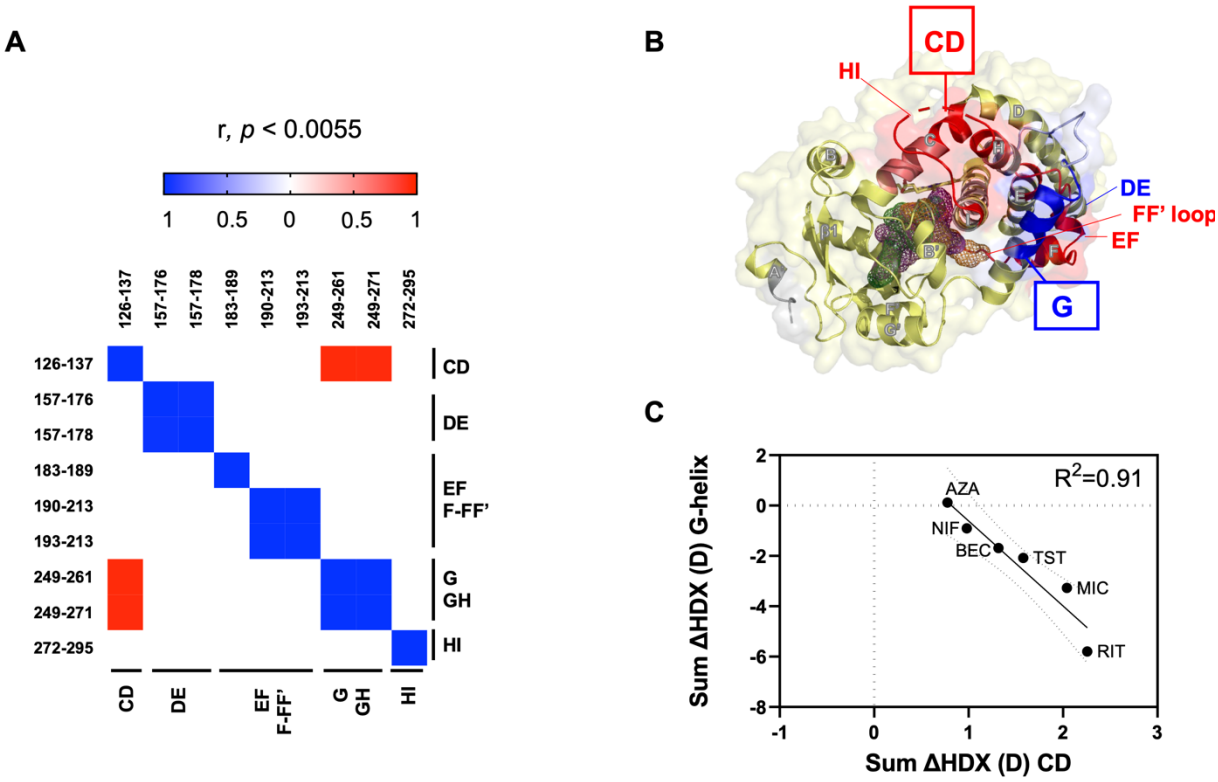

Figure 2.5.5. Dynamics of the G-helix are correlated to the C-D region. A) Correlation matrix heatmap of sum ΔHDX at 30 s, 5 m, and 90 m for peptides that show a significant difference in HDX for at least five ligands. B) Peptides in A mapped onto the 1TQN structure (yellow) in the same color representation as in Figure 2.5.4B. Only parts of the structure are visible for clarity. The C-D region and G-helix peptides are highlighted with boxes. C) Correlation plot of the sum ΔHDX of the CD region (peptide 126-137) against the sum ΔHDX of the G-helix (peptide 249-261). Dotted lines represent the 95% CI.

2.6 TABLES

Table 2.6.1. Properties of CYP3A4 ligands analyzed by HDX-MS. Affinity is reported as a K_d value or a K_s value when marked with a (*). Affinity measurements obtained with ND-embedded CYP3A4 are marked with (†).

Ligand	Type	Affinity (μM)	X-ray structure?	Binding to CYP3A4
Ritonavir (RIT)	II	0.85	Yes	Complex: binding is stoichiometric, irreversible and biphasic. [130], [205]
Nifedipine (NIF)	I	20*	No	Complex: multiple binder, displays substrate inhibition kinetics [206]
Bromocriptine (BEC)	I	0.45	Yes	Single binder [200], [207]
Miconazole (MIC)	II	0.45 *†	No	Single binder? [207]
Azamulin (AZA)	I	1.7*	Yes	Single binder [199]
Testosterone (TST)	I	120†	No	Complex: multiple binder, allosteric [165]

Table 2.6.2. Summary of HDX conditions and final analysis with 3A4-NDs in the free state and bound to RIT, NIF, or BEC.

Data Set	Free (I)	RIT	NIF	BEC
HDX reaction details	0.9 μM 3A4-ND, 50 mM HEPES, 50 mM NaCl, 2 mM TCEP, 2% DMSO, pH = 7.0, 24 °C	0.9 μM 3A4-ND, 50 mM HEPES, 50 mM NaCl, 2 mM TCEP, 20 μM RIT, 2% DMSO, pH = 7.0, 24 °C	0.9 μM 3A4-ND, 50 mM HEPES, 50 mM NaCl, 2 mM TCEP, 400 μM NIF, 2% DMSO, pH = 7.0, 24 °C	0.9 μM 3A4-ND, 50 mM HEPES, 50 mM NaCl, 2 mM TCEP, 20 μM BEC, 2% DMSO, pH = 7.0, 24 °C
Quench details	1.2% FA, 0.4 % TFA			
pH of quenched undeuterated sample	2.55			
Nanodisc disassembly, lipid removal details	1.05 μmol sodium cholate, 3 mg ZrO_2 resin per sample			
D_{frac}	0.832			
HDX time course (min)	0.5, 5, 90	0.5, 5, 90	0.5, 5, 90	0.5, 5, 90
# of Peptides	65			
Coverage	89.3% (sequence); 79.3% (amide hydrogens)			
Average peptide length / Redundancy	12.4/ 1.88			
Replicates (biological or technical)	2 (technical)	2 (technical)	2 (technical)	2 (technical)
Repeatability	0.09 D (average standard deviation)	0.13 D (average standard deviation)	0.11 D (average standard deviation)	0.05 (average standard deviation)
Significant differences in HDX (delta HDX > X D); [RIT/NIF/BEC-Free(I)]	NA	0.38 D (95% CI); 0.85 D (99% CI)	0.35 D (95% CI); 0.77 D (99% CI)	0.25 D (95% CI); 0.55 D (99% CI)

Table 2.6.3. Summary of HDX conditions and analysis with 3A4-NDs in the free state and bound to MIC, AZA, or TST.

Data Set	Free (II)	MIC	AZA	TST
HDX reaction details	1.2 μM 3A4-ND, 50 mM HEPES, 50 mM NaCl, 2 mM TCEP, 2% DMSO, pH = 7.0, 24 °C	1.2 μM 3A4-ND, 50 mM HEPES, 50 mM NaCl, 2 mM TCEP, 2% DMSO, pH = 7.0, 24 °C	1.2 μM 3A4-ND, 50 mM HEPES, 50 mM NaCl, 2 mM TCEP, 2% DMSO, pH = 7.0, 24 °C	1.2 μM 3A4-ND, 50 mM HEPES, 50 mM NaCl, 2 mM TCEP, 2% DMSO, pH = 7.0, 24 °C
Quench details	1.2% FA, 0.4 % TFA			
pH of quenched undeuterated sample	2.55			
Nanodisc disassembly, lipid removal details	1.05 μmol sodium cholate, 3 mg ZrO_2 resin per sample			
D_{frac}	0.832			
HDX time course (min)	0.5, 5, 90	0.5, 5, 90	0.5, 5, 90	0.5, 5, 90
# of Peptides	65			
Coverage	89.3% (sequence); 79.3% (amide hydrogens)			
Average peptide length / Redundancy	12.4/ 1.88			
Replicates (biological or technical)	2 (technical)	2 (technical)	2 (technical)	2 (technical)
Repeatability	0.042 D (average standard deviation)	0.05 D (average standard deviation)	0.08 D (average standard deviation)	0.08 D (average standard deviation)
Significant differences in HDX (delta HDX > X D); [MIC/AZA/TST-Free(II)]	NA	0.16 D (95% CI); 0.36 D (99% CI)	0.22 D (95% CI); 0.49 D (99% CI)	0.22 D (95% CI); 0.48 D (99% CI)

2.7 SUPPORTING FIGURES

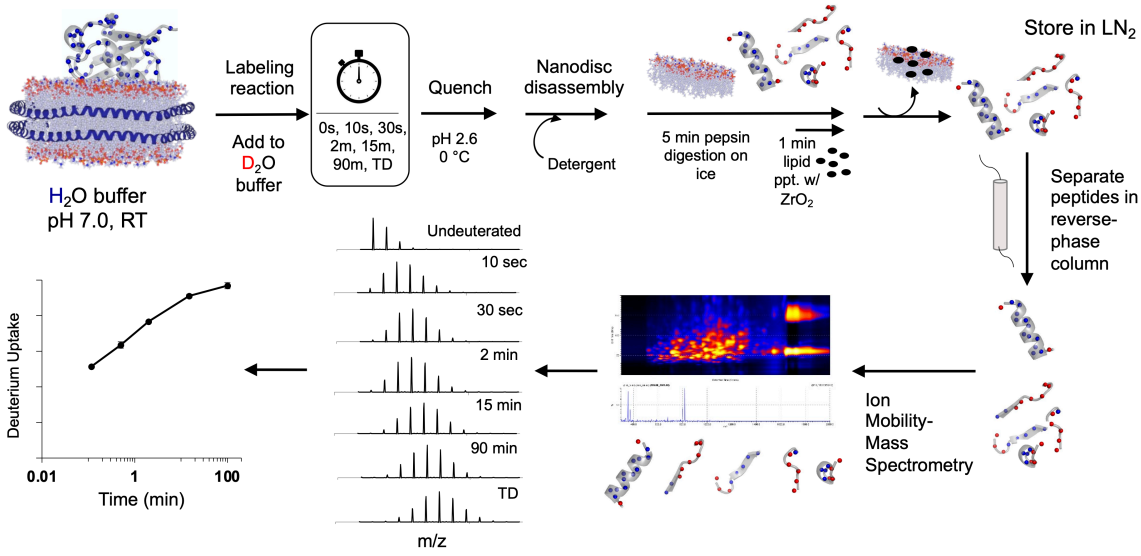

Supporting Figure 2.7.1. HDX workflow for nanodisc-embedded proteins.

Chapter 3. LIGAND-DEPENDENT STRUCTURAL DYNAMICS OF NANODISC-EMBEDDED CYP19A1

3.1 DYNAMICS AND MECHANISM OF ANDROSTENEDIONE BINDING TO MEMBRANE-ASSOCIATED AROMATASE

Note: Parts of this section are reproduced from the following publication: L. Paço, F. Zarate-Perez, A. F. Clouser, W. M. Atkins, and J. C. Hackett, "Dynamics and mechanism of androstenedione binding to membrane-associated aromatase", *Biochemistry*, 2020.
F. Zarate-Perez prepared and characterized the 19A1 nanodiscs. John C. Hackett performed the MD simulations.

3.1.1 Introduction

The cytochromes P450 (CYPs) are versatile catalysts responsible for a vast array of transformations in xenobiotic and endobiotic metabolism [60], [208], [209]. The range of chemical reactions catalyzed and the breadth of substrates transformed by CYPs are immense; however, the interplay of protein dynamics, ligand binding, and catalysis used to achieve this flexibility remains poorly understood. Within this void, there is very little known about how CYPs, especially those associated with the membrane, capture potential substrates. It is generally accepted that, due to their amphipathic nature, CYP substrates are harvested from the membrane. This paradigm is supported by rigorous molecular dynamics simulations of xenobiotic-metabolizing CYP3A4 [161] and CYP2D6 [210] with a limited number of model substrates. While simulations underscore the importance of the membrane interface and the structural elements involved in substrate ingress are readily apparent, direct experimental validation of these results is lacking. Furthermore, due to the

promiscuity of the enzymes examined to date, it is difficult to extrapolate the results to more selective CYPs, such as those involved in steroidogenesis. While selective, often the interactions that permit discrimination between structurally similar ligands are not obvious in the corresponding crystal structures. It is conceivable that selectivity is conferred through interactions made in metastable states during ligand transit; albeit their short lifetimes make experimental characterization extremely difficult.

Cytochrome P450 19A1 (19A1 hereafter), also known as aromatase, is a steroidogenic enzyme that catalyzes the terminal step in the biosynthesis of estrogens (estrone, 17β-estradiol) from androgens (androstenedione [ASD], testosterone) [211]–[214]. Accordingly, 19A1 has proven to be an invaluable target for pharmacotherapy used to treat estrogen-dependent breast and gynecological cancers as well as infertility [215]–[224]. Clinical relevance aside, phylogenetic analysis of the human CYPs reveal 19A1 to be among the most primordial [225]. 19A1's ancestral relationship to other human CYPs make its functional dynamics especially pertinent. In accordance with conformational dynamism [38], [226], the fundamental dynamics of primordial ancestors are conserved and serve as the foundation for evolution of new protein functions. Thus, the evolutionary origins of promiscuity in xenobiotic metabolizing CYPs are encoded in their evolutionary ancestors, including 19A1. This enzyme is therefore relevant to the extent that it promises insight into the mechanisms of substrate discrimination by steroidogenic CYPs, as well as illuminates the fundamental dynamics employed by the more recently evolved and promiscuous xenobiotic metabolizing CYPs.

Herein we describe the combination of hydrogen-deuterium exchange mass spectrometry (HDX-MS) and enhanced sampling molecular dynamics simulations of 19A1 in nanodiscs (19A1-

NDs) and a lipid bilayer, respectively, to investigate the mechanism of ASD binding and its impact on global structural dynamics. There are some differences in the membrane properties of NDs and periodic bilayers [227]; nevertheless, the similar membrane dimensions and the monodispersity of proteins embedded in NDs make them superior models for obtaining biophysical data for comparison to computer simulations. HDX-MS reports on the differential rates of exchange of amide protons for deuterons in deuterated solvent. Solvent-exposed and highly dynamic regions exchange rapidly, in contrast to those that are in structurally rigid domains (α-helices, β-sheets), buried, or inaccessible. These studies are complemented by Gaussian-accelerated molecular dynamics (GaMD) simulations, and a remarkable correlation between the HDX-MS and simulation is observed. Both approaches support global suppression of 19A1 backbone motion by ASD. Furthermore, the greatest protection from HDX was observed near the membrane interface including structural elements contacting ASD as it traverses its predicted entrance channel. Finally, the differential HDX supports that ASD eliminates detection of bimodal patterns, favoring binding to one state and thereby supporting the possibility that conformational selection is operative in 19A1. This result agrees with stopped-flow data supporting the presence of conformational selection in ligand binding to 19A1 [228].

3.1.2 Methods

Protein expression, purification, and ND assembly

19A1 used in these studies was identical to the form originally described by Kagawa and coworkers with arginine at position 264 [229]. 19A1-NDs were assembled from 19A1, the membrane scaffold protein MSP1D1(-), and POPC as previously described [228]. 19A1-NDs intended for HDX-MS were spiked with 10% glycerol following size exclusion chromatography and flash frozen in liquid N_2 for overnight shipping to the Atkins laboratory.

Hydrogen-deuterium exchange (HDX)

HDX was performed as previously described [102], [230] with modifications. A 10x 19A1-ND stock was buffer-exchanged into HDX buffer (50 mM HEPES, 50 mM NaCl, 2 mM TCEP, pH 7.0) and treated with either ASD or co-solvent (EtOH). A 10 µl ligand-free or ASD-bound 19A1-ND aliquot was incubated in the dark for at least 10 min at 24°C prior to dilution into 90 µl of D_2O HDX buffer containing ASD or the co-solvent for 10 s, 30 s, 2 m, 15 m, 90 m and 20 h. The final concentration in the 100 µl sample was ~1.3 µM 19A1-ND, 40 µM ASD, 83% D_2O and 1% (v/v) EtOH. HDX was quenched with an equal volume of ice-cold 1.2% formic acid / 0.4% trifluoroacetic acid quench solution for a final pH of ~2.6. Immediately preceding an exchange reaction, excess liquid (60 µl) was removed by centrifugation from 200 µl immobilized pepsin slurry and the pepsin beads were subsequently washed with 600 µl of 0.8% formic acid. ND disassembly was initiated with addition of 4.2 µl of 250 mM sodium cholate stock, followed by transfer into ~140 µl of pre-washed immobilized pepsin for 5 min of proteolytic digestion with rapid vortexing every 30 s. At min 4 of pepsin digestion, ZrO_2 (10 µl of 300 mg/ml ZrO_2-coated silica resin beads) was added to facilitate POPC lipid removal. Upon removal, 200 µl filtered aliquots were flash frozen in LN_2 and stored in -80°C until MS analysis.

Samples were prepared in triplicate in random order. One and two replicates were obtained for the 20-hour timepoint in the free and ASD-bound states respectively, prompting this time point to be excluded from the analysis. (An HDX difference plot including the 20-hour dataset can be found in the Supplemental Information, Figure 3.1.6.3). Undeuterated samples were prepared by using H_2O instead of D_2O buffer. Fully deuterated samples were prepared to calculate back-exchange of the deuterium label as follows: C18-separated peptides from two undeuterated

samples initially injected onto the mobile LC system were collected prior to MS analysis, dried under speed vacuum, resuspended in 100 µl of D_2O buffer, and incubated at 65 °C for 1 h. After that, the exchange procedure (quenching, digestion, etc.) was repeated as described above for the other samples. A control 10 s sample was prepared to ensure that the protein was stable for the duration of the experiment as follows: 10 µl of ligand-free 19A1-ND + 1% (v/v) EtOH was incubated at 24°C for at least 20 h. The next day, the sample was mixed with D_2O HDX buffer for 10 s and prepared as usual. The deuterium uptake profile of this sample was then compared to that of the other "10 s" ligand-free samples.

Mass spectrometry and HDX data analysis

MS was performed as previously described [230] with the following modifications: Thawed samples were injected into a mobile in-house LC system connected to a Waters Synapt-G2 MS instrument. The LC system was maintained at 1 °C to minimize back-exchange of the deuterium label. After being loaded onto the Waters BEH trap column for 5 m, peptides were resolved on the analytical C18 column using a gradient of 2 to 50% solvent B [0.1% FA in acetonitrile (ACN)] at 40 µL/min for 10 min. Following gradient separation of peptides on the C18 analytical column, the trap column was washed with a series of 250 µL injections: 1) 10 % FA; 2) 30 % trifluoroethanol; 3) 80 % MeOH; 4) 66 % isopropanol, 34 % ACN; 5) 80 % ACN. During the trap column washes, the analytical column was cleaned with three rapid gradient steps (0-95% solvent B, 30 s each) to minimize peptide carry-over between injections. A Thermo Orbitrap LTQ instrument was used to identify peptides via MS/MS mapping against a library of CYP19A1 and MSP1D1 protein sequences using the Batch-Tag Web tool in ProteinProspector [102], [231]. Peptide retention and drift times were collected via DriftScope 2.0. HXExpress3v2 [232] was used

to generate the isotopic distribution envelopes, relative deuterium uptake values from binomial fitting of mass envelopes, and bimodal deconvolution (when present).

Deuterium uptake values reported here were corrected for back-exchange of deuterium using the undeuterated and fully deuterated samples as previously described [168]. A threshold of statistical significance for differences in HDX between the two states was calculated in the form of a 95% confidence interval (CI) based on the average standard deviation of the pooled data [168], [185]. Peptides were considered protected if the decrease in HDX between the ASD-bound and free state was greater than the 95% confidence value for two consecutive time points. The 20 h time point was considered for this rule for peptides in the A' helix and B-C region, since it is clear that large differences in HDX occur in these regions beyond 90 m.

System Preparation and conventional MD

To maintain consistency with the experiments, an identical 19A1 sequence was used in the simulations. Following removal of crystallographic water from the 3EQM crystal structure [136], the first pair of residues resolved in the crystal structure (Ser45 and Ser46) were replaced with the sequence MARQSFGRGKL. Protonation states of amino acids were assigned using Poisson-Boltzmann based PropKa calculations at pH 7.4 [233]. Curated 19A1's initial position in the membrane was predicted using the Orientations of Proteins in Membranes (OPM) database [234]. Reoriented 19A1 was merged with 100 Å × 100 Å POPC membrane constructed using the Membrane Builder plugin VMD [55], with POPC and water within 0.8 Å of the protein removed. Membrane-associated 19A1 was solvated with an additional 10 Å layer of TIP3P water in the $\pm z$ directions. Potassium and chloride ions were added to an ionic strength of 0.15 M with the latter ion in slight excess to ensure electrical neutrality.

All molecular dynamics procedures were performed with the NAMD 2.13 code using the CHARMM36 force field for POPC and the CHARMM27 force field for the remainder of the system. Simulations were performed with and without ASD present in the active site using parameters from our previous work [235]. The complete systems were minimized for 10^4 steps followed by equilibration of the lipid tails for 1 ns with the coordinates of the remaining atoms frozen. Melting of the lipid tails around the protein was followed by 2 ns at constant temperature and pressure (NPT) simulation with a harmonic restraint (5 kcal mol^{-1} $Å^{-2}$) applied to the protein C_α atoms using the Langevin piston method with a target pressure of 1.01325 bar, decay period of 50 fs, and piston temperature of 300 K. After completion of the preparative simulations, the complete 19A1 systems were equilibrated in the NPT ensemble for an additional 2 ns.

Gaussian-Accelerated Molecular Dynamics

A pair (±ASD) of 104 ns preparatory GaMD simulations were performed where potential statistics (V_{max}, V_{min}, V_{avg}, and σ_V) collected in the latter 100 ns were used to calculate the boost potential (48, 49). Their endpoints were used to spawn four each 0.75 μs GaMD simulations with independently-randomized velocities at 300 K. GaMD simulations were performed in "dual-boost" mode meaning that boost potentials were added to both the dihedral and total system potential energies by setting the reference energy to lower bound, $E=V_{max}$. The average and standard deviation of the potential energy was calculated every 200 ps. The upper limit for the dihedral and total boost potential energies was set to 6 kcal mol^{-1} ($\sim 10k_BT$). Trajectory frames were saved every 200 ps for further analysis. Only the latter 0.4 μs of each trajectory were subject to subsequent analyses.

Random Acceleration MD

Five RAMD simulations were performed from the endpoints of each of the four GaMD simulations. A force of 14 kcal mol^{-1} Å was applied to the ASD center of mass. The orientation of the random force was re-assigned if the ASD center of mass did not travel 0.025 Å every 100 steps. RAMD simulations were terminated if ASD traveled 30 Å from its initial position or if the simulation time reached 1 ns.

Adaptive Biasing Force Simulations

The vector defined by the ASD center of mass when it is present in the active site and in the membrane was used to define the reaction coordinate for ASD access to the 19A1 active site [236]. The reaction coordinate was divided into 2 Å bins and a RAMD trajectory snapshot with the ligand subsiding in each bins were selected as initial positions. These frames were minimized for 2000 steps and equilibrated for 2 ns in the NVT ensemble with the ASD coordinates frozen. The ABF data were accrued in bins 0.1 Å wide with upper and lower wall constants of 100 kcal mol^{-1} $Å^{-2}$. Simulations were performed until the overall PMF was observed to converge, defined as a mean PMF difference of less than 0.3 kcal mol^{-1}. To avoid translation of 19A1 in the membrane during ABF calculations, the C_α atoms of Thr170, Val194, and Leu284 were harmonically restrained with a force constant of 600 kcal mol^{-1} $Å^{-2}$. No bias was applied during the first 10^4 steps of the ABF simulations to avoid perturbation by non-equilibrium effects.

3.1.3 Results

Global dynamics of aromatase

Dynamics of ligand-free and ASD-bound 19A1-NDs were probed via HDX-MS as previously described for drug-metabolizing CYP3A4 with modifications [139], [237]. Fully deuterated uptake

profiles were obtained for each peptide and absolute deuterium uptake values were corrected for back-exchange of the deuterium label during the experiment. Analysis of 61 peptides resulted in 69.2% coverage of the 19A1 sequence. Regions with no peptide coverage consisted of the G-H and D-E loops, parts of the D, G, and I-helices, most of the H and L-helices and the β9-β10 sheets. Deuterium uptake levels at representative time points are summarized in Figure 3.1.6.4. The labeling reaction proceeded to >95% for rapidly exchanging peptides, whereas rigid or buried regions such as parts of the K helix, had near zero HDX at 90 m of the deuterium labeling reaction. In lieu of a ligand-free structure, the results provide novel structural information about ligand-free 19A1 under native-like conditions.

Comparison of HDX profiles of ligand-free and ASD-bound 19A1

In our recent study, we showed that binding of ASD to 19A1-NDs conforms to a single-site model with a K_d of 0.14 μM [228]. Herein, we show that the presence of ASD suppresses HDX (and therefore conformational dynamics) of 19A1. Protection from HDX in the ASD-bound state is not localized to the active site, but rather distributed throughout the protein, including the protein-membrane interface and substrate access channel. Notably, all the membrane-associated regions are protected from HDX in the presence of ASD. No significant deprotection was observed. The 16 peptides in Figure 3.1.5.1 showed significant differences in deuterium uptake between the two states, except for the B'-C loop (Figure 3.1.5.1, peptide 4). There was no difference in HDX for this peptide up to 90 m, but a dramatic decrease in HDX was observed at 20 h (Figure 3.1.6.3), indicating slow changes in the conformational dynamics of the B'-C loop that are not captured by the 10 s - 90 m deuterium labeling window. Similarly, the protection was exacerbated at 20 h for the A' helix (Figure 3.1.6.3).

Protected regions consisted of the membrane-associated A'- and A-helices (Figure 3.1.5.1; 1-2), the B-C (3-5) and F-G (7-10) blocks, the K-β3 region in the active site (11-12), the K', K''-helices and intervening loops (13-14), and the C-term region containing residues in the active site and near the membrane interface (15-16). Protected peptide 372-380 (12) contains residues Leu372 and Val373 that make direct ligand contact, and Met374, the backbone amide of which is the proposed hydrogen bond donor to the 17-keto oxygen of ASD in the crystal structures [136], [238]. The peptide containing Asp309, the hydrogen bond donor to the 3-keto oxygen of ASD, displayed minimal differences in HDX (< 5%) between the free and ASD-bound states (Figure 3.1.6.5).

The differences in absolute deuterium uptake for all the peptides are summarized in Figure 3.1.5.2. It is worth noting that two highly protected regions containing part of the A-helix and the β7-β9 fragment (Figure 3.1.5.1, peptides 2 and 16), are located next to each other in three-dimensional space and display a similar trend in uptake kinetics with most of the protection from HDX occurring early in the labeling reaction. This is unlike the rest of the protein where protection from HDX typically increases in the later time points.

Bimodal patterns of the B'-C Region in Ligand-Free 19A1

We observed bimodal patterns in the mass spectra of the B'-C loop (peptide 125-140) across all time points for ligand-free 19A1 only (Figure 3.1.5.3), indicating at least two distinct conformations in the absence of ASD. The population ensemble consisted of a major, slowly exchanging state and a minor, rapidly exchanging state. The relative abundance of each state remained nearly constant up to 90 m where the abundance of the minor, exposed state increased from 10% to 30%. This exchange profile was observed across replicates (data not shown) and the bimodal deconvolution of the spectra was consistent among replicates. The increase in relative abundance of the exposed state at the latest time point suggests an EX1 [239] component of the

exchange kinetics where multiple residues in the loop undergo a correlated opening motion to convert from the slowly exchanging state to the more rapidly exchanging state. As each population becomes increasingly deuterated with time, the data is best described by a mixed EX2/EX1 exchange model, also referred to as EXX kinetics [240], though more evidence is required to confirm this mechanism. The slow transition to the exposed state is not fully captured in the 10 s – 90 m time course. Importantly, protein integrity issues were excluded as contributors to the increase in relative abundance of the exposed state. The mass spectra of the B'-C loop peptide corresponding to a "10 s control" sample, where ligand-free 19A1 was left at 24°C for a day and subsequently exchanged in deuterated buffer for 10 s, displayed similar bimodal patterns and relative abundance of states (data not shown) as the regular "10 s" samples. In the ASD-bound dataset, the B'-C loop displayed unimodal isotopic distributions across all time points, resembling the major, slowly exchanging state in the ligand-free dataset, suggesting that ASD locks the protein in the more slowly exchanging conformation.

Gaussian-Accelerated Molecular Dynamics

The initial configuration for the 19A1 membrane system was generated by appending the N-terminus derived from CYP2C11 to the structure of human placental aromatase (PDB 3EQM) so that it matches the form of the enzyme in the 19A1-NDs [136], [229]. The modified structure was oriented relative to the POPC membrane slab in accordance with that predicted by the Orientations of Proteins in Membranes Database [234]. Following preparatory simulations, systems with and without ASD were subject to 100 ns of conventional MD to equilibrate the systems and gather the necessary statistics to calculate GaMD boost potentials. GaMD was selected because it achieves more extensive conformational sampling by lowering energetic barriers [241]. Like conventional aMD, it is also expected to enhance diffusion of lipids and thereby achieve a more rapid and

complete association of the 19A1 catalytic domain with the membrane [242]. From the endpoint of the conventional MD simulations, four each (± ASD) independent 0.75 μs GaMD simulations were performed. A representative endpoint from one of the ligand-free simulations is depicted in Figure 3.1.5.4 illustrating the membrane contacts as the truncated N-terminus, A'-helix, G'-helix, and the N-terminal region of the G-helix. Positions of the N-terminus, A'-helix, and G-helix relative to the bulk membrane layers are illustrated in Figure 3.1.5.5A-C. In each simulation, the position of the 19A1 catalytic domain was ensconced in the membrane and demonstrated stable fluctuations after approximately 0.4 μs. The truncated CYP2C11 N-terminus is too short to penetrate the bulk of the membrane and therefore mostly resides between the choline and phosphate units of the lipid bilayer, occasionally, albeit rarely, sampling interactions with the acylglycerols. On average, the A'-helix resides closer to the membrane surface between the choline and acylglycerol units of POPC. The G'-helix penetrates deeper, persisting at the level between the lipid phosphates and acylglycerols with occasional penetration into the hydrophobic tails. Association and penetration of the 19A1 catalytic domain in simulations with ASD present in the active site were qualitatively similar (data not shown).

The impact of bound ASD on the protein backbone fluctuations is illustrated in Figure 3.1.5.5D. Except for a few solvent-exposed regions distant from the ASD binding site and membrane interface (C-D, D-E, and K'' helices as well as β3-5 sheet), ASD suppresses dynamics throughout the protein, most notably in the N-terminus, A'-B, F-G, and β8-10 regions.

Random-Acceleration Molecular Dynamics

RAMD simulations were used to identify probable paths of ASD ingress/egress from the active site. It is achieved by applying a randomly oriented acceleration to the ligands center of mass. If the ligand does not travel a predefined distance from its origin in a specified number of steps, the

orientation of the acceleration is changed. This is repeated until the ligand escapes from the active site [243]–[245]. Twenty 2 ns RAMD simulations, five from each endpoint of four GaMD trajectories were performed. Expulsion of ASD from the active site was observed in eight of the RAMD simulations across three of the four trajectory endpoints. The egress pathways are depicted in Figure 3.1.5.6A. Seven are very similar, with ASD passing between the β3/4 sheet, N-terminus of the F-helix, B'-B loop, and the β8/9 turn. ASD exits from the groove formed by the A'- and G'-helices into the lipid headgroups. In two of the RAMD simulations, ASD persisted in a cavity formed by the A'-helix and the β1-4 sheet, but ultimately changed course to utilize the same exit point as in the other trajectories. In one simulation, ASD found an alternative pathway into the membrane passing through a channel lined by the F-helix and β8/9. Owing to the correlation between the changes in HDX and ASD-protein contacts, we focused subsequent scrutiny on the former pathway with adaptive biasing force (ABF) calculations.

Adaptive Biasing Force (ABF) Simulations in the ASD Access Tunnel

RAMD provides an overview of the access pathway, however sampling is too sparse to prioritize interactions and extract well-converged free energies. The endpoints of the predominant pathway identified in the RAMD simulations were used to define a 26 Å long reaction coordinate (ξ) for evaluation of ASD binding to 19A1 by ABF. ξ was partitioned into 2 Å windows and each populated with a trajectory snapshot with ASD positioned in the window. Sampling was initially performed for 50 ns, followed by 10 ns increments thereafter. The potentials of mean force (PMF), constructed by concatenating the profiles from each window, are illustrated in Figure 3.1.5.6B. The PMF converged after 90 ns with an overall free energy change, $\Delta A(\xi)$ of -13.7 kcal mol^{-1}.

ASD traverses a rough energy landscape characterized by several small energy barriers as it moves from the lipid headgroups to the deep potential energy well corresponding to active site

occupation. (Figure 3.1.5.6B) Despite its rugged appearance, the landscape can be partitioned into distinct regions including 1) ASD immersed in the lipid headgroups (Figure 3.1.5.6B, position A), 2) capture by 19A1 (Figure 3.1.5.6B, position B→C), 3) occupation of a metastable bound states (Figure 3.1.5.6B, position C and E), 4) passage through gating residues (Figure 3.1.5.6B, position C→F), and 5) ASD occupation of the active site (Figure 3.1.5.6B, position F). Representative trajectory snapshots from each of these regions are illustrated in Figure 3.1.5.7. From complete immersion in the POPC headgroups (ξ = 24-26 Å; Figure 3.1.5.7A), ASD is initially captured by sliding into the groove formed by the A'-helix, β1/2, and the turn between the F- and G'-helices (ξ = 20-22 Å; Figure 3.1.5.7B). ASD subsequently climbs a 4.4 kcal mol^{-1} barrier to access a shallow minimum (ξ = 14-16 Å; Figure 3.1.5.7C) corresponding to occupation of a pocket defined below by the A'-helix, above by β1/2, and the turn linking the F- and G'-helices. This 'off-path' binding site was observed in two of the RAMD trajectories. A notable feature of this window is the central distortion of the A'-helix that pushes it deeper into the membrane. ASD then moves into a channel defined primarily by the B'-B and B-C loops and β8/9. (ξ = 8-17 Å; Figure 3.1.5.7D & E) The channel is gated, relying on reorientation of several residues to allow passage of ASD into the active site. The first energy barrier (4.4 kcal mol^{-1}; Figure 3.1.5.6B, position D) corresponds to side chain rearrangements of Met374, Phe116, Leu228, and Leu477; while the second (2 kcal mol^{-1}; Figure 3.1.5.6B, position E) is attributable to passage between Phe221 and Trp224. When in the active site, ASD is oriented in a catalytically competent orientation with the 19-methyl and steroid A ring oriented above the heme iron. ASD also makes hydrophobic contacts with Ile133, Phe221, Trp224, and Leu477, as observed in the crystal structures. In structures obtained with ASD, testosterone, and other androgens [136], [139], [238], a close contact between the 3-keto and Asp309 is apparent, supporting the presence of a hydrogen bond. Protonation of

Asp309 is also supported by biophysical experiments [237]. However, despite Asp309 being protonated in the simulations, no hydrogen bonding with Asp309 was visible, rather the 3-keto oxygen atom accepts a hydrogen bond from the side chain of Thr310.

3.1.4 Discussion

In this work, we combined differential HDX-MS with enhanced sampling and non-equilibrium MD simulations to interrogate how ASD binding impacts the dynamics of 19A1 in a native-like membrane environment and elucidate the mechanism by which ASD accesses the active site. HDX-MS has emerged as a powerful tool to understand protein dynamics. MD has the potential to be highly complementary because it informs, in atomistic detail, on the dynamics and solvation that determine HDX. Nevertheless, the marriage of the two methods is not perfect, as there still many challenges to be overcome and pitfalls to be avoided when interpreting the integrated results [246]. It is important to remember that HDX-MS does not directly report on conformational dynamics, but rather on the solvent accessibility, strength, and frequency of hydrogen bonding of the backbone amides [247]. Quantitative information about hydrogen bonding and solvent accessible surface area can be conveniently extracted from MD-generated ensembles. However, there are additional factors dictating the extent of HDX that remain poorly understood or difficult to track in a simulation, such as regional electrostatic potential [248]. These limitations have translated to shortfalls in previous attempts to completely reconcile HDX and MD in even small soluble proteins [246]. MD likewise has limitations. Most notably, even with the advancements made in computing hardware and development of enhanced sampling methods, MD is still generally unable to access and sufficiently sample rare conformational transitions occurring over a potentially hours long HDX experiment. In view of the caveats associated with integrating these

approaches, we observed remarkable correlation between the results of differential HDX-MS using 19A1-NDs and MD of 19A1 in a POPC bilayer. Both methods support near global suppression of 19A1 backbone dynamics in the presence of ASD. Furthermore, the greatest protection from HDX is in regions at the membrane interface, close to the predicted entrance channel, and in contact with ASD as it moves between the membrane and the active site.

These results are consistent with an earlier report of lower HDX in the α-helices and slower dynamics of the F-G motif as probed by FTIR and time-resolved fluorescence spectroscopy, respectively [93]. The ASD-dependent differences in HDX are striking, suggesting the bound and unbound states adopt distinct conformations in native-like conditions. Open (free) and closed (bound) conformations of 19A1 have been previously discussed [93]. Though the HDX results here can be interpreted in favor of the open/closed model, they do not provide conclusive proof. The bimodal patterns observed for the B'-C loop indicate that there are at least two populations of ligand-free 19A1.

Of note is the extreme attenuation of rapid exchange in the early time points for the β7-β9 fragment (Figure 3.1.5.1, peptide 16) when ASD is bound. From the crystal structures, Ser478 and His480 make direct contact with ASD and several other residues that line the access tunnel [136], [238]. ASD binding might promote hydrogen bonding of the backbone amides, stabilizing the fragment. Moreover, the region is characterized by relatively low thermal isotropic factors in high-resolution bound structures and normal mode analysis describes it to be relatively stationary in the bound state [141]. Formation of hydrogen bonds is sufficient to slow HDX though not necessary. Lack of access to the solvent catalyst could be another reason. Buried unbonded amides are rare in soluble globular proteins due to the energetic costs associated with these groups operating freely in hydrophobic cavities [247]. In the context of membrane proteins however, deeper insertion in

the membrane upon substrate binding could expel solvent from unbonded amide sites and lead to the sharp protection observed. Speculatively, the similar trend in uptake kinetics observed for the A'-A turn motif with most of the protection occurring early in the exchange reaction, and its proximity to the C-terminal β7-β9 loop (specifically, the β8-β9 loop) could be interpreted as the two peptides "experiencing" a similar environment, such as one deeper in the protein-lipid interface. MD results showed a deeper insertion of the A' and G' helix as ASD is traversing the access channel, suggesting that such distortions in the membrane can occur, albeit their precise location in the protein might shift from pre-equilibrium to equilibrium conditions. The A'- and G'-helices are also protected from exchange when ASD is bound. Regardless of the inner workings of the slow exchange in the bound state, the effect of ASD on the protein-lipid interface, particularly around the access channel, is remarkable.

In an interesting observation with unknown functional relevance, the K'-K'' loop and K''-helix were also protected from exchange in the presence of ASD but remain unaltered in the MD simulations. This region is located far from the active site, access channel, and membrane interface. The protection observed could be due to long-range allosteric interactions propagating from the binding pocket or in a region in the heme proximal cavity that is missing coverage.

The observation that regions contacting ASD as it traverses the access tunnel discovered by RAMD is very intriguing. It is tempting to attribute the observed protection from HDX to the frequent population of metastable states on the PMF; however, owing to the strong energetic preference for occupation of the active site, global suppression of dynamics will mostly be attributable to the latter configuration. The occupation of the corresponding access tunnel by steroid nuclei in the crystal structures of other CYP enzymes is not unprecedented and noteworthy. In CYP46A1, there is a ~25 Å banana-shaped cavity accommodating cholesterol 3-sulfate lined

by the same secondary structural elements predicted in this work [249]. Furthermore, HDX-MS of CYP46A1 ± cholesterol 3-sulfate likewise demonstrated suppression of exchange in many of the same regions suppressed by ASD in 19A1 [104]. Occupation of this channel by the intermediate substrates 22-hydroxycholesterol [250] and 20,22,-dihydroxycholesterol [251] were observed in CYP11A1. In contrast to 19A1, these channels are the terminal binding site for the steroid nuclei, serving to optimally position the C17 side chains above the heme iron for oxidation. Assuming that 19A1 is an evolutionary precursor to these enzymes, these similarities could be interpreted as repurposing of the access tunnel to modulate substrate selectivity.

In summary, these results support the sequestering of steroid substrates from the membrane and reiterate the important functional consequences of membrane integration in 19A1. The substrate-induced differences in HDX described here are markedly more extensive than those observed for xenobiotic-metabolizing CYP3A4 embedded in NDs [102], [230]. HDX of CYP3A4 is minimally perturbed in the presence of different ligands compared to 19A1. The degree to which HDX is affected by ligands raises an interesting premise in the context of specific vs. promiscuous enzymes-it appears that the backbone dynamics of the primordial and highly substrate-specific 19A1 is more sensitive to the presence of its native substrate. Whether this paradigm will survive as knowledge of CYP dynamics expands remains to determined. In view of the strong correlation observed in this work, we expect the combination of HDX-MS of CYP-NDs with MD simulations to continue to be an invaluable approach to test these hypotheses.

3.1.5 Figures

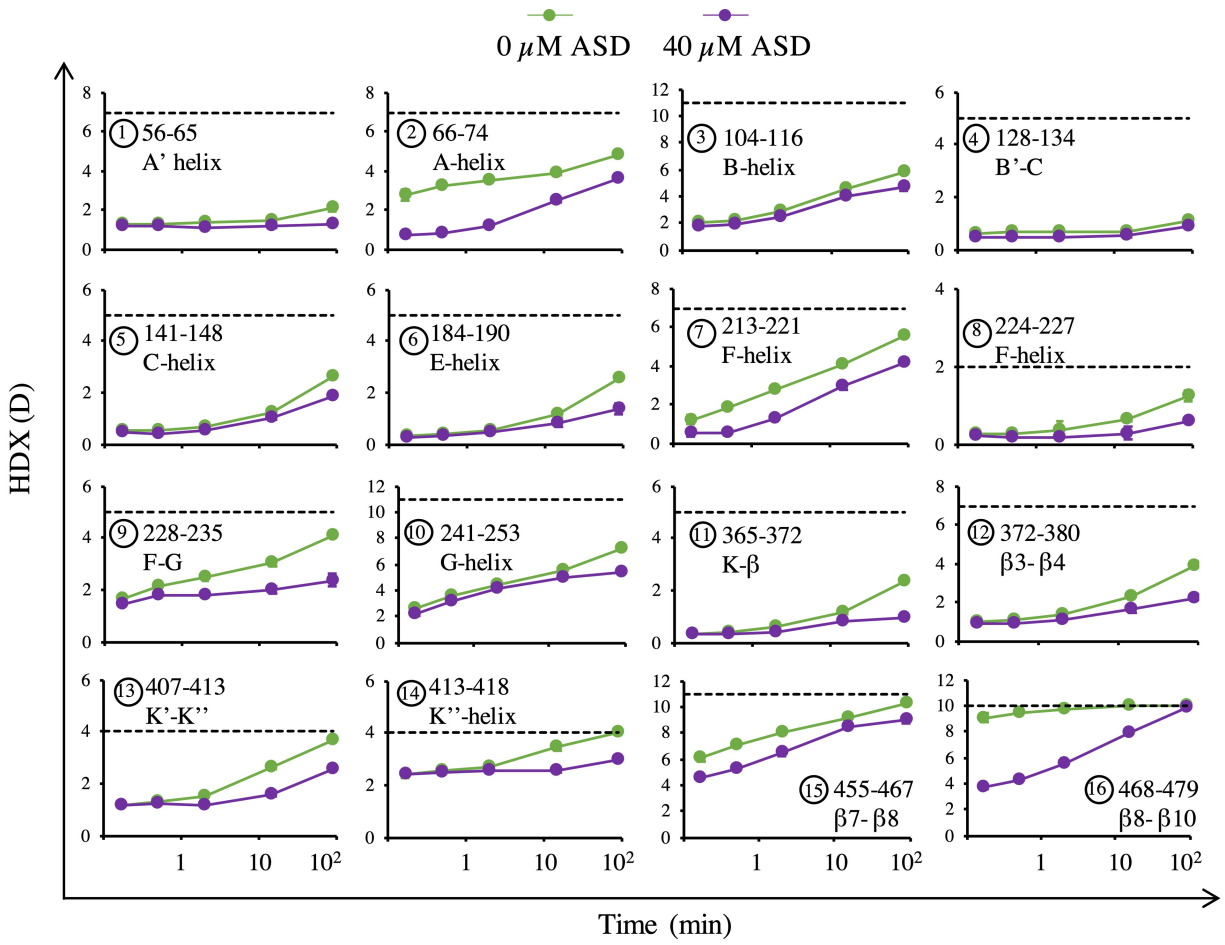

Figure 3.1.5.1 Effect of ASD on absolute deuterium uptake for selected peptides. (*n* = 3), 0 μM ASD (green), 40 μM ASD (purple). Dashed line represents the theoretical maximum number of exchangeable amides for each peptide. Error bars might be masked by marker size.

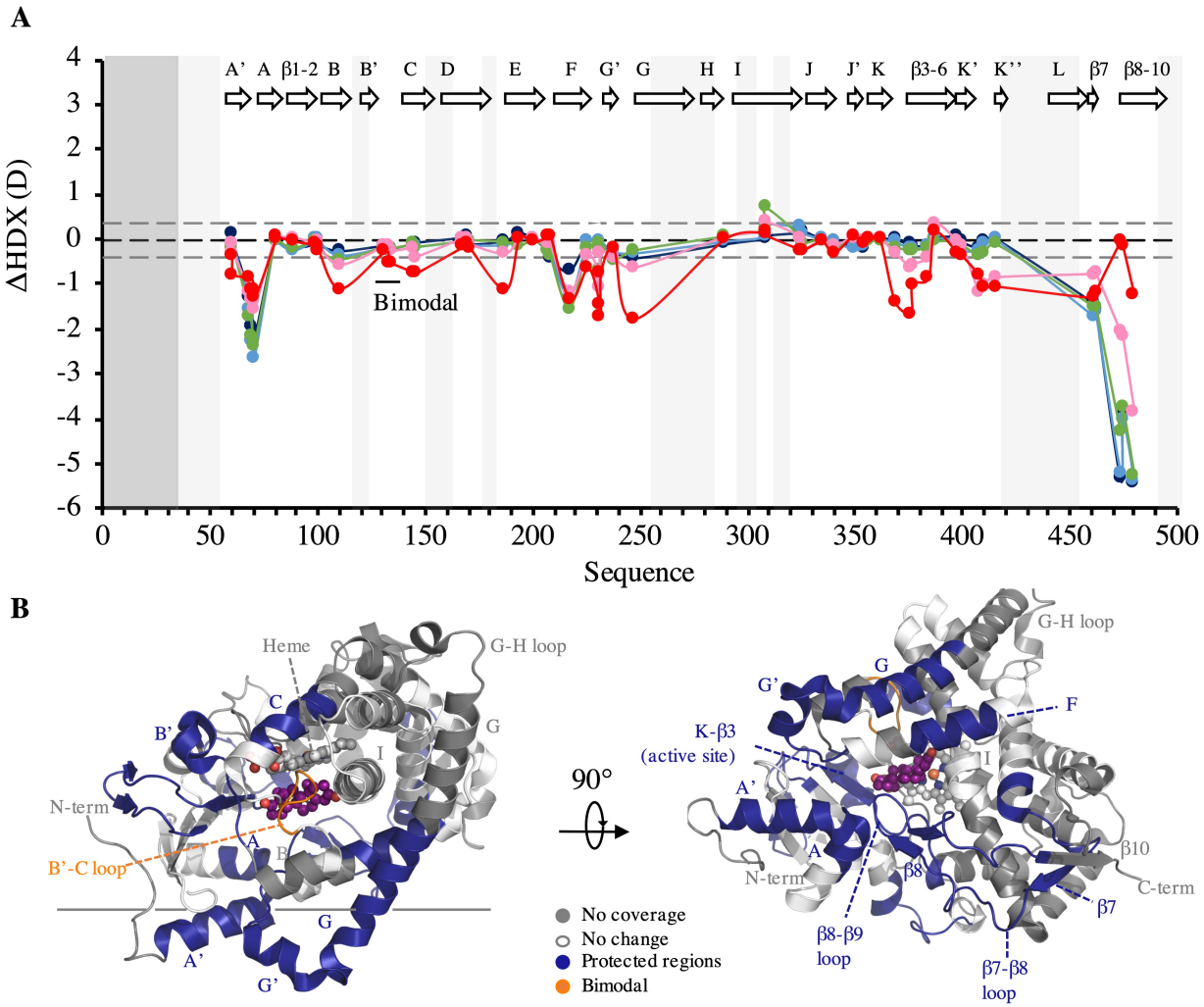

Figure 3.1.5.2. ASD-induced suppression of HDX in 19A1. **A.** Differences in HDX (ASD-bound state – free state) upon 10 s (dark blue), 30 s (light blue), 2 m (green), 15 m (pink) and 90 m (red) of deuteration. Peptides are represented by the midpoint of their sequence. The dashed gray lines at -0.38 D and +0.38 D represent the boundaries for a significant difference in uptake between the two states. Regions with no coverage are shaded gray. The first 35 residues (in dark gray) are not expressed. **B.** Heatmap of differences in HDX on the crystal structure of ASD-bound 19A1 (PDB ID: **3EQM**) in two orientations: membrane-bound (left) and flipped ~90° (right) for ease of viewing. Regions are considered protected if peptides show a significant decrease in uptake for two consecutive time-points. The heme and ASD are shown by sphere representation in gray and purple, respectively.

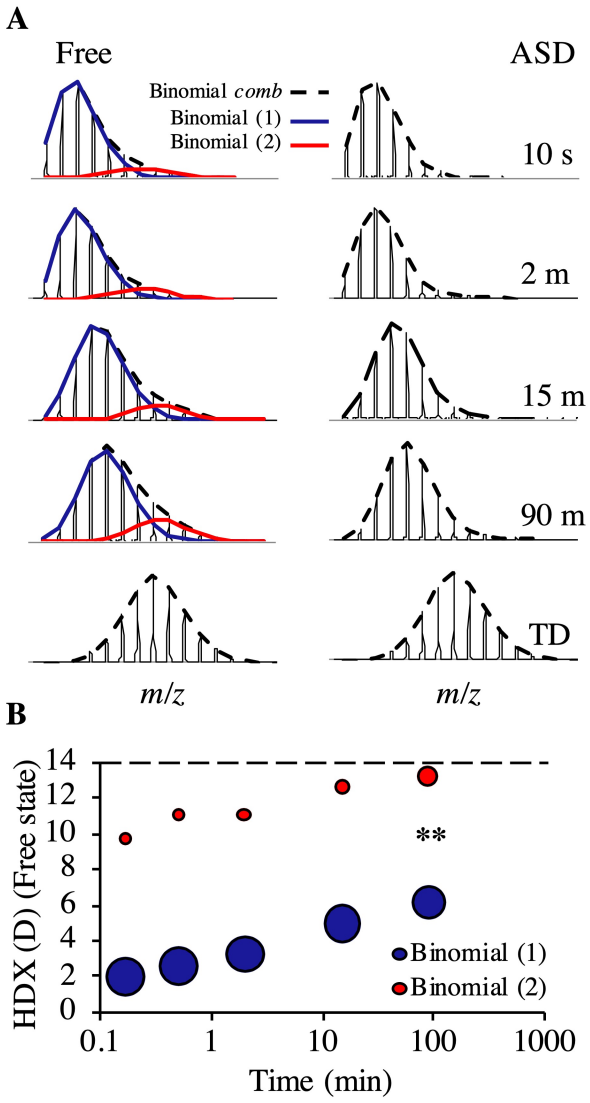

Figure 3.1.5.3. Bimodal patterns of the B'-C loop. **A.** Mass envelopes of peptide 125-140 in the ligand-free (left) and ASD-bound states (right) from variably labeled and totally deuterated (TD) samples. Solid lines indicate binomial fits from deconvolution of bimodal spectra. The ASD spectra did not pass statistical tests for bimodal deconvolution (HXExpress_3v22). **B**. Bubble plot showing HDX for the bimodal distribution of the 125-140 peptide in the free state. The relative size of the bubbles reflects the relative intensity of each species based on $n = 3$ replicates. Dashed line indicates the maximum number of amides that can exchange. (**) marks a significant difference (Student's t-test, $p < 0.01$) in the ratio of the species present at 90 m.

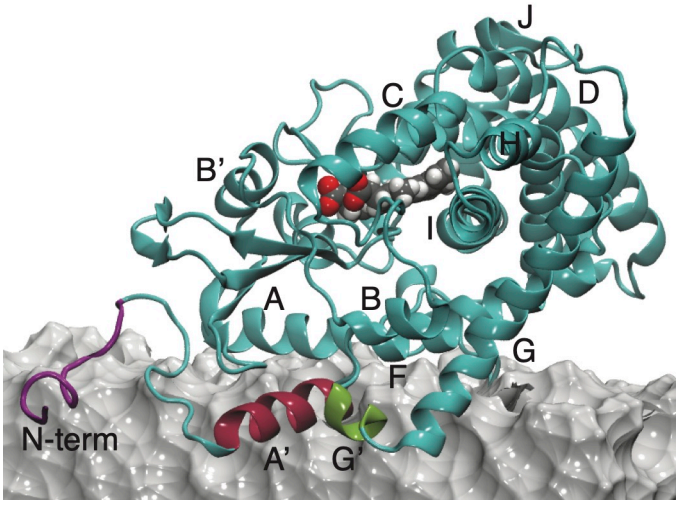

Figure 3.1.5.4. **Representative endpoint of one GaMD trajectory illustrating 19A1's orientation in the membrane**. The positions of the N-terminus, A'-, and G'-helices are in purple, red, and green, respectively. These colors match the corresponding data in Figure 3.1.5.5. The membrane bilayer, cut-away to reveal the protein, is depicted as a grey surface.

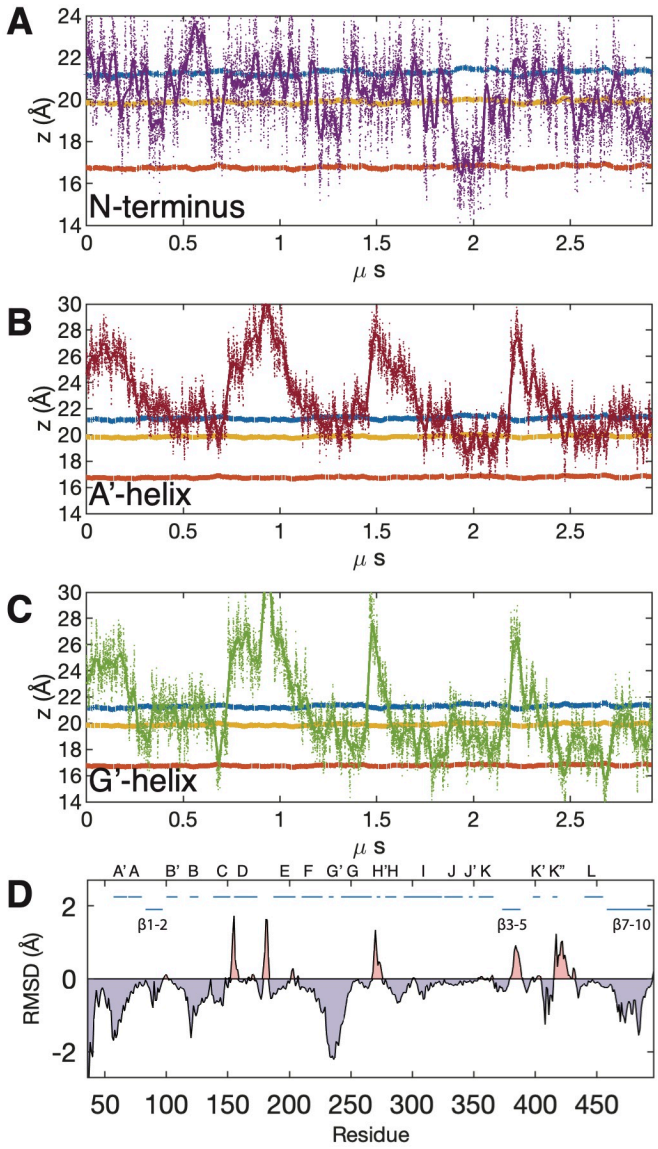

Figure 3.1.5.5. **Average distances above the membrane center for the N-terminus (A, purple), A'-helix (B, red), and G'-helix (C, green) in four concatenated 0.75 µs GaMD simulations in the absence of ASD.** Positions of the POPC choline, phosphates, and acylglycerols are depicted as blue, yellow, and orange lines, respectively. (**D**) Average per-residue RMSD values of 19A1 with ASD less the average values for the ligand free enzyme. RMSD values were calculated relative to the average structure over the entire trajectory. RMSD values were calculated using the CA, CB C, O, N, HA, HA1, HA2 and HN atoms.

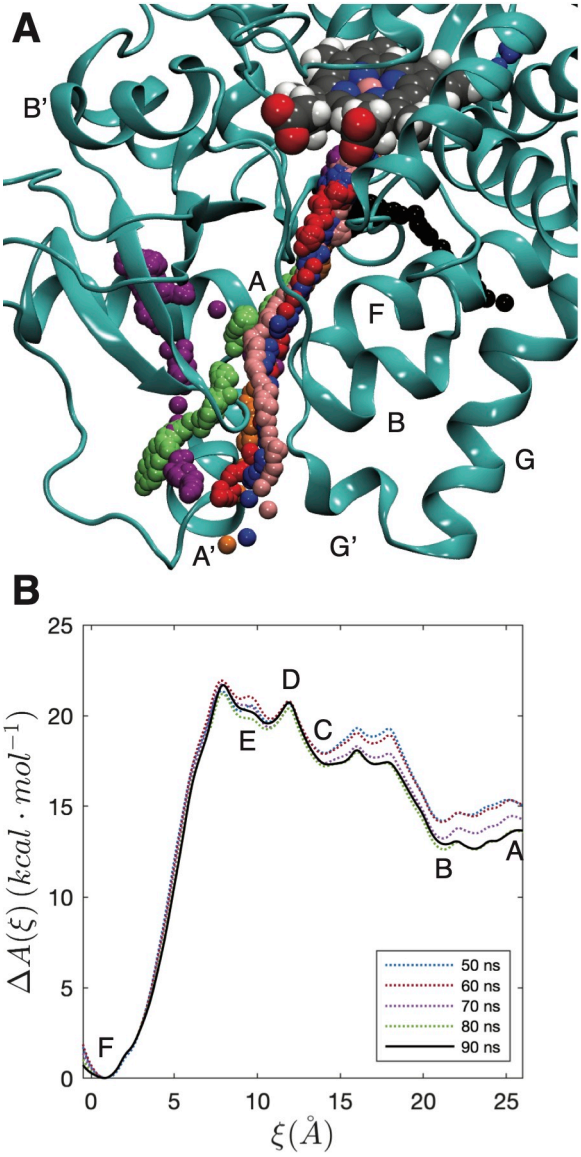

Figure 3.1.5.6. (**A) Pathways for ASD escape from eight RAMD simulations.** Positions of ASD's center of mass along each RAMD trajectory are depicted with differently colored spheres. Seven of the eight simulations revealed a common pathway where ASD exits in the enzyme from the groove formed by the A'-helix and the turn linking the F- and G-helices. In one instance (black spheres), ASD exited the active site through a channel bounded by the F-helix and β8/9 loop. (**B**) PMF along the reaction coordinate (ξ) for ASD traversing the entrance channel predicted by RAMD. Dashed lines denote stages of convergence for the PMF, starting from 50 ns (dotted lines) to 90 ns (solid black line) in 10-ns intervals. The landscape is characterized by regions corresponding to ASD in the lipid headgroups (A), capture by the A'-helix and the turn linking the F-G'helices (B) occupation of a metastable binding site (C), passage through gating residues (D,E), and occupation of the active site (F).

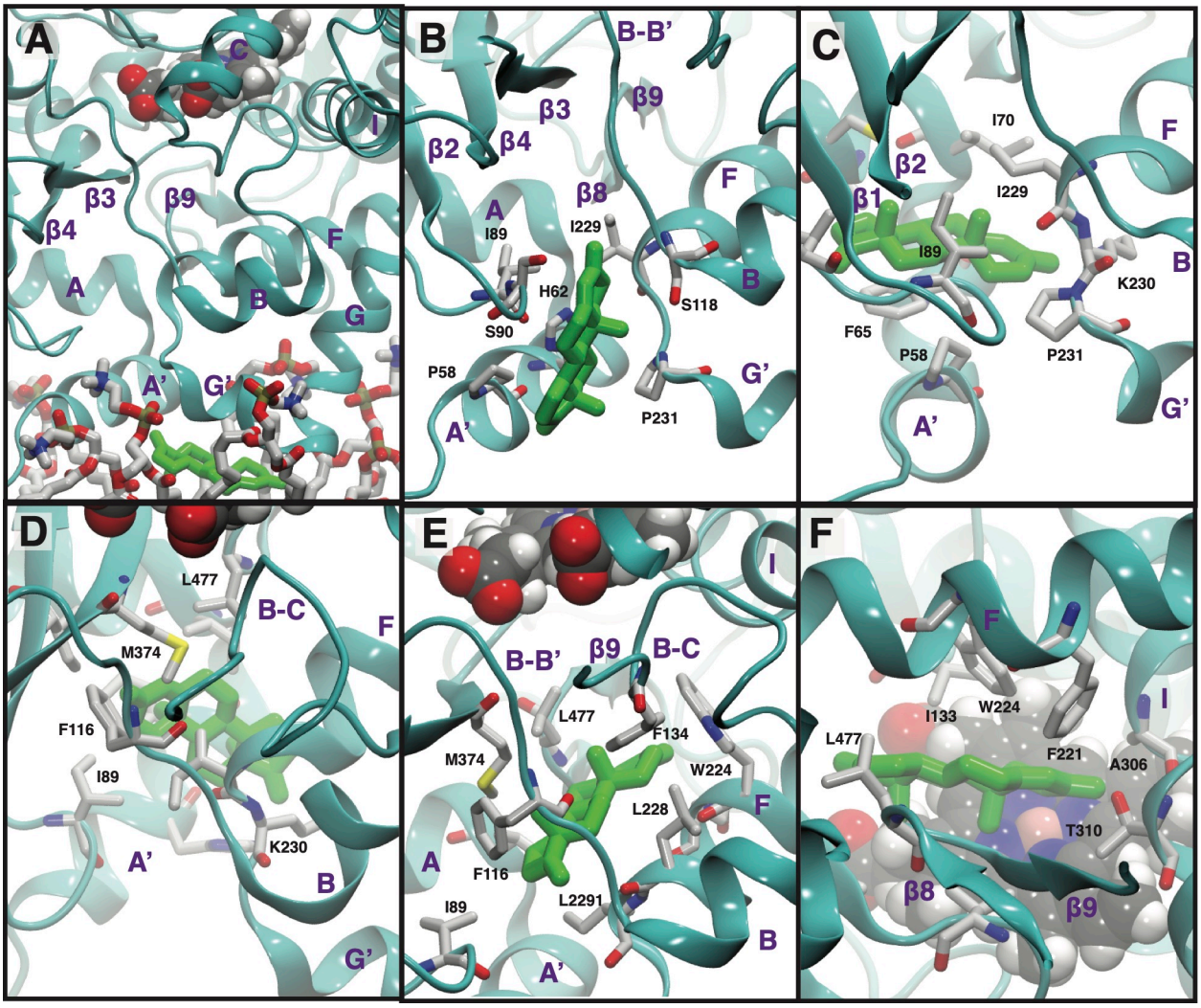

Figure 3.1.5.7. Representative snapshots depicting the position and interactions of ASD (green) in each of the regions labeled on the PMF in Figure 3.1.5.6B.

3.1.6 Supporting Figures

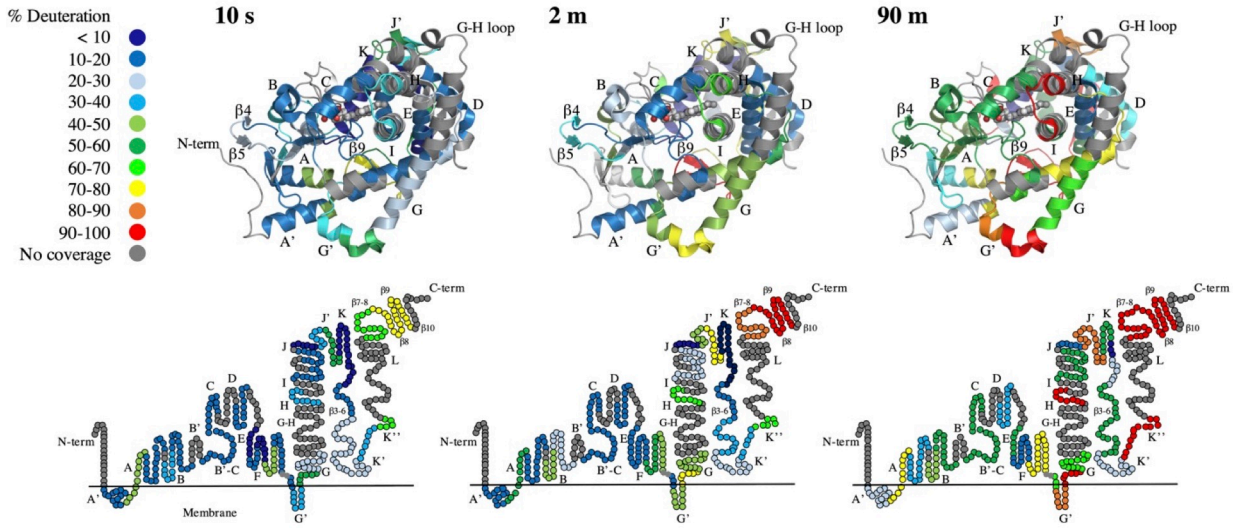

Figure 3.1.6.2. **Global dynamics of 19A1.** Heatmap of *percent* deuterium uptake for peptides at representative time points in the free state. Uptake levels are mapped on the crystal structure of 19A1 (PDB ID: **3EQM**) (top panel) and primary sequence (bottom panel, snake diagram). Circles under the solid line indicate regions immersed in the membrane.

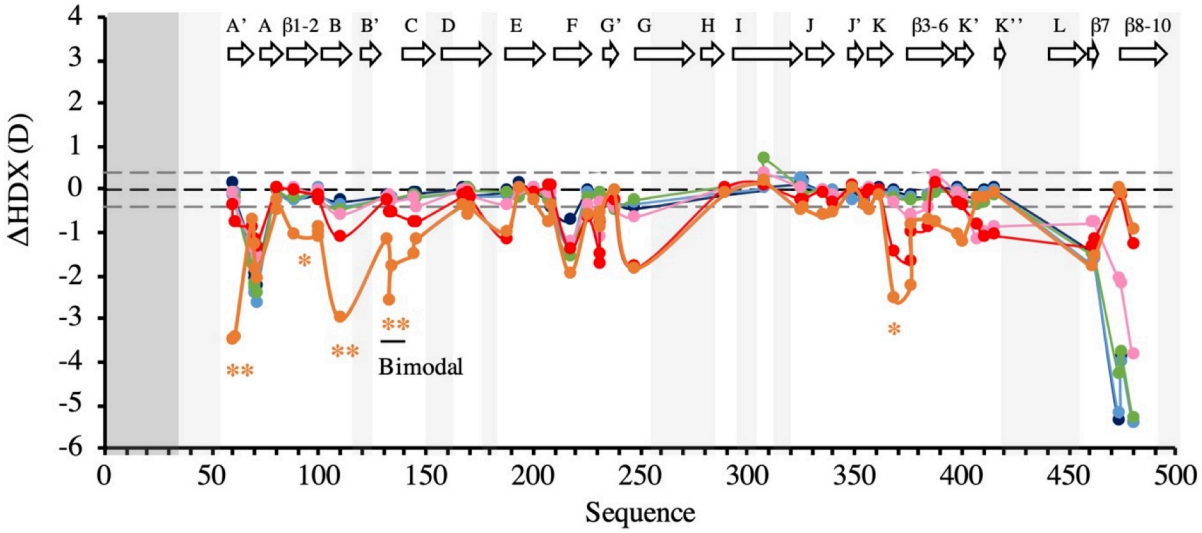

Figure 3.1.6.3. **ASD-induced suppression of HDX in 19A1 including the 20 hour dataset (orange). A.** Differences in HDX (ASD-bound state – free state) upon 10 s (dark blue), 30 s (light blue), 2 m (green), 15 m (pink), 90 m (red) and 20 hr (orange) of deuteration. (*) and (**) mark peptides in the 20 hr dataset that differ by more than 1 D and 2 D respectively from the nearest time point. Peptides are represented by the midpoint of their sequence. The dashed gray lines at -0.38 D and +0.38 D represent the boundaries for a significant difference in uptake between the two states. (95% CI based on the average standard deviation for all the peptides and timepoints). Regions with no coverage are shaded gray. The first 35 residues (in dark gray) are not expressed

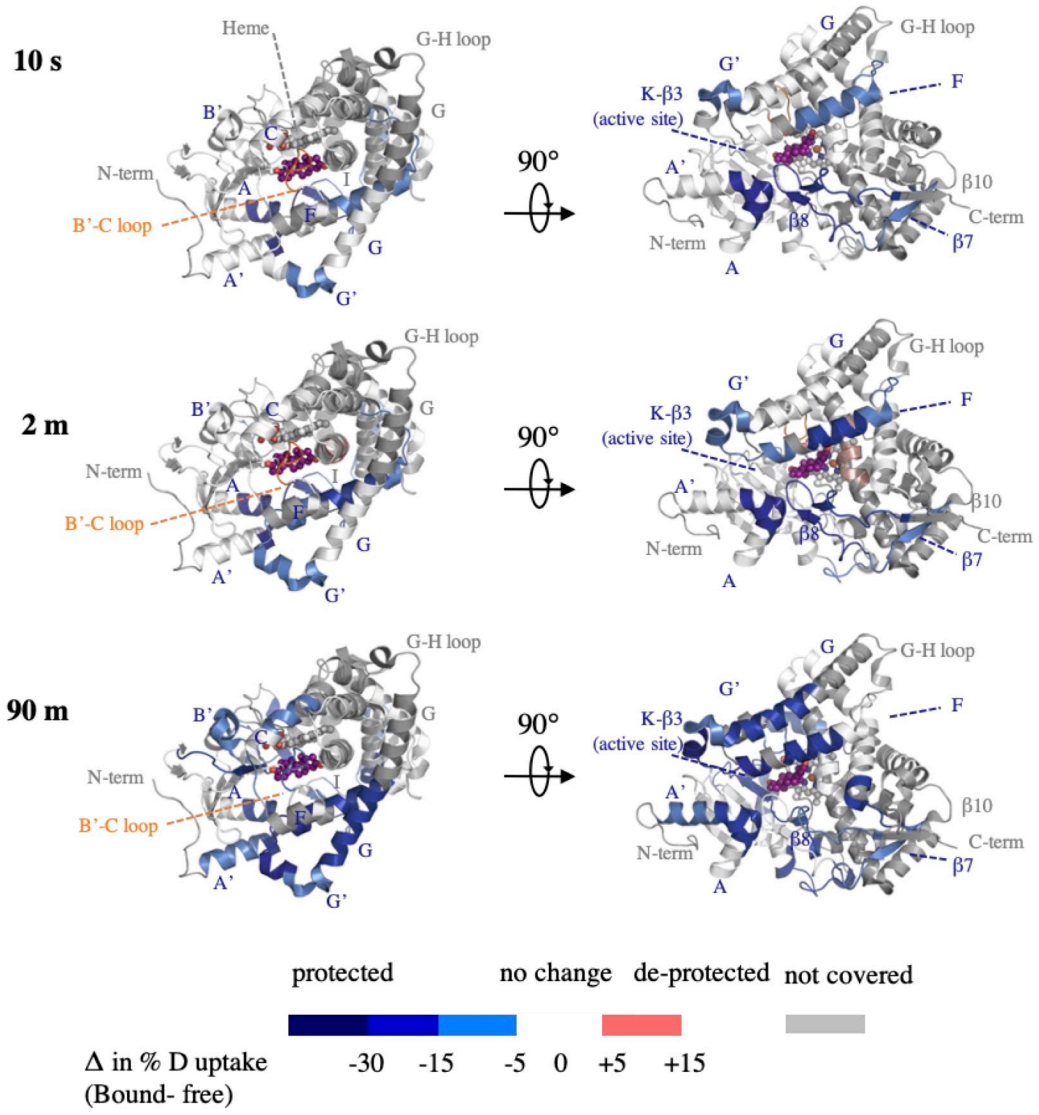

Figure 3.1.6.4. ASD-induced suppression of % deuterium uptake in 19A1 at 10 s, 2 m and 90 m. Heatmap representation of *differences in % deuterium uptake* (ASD-bound state – free state) upon 10 s, 2 m, and 90 m of deuteration, mapped onto the crystal structure of ASD-bound 19A1 (PDB ID: **3EQM**) in two orientations: membrane-bound (left) and flipped ~90° (right) for ease of viewing. Differences are represented on a blue-white-red color scale, where protected regions are shown in blue. The threshold for significant differences is ±6% as calculated from the 0.38 Da CI described in the Methods. The heme and ASD are shown by sphere representation in gray and purple, respectively.

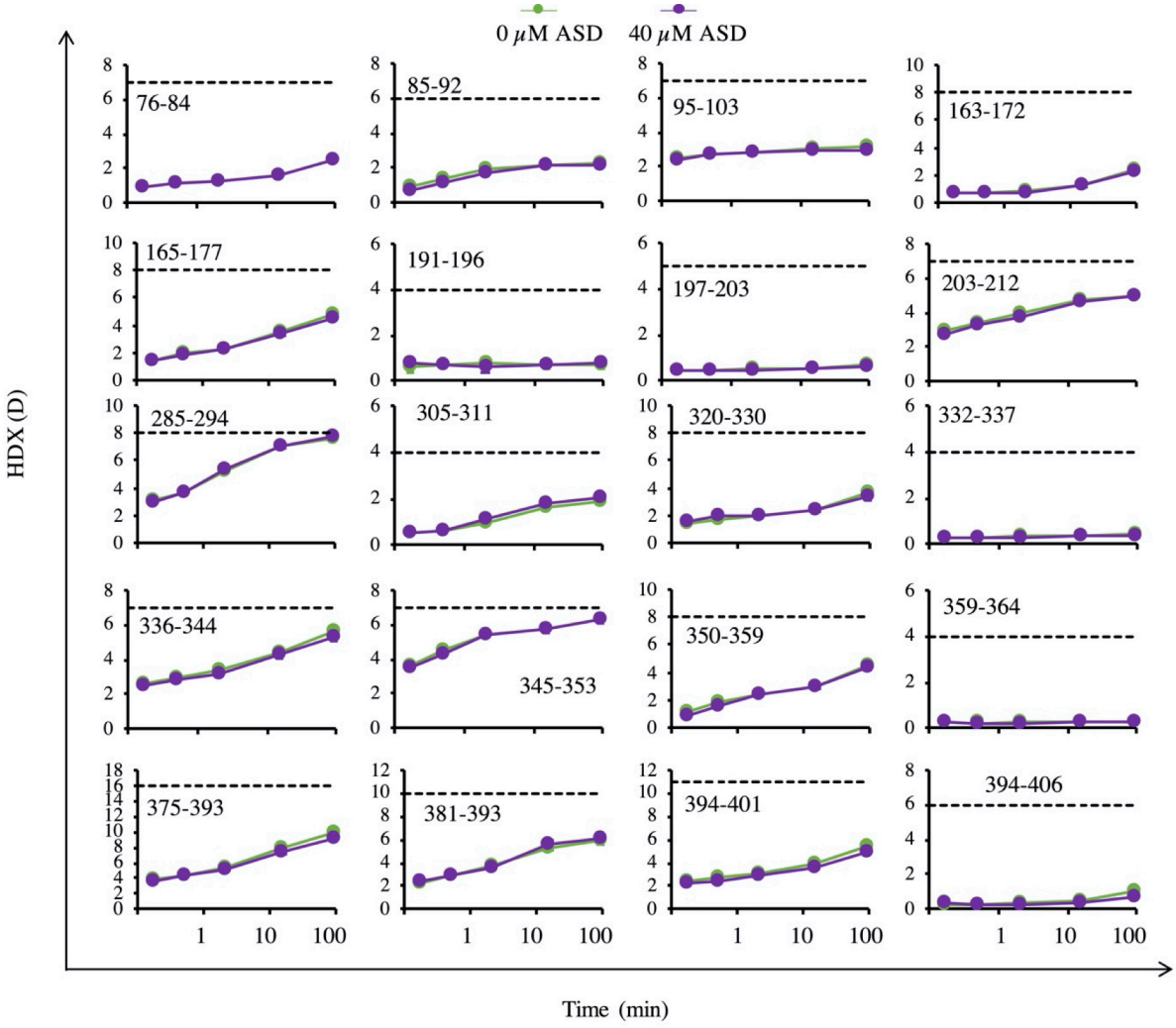

Figure 3.1.6.5. Uptake plots for peptides that show no significant difference in HDX between the free and bound state. The dashed line indicates the theoretical maximum number of amides that can exchange. Error bars are masked by marker size.

3.1.7 Tables

Table 3.1.6.1: Summary of HDX conditions and analysis with 19A1-NDs in the free state and bound to ASD.

DATA SET	FREE	ASD
HDX reaction details	1.3 μM 19A1-ND, 50 mM HEPES, 50 mM NaCl, 2 mM TCEP, 1% EtOH, pH = 7.0, 25 °C	1.3 μM 19A1-ND, 50 mM HEPES, 50 mM NaCl, 2 mM TCEP, 40 μM ASD, 1% EtOH, pH = 7.0, 25 °C
Quench details	1.2% FA, 0.4 % TFA	
pH of quenched undeuterated sample	2.55	
Nanodisc disassembly, lipid removal details	1.05 μmol sodium cholate, 3 mg ZrO_2 resin per sample	
HDX time course (min)	0.17, 0.5, 2, 15, 90	0.17, 0.5, 2, 15, 90
HDX control samples	Maximally-labeled; "10 s" pulsed-labeled after >20 hrs at 25°C	Maximally-labeled
Back-exchange (mean / IQR)	39.48% / 6.5%	
# of Peptides	61	61
Sequence coverage	69%	69%
Average peptide length / Redundancy	9.4/ 1.79	9.4 / 1.79
Replicates (biological or technical)	3 (biological)	3 (biological)
Repeatability	0.112 (average standard deviation)	0.106 (average standard deviation)
Significant differences in HDX (delta HDX > X D)	0.382 D (95% CI)	

3.2 DYNAMICS OF NON-STEROIDAL AROMATASE INHIBITORS ANASTROZOLE AND 7-HYDROXYFLAVONE BINDING TO NANODISC-EMBEDDED AROMATASE

Note. Manuscript in progress. 19A1 nanodiscs were prepared by the Hackett laboratory. MD simulations by John C. Hackett are ongoing and excluded from this section.

3.2.1 Introduction

Aromatase Inhibitors (AI-s) are a class of drugs used to block estrogen synthesis by inhibiting the activity of aromatase or 19A1. Third-generation AI-s are currently recommended by the FDA for treatment of estrogen-dependent breast cancer in postmenopausal women as part of a primary, secondary, or extended therapy with estrogen receptor modulator tamoxifen [252]. They include the steroidal inhibitor exemestane and non-steroidal triazole-based inhibitors anastrozole and letrozole. Exemestane is an irreversible mechanism-based inhibitor that forms a covalent adduct with 19A1 when activated [253]. Anastrozole and letrozole are reversible inhibitors that noncovalently coordinate their triazole moiety to the heme iron and prevent the native substrates from occupying the active site [139].

Despite their success, AI-s have been associated with a series of negative side-effects that are reported in 30-60% of breast-cancer patients [254], [255], and efforts to develop less toxic AI therapeutics are ongoing. The crystal structure of placental 19A1 bound to the steroid substrate, androstenedione, revealed the structural basis for androgen specificity and led to rejuvenated attempts at designing the next generation of AI drugs [136]. Yet, no fourth-generation AI has emerged since exemestane, anastrozole, and letrozole entered the market more than two decades

ago. Additional crystal structures with substrate testosterone and steroidal AI exemestane are now available but no structure with a non-steroidal inhibitor has been published.

Here we report on the effect of two distinct non-steroidal inhibitors on the structural dynamics of nanodisc-embedded 19A1 as probed by hydrogen-deuterium exchange mass spectrometry (HDX-MS). The inhibitors include triazole AI anastrozole (ATZ) and flavonoid inhibitor 7-hydroxyflavone (7HF) (Figure 3.2.5.1). 7HF is part of the flavone class of natural compounds that inhibit the aromatization reaction catalyzed by 19A1 by competing with androgen substrates for the active site [256], [257]. The natural inhibitory capacity of flavones has been exploited to design synthetic flavonoid analogs that may constitute a next-generation AI lead drug, as recently reviewed in [258].

3.2.2 Methods

Protein expression, purification, and ND assembly

19A1-NDs were obtained by the Hackett laboratory as described in section 3.1.2.

Hydrogen-deuterium exchange (HDX), mass spectrometry, and HDX data analysis.

HDX experiments were performed as described in section 3.1.2 with the following modifications: The final concentration of 19A1-ND in the 100 µl HDX sample was 1.1 µM. Due to the greater solubility of 7HF in DMSO, 1% (v/v) DMSO was used as the co-solvent, instead of EtOH. The final concentrations of ATZ and 7HF in the HDX samples were 100 µM and 40 µM, respectively, corresponding to ~20 x the reported K_d values ([228], unpublished). The deuterium labeling time course was expanded to include an 8 h time point to capture the dynamics of the slowly exchanging regions and further probe the EX1 kinetics of the B'-C loop.

One of the three '2 m' replicates for the 7HF-bound dataset was lost in a faulty injection. The final deuterium fraction (D_{frac}) in the HDX samples was 84.5%.

3.2.3 Results

Global dynamics of aromatase

Dynamics of ligand-free, ATZ-bound, and 7HF-bound 19A1-NDs were probed via HDX-MS as described in 3.1.3. Fully deuterated uptake profiles were obtained for each peptide and absolute deuterium uptake values were corrected for back-exchange of the deuterium label during the experiment. Analysis of 64 unique peptides resulted in 68% coverage of the 19A1 sequence. A lower coverage was obtained for the B-C region, as parts of the B-helix and B-B' loop (peptide 104-116) could not be analyzed. In contrast, coverage was gained in the previously unresolved C-D loop (peptide 149-157). The labeling reaction proceeded to >95% for rapidly exchanging peptides, whereas buried regions in the K-helix and E-helix had <20% H/D exchange after 8 hours of the deuterium labeling reaction. Deuterium uptake profiles for the ligand-free 19A1 are consistent with previously published results described in 3.1.3.

Comparison of HDX profiles of ligand-free and ATZ-bound 19A1

HDX was performed at 100 μM ATZ. The saturating concentration of ATZ was chosen based on a K_d of 0.48 μM reported by the Hackett laboratory for ATZ binding to 19A1-NDs (unpublished). The differences between the ATZ-bound and free states are summarized in Figure 3.2.5.2-A and color-mapped onto the 19A1 crystal structure in Figure 3.2.5.2-B. A peptide was considered protected from HDX if the difference in deuterium uptake between the bound and free states is statistically significant for two consecutive time points. The 20 h time point was considered in the identification of protected peptides in cases where in addition to a statistically significant

difference at 8 h, there was a clear difference (> 99% CI) at 20 h as well. Herein, we show that the presence of ATZ suppressed HDX of 19A1 at the following regions: A'-helix (peptide 56-64), A-β1 loop (peptide 76-84), B'-C loop (peptide 125-140), part of the I-helix (peptide 304-312), K-β3 region (peptide 372-380), and K'-K'' region (peptide 394-406) (Figure 3.2.5.2). The largest effects on dynamics were observed in the active site (B'-C loop, I-helix, K-β3) and membrane-associated A'-helix. Significant protection of loops connecting the N-term beta domain to the A and B-helices was observed at the 8 and 20 h time points only. Notably, the dynamics of the A'-A turn motif, F-G helices and β8-β10 sheets at the C-terminus, three regions that are strongly perturbed by the native substrate ASD, remained unaltered in the presence of ATZ.

Comparison of HDX profiles of ligand-free and 7HF-bound 19A1

Binding of 7HF to 19A1-NDs is described by a single-site binding model with a K_d of 0.22 μM [228]. The reported K_d value guided the choice of 40 μM (20x K_d) as a saturating concentration of 7HF in the HDX experiments. The differences between the 7HF-bound and free states are summarized in Figure 3.2.5.3-A and color-mapped onto the 19A1 crystal structure in Figure 3.2.5.3-B. The presence of 7HF suppressed HDX of 19A1 at the following regions: A'-helix (peptide 56-64), A-β1 loop (peptide 76-84), β2-B loop (peptide 95-103), B'-C loop (peptide 125-140), C-helix (peptide 141-149), C-D loop (peptide 149-157), F-G region (peptides 213-221 and 241-256), I-helix (peptide 304-312), K-β3 region (peptide 372-380), and the β6-K' region (peptides 394-406, 407-413) (Figure 3.2.5.3). The largest effects on dynamics were observed at the B'-C loop and K-β3 region in the active site, followed by moderate protection at the membrane-associated A'-helix, and C-D loop. Unlike the other protective effects observed, the unique protection with 7HF at the C-D loop dissipates at the later time points of the HDX reaction.

As with ATZ, the dynamics of the A'-A turn motif and the β8-β10 sheets were not perturbed. The F and G-helices are protected in the presence of 7HF, but the effects on dynamics in this region are more modest than those of the native substrate, ASD.

Comparison of HDX profiles of ATZ-bound vs. 7HF-bound 19A1

Differences between the effects of the two inhibitors on 19A1 dynamics are summarized in Figure 3.2.5.4. Deuterium uptake of 19A1 peptides in the ATZ-bound state was subtracted from the 7HF-bound state and significant differences between the 7HF-bound and ATZ-bound states were established based on criteria described in methods. Both inhibitors suppressed HDX at the active site (B'-C loop, K-β3 region, I-helix), membrane-associated A'-helix, and part of the A-helix and loop connecting it to the N-terminal beta domain. The effects of 7HF extended to the F-helix (213-221), F-G' loop (228-235), C-D loop (149-157) and D-helix (165-172). 7HF also had a stronger effect on the dynamics of the B'-C loop. Even though peptides corresponding to the loop connecting the L-helix to the β7 sheet and β8-β10 sheets are not significantly protected with any individual inhibitor, the sum of the HDX differences between the two bound states across the 10 s – 8 h time course indicates a potential protective effect in the 7HF-bound state relative to the ATZ-bound state. (Figure 3.2.5.4). Overall, the HDX signatures of the two inhibitors are similar, with 7HF having an impact at few additional regions, akin to the global effects observed with the native substrate, ASD. Neither inhibitor shows the strong protection observed with ASD at the A'-A turn motif and C-terminus loop. Part of the I-helix containing several residues in contact with ASD in the crystal structure of the ASD-bound complex that showed no difference in HDX relative to the free state in 3.1.3, was protected from HDX in the presence of either inhibitor.

Lastly, as observed in our previous work, the B'-C loop showed a bimodal distribution in the free state that was not present in the ATZ-bound and 7HF-bound states (Figure 3.2.5.5). The addition

of an 8 h time point confirmed the presence of EX1 kinetics, as the exchanging of the two populations in the bimodal distribution of the B'-C loop progressed further.

3.2.4 Discussion

In our previous work, we demonstrated that the native substrate androstenedione has a global stabilizing effect on the backbone dynamics of 19A1, in agreement with the stabilizing effect of ASD on the 19A1 structure observed previously by other methods [93]. The suppression of dynamics was most pronounced at the A'-A, F-G, and β8-β10 regions of the protein. The β8-β10 fragment, which was fully exchanged in free 19A1, retained more than half of its amide hydrogens in the presence of ASD, resulting in >60% protection at the earliest time points of the deuterium labeling reaction. We suggested that the A'-A and β8/9 turns underwent a similar ASD-induced change in dynamics based on their close spatial proximity and similar kinetics of HDX suppression. Residues in the protected β8-β10 fragment are part of the active site (S478, L479, H480) and access channels S[5] (L477, S478) and 2d (H475, L477, S478, L479), whereas G71 and N75 from the A'-A turn line part of the 2d access channel. Interestingly, MD simulations performed by Park *et al.* suggested the existence of a charged hydrophilic pocket with unknown pharmacological relevance containing the openings of the 2d channel and Channel 5 formed by the A, K, K' helices, β8-β9 sheets and K-β3 loop. All components of this pocket showed decreased HDX in the presence of ASD. Speculatively, the joint protection at the A'/A and β8/9 turns may implicate the 2d channel in the mechanism of ASD binding to 19A1, based on the observation that residues 71 and 475 from the 2d channel display the shortest distance between the A'/A and β8/β9 fragments: the backbone carbonyl oxygen of H475 is positioned

[5] Channels are named according to standard P450 channel terminology.

only 3.3 Å away from the backbone amide nitrogen of G71 in the ASD-bound structure. Most notably, the protection of the A'-A and β8/9 turns is not observed in the presence of either inhibitor. In general, the differences between the bound and free states are greater for ASD than 7HF or ATZ, suggesting distinct dynamic signatures between the preferred substrate and other ligands. In lieu of crystal structures with non-steroidal ligands, the interaction between 19A1 and ATZ has been investigated by docking ATZ to the 19A1 active site [259]. A model of the 19A1-ATZ complex proposed that one cyanoisopropyl group of ATZ occupies the cleft between the I-helix and β8 sheet, and the other resides near the B'-C loop. Two H-bonds between ATZ and residues T310 and D309 on the I-helix help orient ATZ in the active site. Furthermore, among 16 tested 19A1 mutants, the D309A mutant dramatically decreases the binding affinity for ATZ. Other mutants such as I133Y, E302D, S478T and H480K also decrease binding affinity for ATZ, whereas T310S, I474Y, I474M, and I474N have increased affinity for ATZ. It should be noted that the D309A mutant is catalytically inactive with steroid substrates and D309 has been implicated as a critical residue in the catalytic cycle of 19A1. Surprisingly, peptide 304-312 containing several I-helix residues in the active site, including D309, did not show a difference in deuterium uptake in the ASD-bound vs free state, but is decisively protected from HDX in the presence of ATZ and 7HF. The effect of ATZ on 19A1 dynamics is primarily localized on the active site, indicating a smaller stabilizing effect on the 19A1 structure relative to the native substrate, in agreement with previous calorimetry data showing a 3°C increase in T_m of 19A1 in the presence of ASD, but not ATZ [93]. In addition to the protein regions affected by ATZ, 7HF binding alters the backbone dynamics of the F-G and C-D regions, aligning more closely with the dynamic profile of the native substrate, ASD. The HDX results reflect the structural similarities of the three ligands: ASD and 7HF are planar hydrophobic compounds with limited

flexibility and similar scaffold, whereas ATZ is bent, polar, and more flexible. Other than regions in the active site, all three ligands suppress the backbone dynamics of the membrane-associated A'-helix that contributes residues to access pathways. MD simulations in 3.1.3 revealed that the A'-helix is distorted in the presence of ASD and sinks deeper in the membrane upon ASD binding. Previous MD simulations have shown that the A'-helix partially unfolds during simulations and the unfolding has been attributed in part to interaction with the lipid interface [260], [261]. It is likely that ligands stabilize the A'-helix, resulting in the decreased HDX observed. The stabilizing effect of ligands was also observed in the dissipation of bimodal patterns of the B'-C loop in favor of the more slowly exchanging conformation of 19A1.

3.2.5 Figures

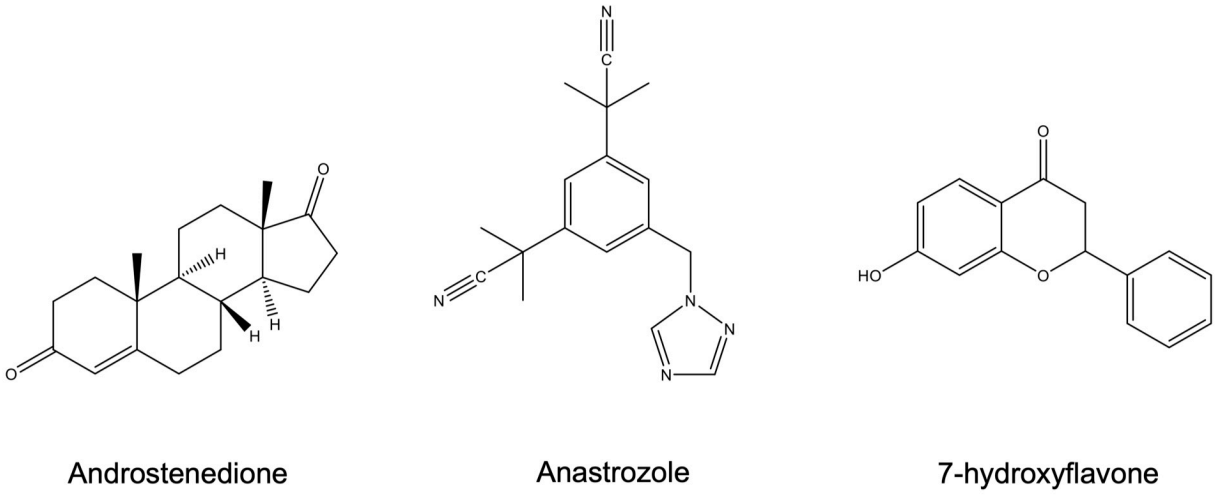

Figure 3.2.5.1. Structures of the substrate and inhibitors of 19A1.

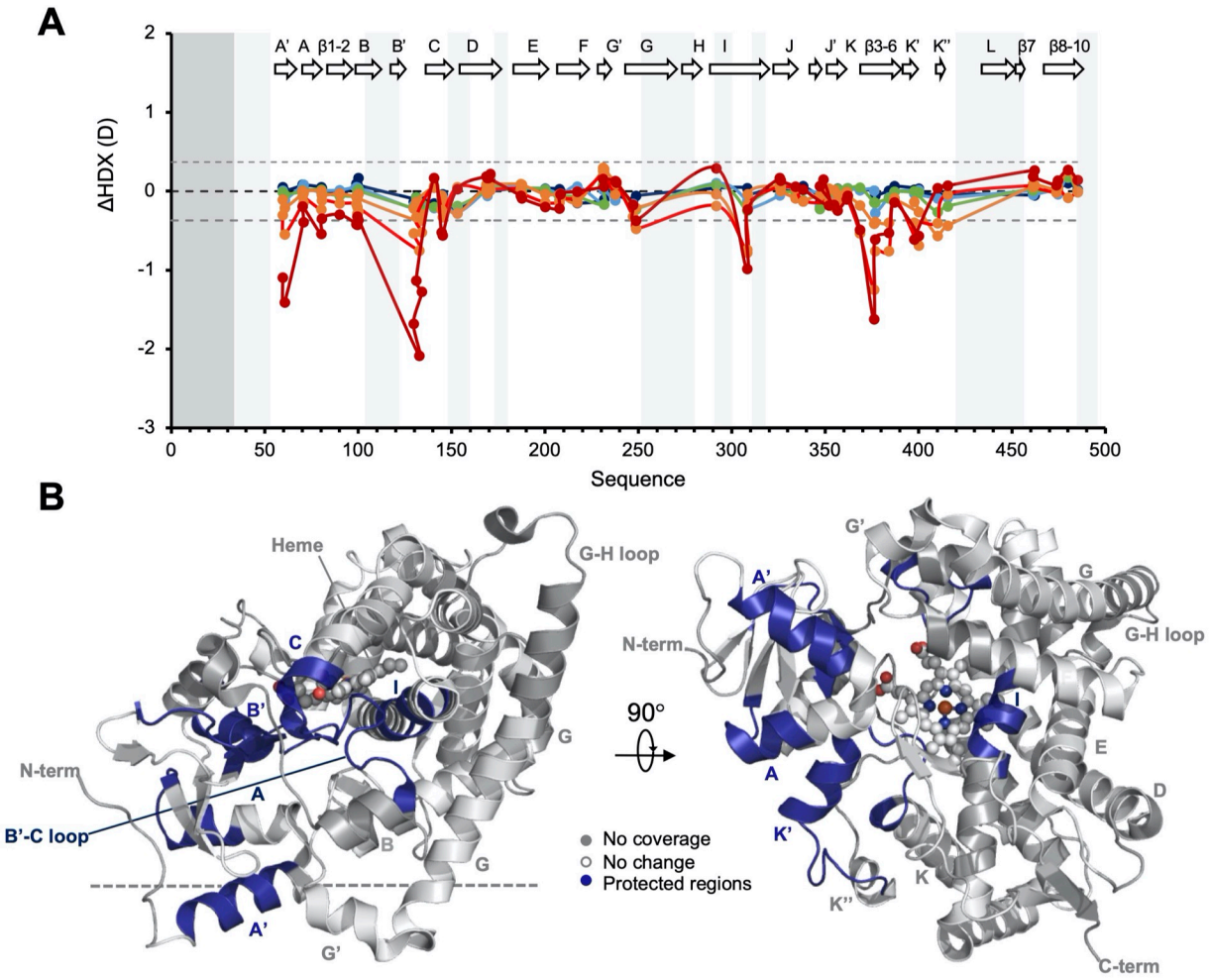

Figure 3.2.5.2. Anastrozole (ATZ)-induced suppression of HDX in 19A1. **A.** Differences in HDX (ATZ-bound state – free state) after 10 s (dark blue), 30 s (light blue), 2 m (green), 15 m (orange), 90 m (red), and 8 hr (dark red) of deuteration. Peptides are represented by the midpoint of their sequence. The dashed gray lines at -0.37 D and +0.37 D indicate the respective negative and positive threshold for a significant difference (CI 95) in uptake between the two states. Regions with no coverage are shaded gray. The first 35 residues (in dark gray) are not expressed. **B.** Heatmap of differences in HDX on the crystal structure of 19A1 (PDB ID: **3EQM**) in two orientations: membrane-bound (left) and flipped ~90° (right) for ease of viewing. The heme is shown by spheres in gray.

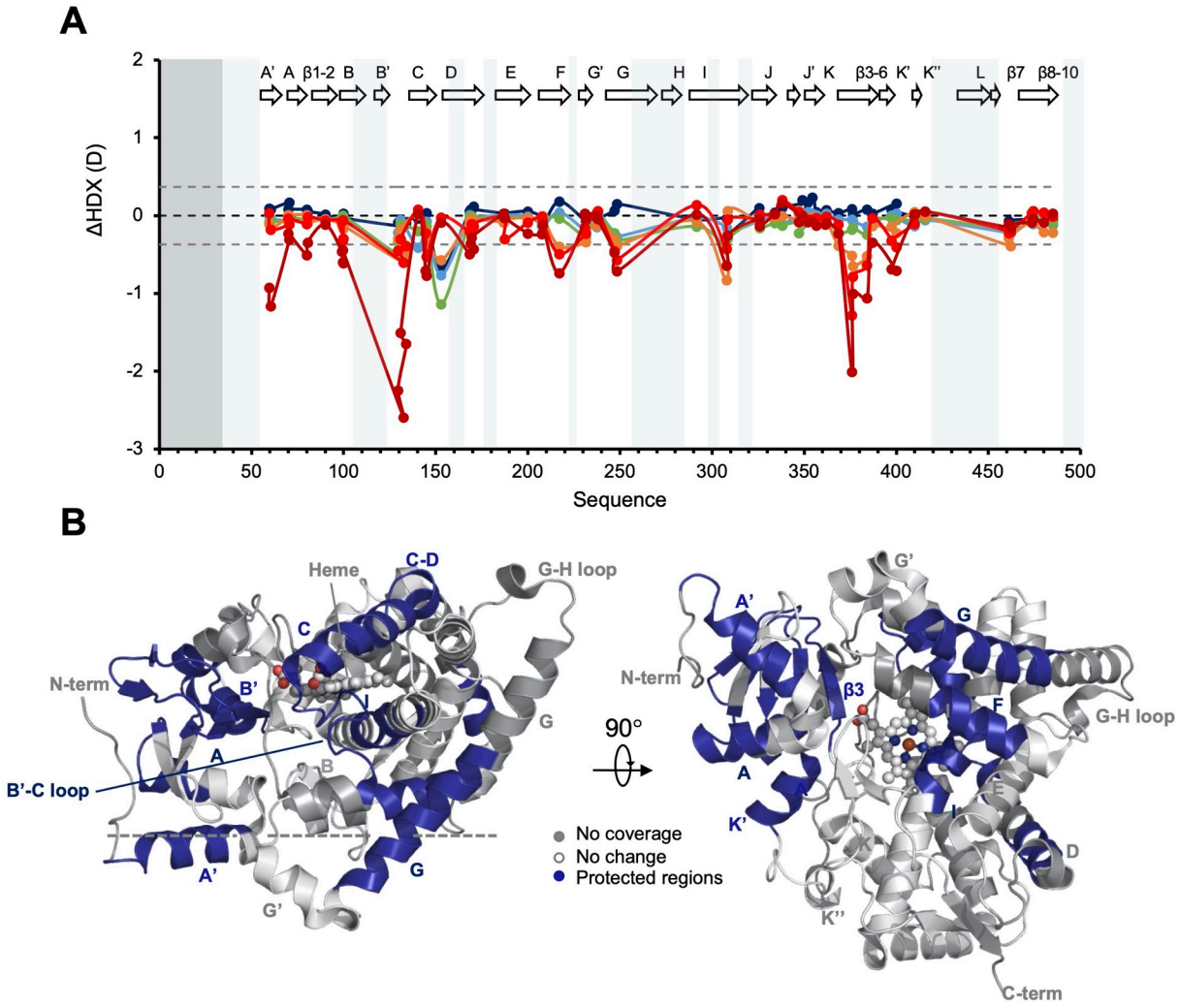

Figure 3.2.5.3. 7-hydroxyflavone(7HF)-induced suppression of HDX in 19A1. **A.** Differences in HDX (7HF-bound state – free state) after 10 s (dark blue), 30 s (light blue), 2 m (green), 15 m (orange), 90 m (red), and 8 hr (dark red) of deuteration. Peptides are represented by the midpoint of their sequence. The dashed gray lines at -0.37 D and +0.37 D indicate the respective negative and positive threshold for a significant difference (CI 95) in uptake between the two states. Regions with no coverage are shaded gray. The first 35 residues (in dark gray) are not expressed. **B.** Heatmap of differences in HDX on the crystal structure of 19A1 (PDB ID: **3EQM**) in two orientations: membrane-bound (left) and flipped ~90° (right) for ease of viewing. The heme is shown by spheres in gray.

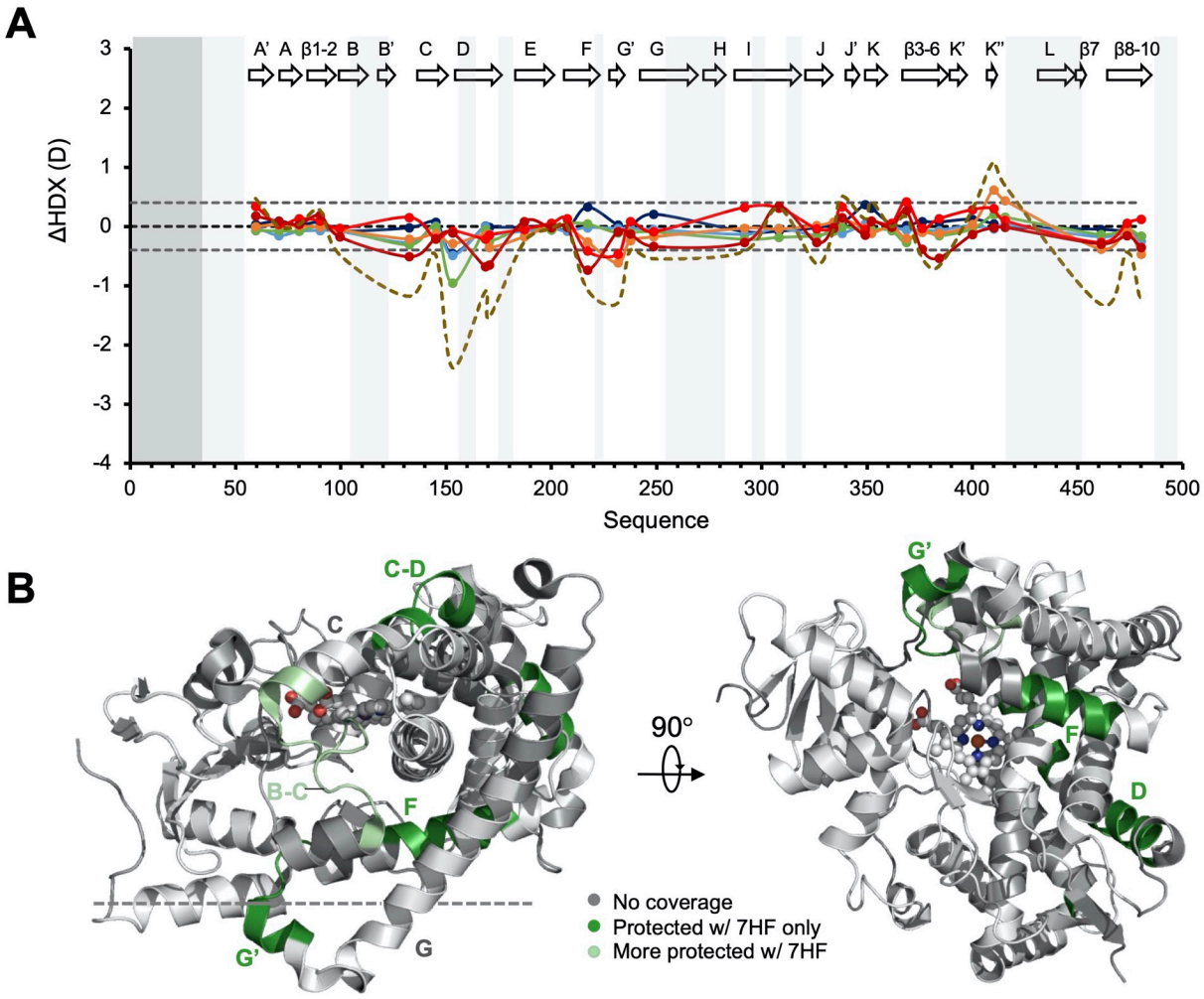

Figure 3.2.5.4. HDX comparison between nonoverlapping peptides in 7HF-bound and ATZ-bound 19A1. A. Differences in HDX (7HF-bound state – ATZ-bound state) after 10 s (dark blue), 30 s (light blue), 2 m (green), 15 m (orange), 90 m (red), and 8 hr (dark red) of deuteration. The dashed gold line indicates the sum of differences between the two states across all time points. Peptides are represented by the midpoint of their sequence. The dashed gray lines at -0.37 D and +0.37 D indicate the respective negative and positive threshold for a significant difference (CI 95) in uptake between the two states. Regions with no coverage are shaded gray. The first 35 residues (in dark gray) are not expressed. **B.** Regions affected by only one ligand (by 7HF in dark green, by ATZ in purple) highlighted on the crystal structure of 19A1 (PDB ID: **3EQM**) in two orientations: membrane-bound (left) and flipped ~90° (right) for ease of viewing. The heme is shown by spheres in gray.

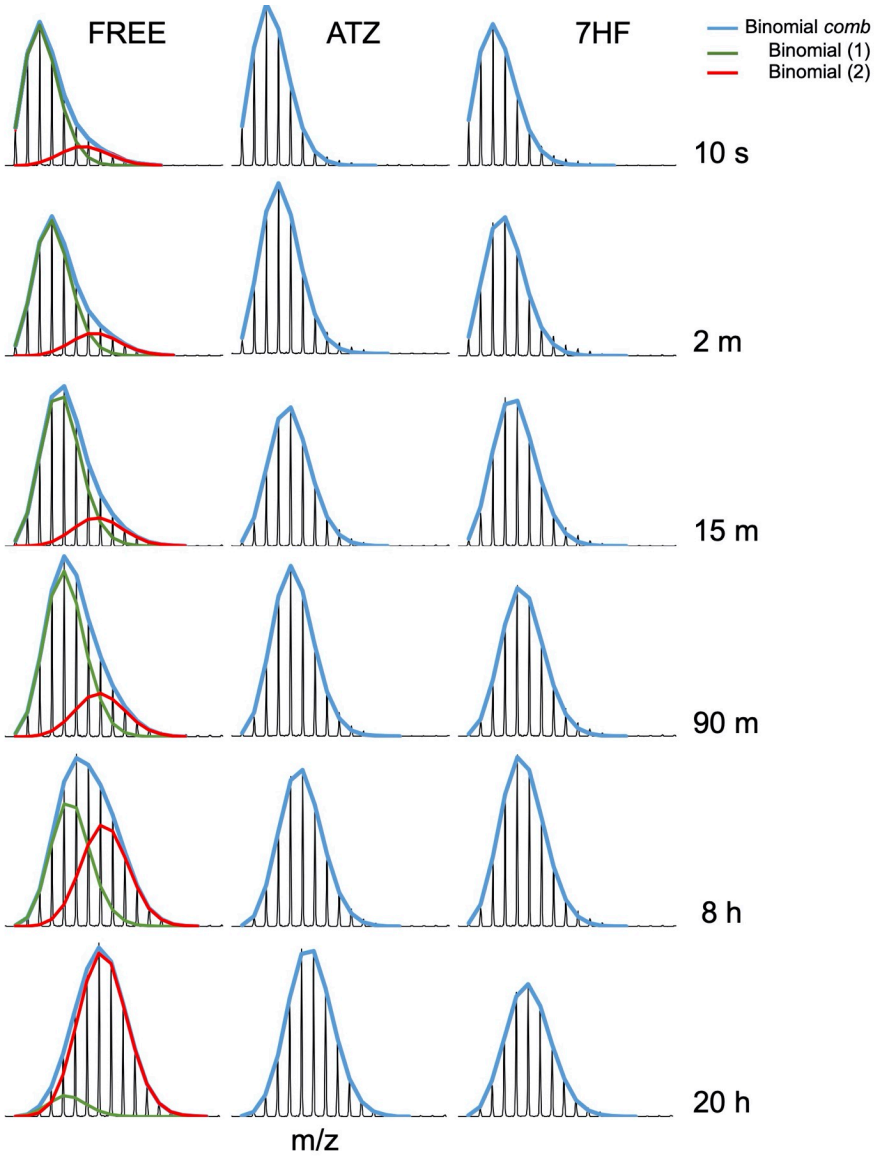

Figure 3.2.5.5. **Bimodal patterns of the B'-C loop (peptide 125-140) in the absence or presence of 19A1 inhibitors.** The bimodal deconvolution was statistically significant in the free state only.

3.2.6 Tables

Table 3.2.6.1. Summary of HDX conditions and analysis with 19A1-NDs in the free state and bound to ATZ or 7HF.

DATA SET	FREE	ATZ	7HF
HDX reaction details	1.1 µM 19A1-ND, 50 mM HEPES, 50 mM NaCl, 2 mM TCEP, 1% DMSO, pH = 7.0, 25 °C	1.1 µM 19A1-ND, 50 mM HEPES, 50 mM NaCl, 2 mM TCEP, 100 µM AZ, 1% DMSO, pH = 7.0, 25 °C	1.1 µM 19A1-ND, 50 mM HEPES, 50 mM NaCl, 2 mM TCEP, 40 µM 7HF, 1% DMSO, pH = 7.0, 25 °C
Quench details	1.2% FA, 0.4 % TFA		
pH of quenched undeuterated sample	2.55		
Nanodisc disassembly, lipid removal details	1.05 µmol sodium cholate, 3 mg ZrO_2 resin per sample		
D_{frac}	0.845		
HDX time course (min)	0.17, 0.5, 2, 15, 90, 480, 1200*	0.17, 0.5, 2, 15, 90, 480, 1200*	0.17, 0.5, 2, 15, 90, 480, 1200*
HDX control samples	Maximally-labeled	Maximally-labeled	Maximally-labeled
Back-exchange (mean / IQR)	30.5% / 8.1%		
# of Peptides	64		
Sequence coverage	68%		
Average peptide length / Redundancy	9.81/ 2.01	9.81/ 2.01	9.81/ 2.01
Replicates (biological or technical)	3 (technical)	3 (technical)	3* (technical)
Repeatability	0.092 (average standard deviation)	0.116 (average standard deviation)	0.117 (average standard deviation)
Significant differences in HDX (delta HDX > X D); (AZ/7HF-Free)	NA	0.364 D (95% CI); 0.812 D (99% CI)	0.367 D (95% CI); 0.817 D (99% CI)

2 replicates for t=1200 min- not included in the final analysis
2 replicates for t=2 m for 7HF-bound dataset

Chapter 4. REVERSIBILITY OF GLUTATHIONE CONJUGATION OF NONENAL BY GSTA1-1 AND GSTA4-4

Michele Scian expressed and purified the GST enzymes, synthesized GS-nonenal, and first discovered and characterized H/D exchange of nonenal by kinetic ^{1}H NMR assays. I performed kinetic NMR experiments with M. Scian under his supervision and independently, as well as determined the rate of H/D exchange reported here. I designed and performed the UV-VIS enzymatic assays with nonenal and prepared samples for LC-MS enzymatic assays. James Movius and Dale Whittington developed the LC-MS method for GS-nonenal quantitation. Taylor Murphree synthesized and purified GS-nonenal used to prepare samples for LC-MS analysis using the method developed by M. Scian.

4.1 INTRODUCTION

Glutathione transferase A4-4 (GSTA4) is an alpha class glutathione transferase that is highly efficient toward lipid alkenal peroxidation products such as 4-hydroxynonenal (HNE) and trans-2-nonenal (nonenal) (Figure 4.5.1) [262]. The unusual selectivity toward a specific class of substrates contrasts the promiscuous activity of canonical cytosolic GSTS, including that of closely related isoform, GSTA1-1, as discussed in section 1.5.1 of Chapter 1. Electrophilic compounds of lipid peroxidation accumulate to toxic levels under oxidative stress reacting with a wide range of intracellular components via Michael addition at the olefin or nucleophilic attack at the aldehyde [263]. Lipid alkenals of particular interest include 4-hydroxynonenal (HNE), a major product of arachidonic acid oxidation, and trans-2-nonenal (nonenal), an oxidation product of omega-7

unsaturated fatty acids. HNE has been widely implicated in cytotoxicity and diseases such as cancer, cardiovascular and neurodegenerative disorders [264], [265]. However, it has been found that at low levels, HNE acts as an intracellular signaling molecule that elicits cell differentiation, proliferation, and cytoprotective responses to oxidative stress [266]. Specifically, the Keap-Nrf2-ARE pathway is activated at low concentrations of HNE to maintain adequate antioxidant responses resulting in cells becoming hypersensitive to oxidative stress [264]. The concentration-dependent dual role of HNE as a toxic metabolite and regulatory second messenger suggests that its levels might be controlled via cellular pathways [267]. Since glutathione (GSH) conjugation is an established clearance pathway for lipid alkenals [268] and GSTA4-4 is selective toward lipid alkenal substrates, we hypothesized a possible role for GSTA4-4 as a regulatory enzyme that contributes to the regulation of lipid alkenal levels by efficiently catalyzing the reverse reaction with GS-lipid alkenal conjugates. The ability of GSTA4 to catalyze the reverse reaction, a r*etro* Michael addition, has not been studied, despite the documented ability of other GSTs to catalyze *retro* Michael additions with other α, β-unsaturated substrates [269], [270]. Interestingly, GSTs have been suggested to catalyze the *retro* Michael addition using GS-HNE as a substrate in rat liver cytosol, but no mechanistic details were studied [271]. Here we considered the ability of GSTA4-4 to catalyze the *retro* Michael reaction with a GS-nonenal conjugate and contrasted it to that of the promiscuous isoform, GSTA1-1.

4.2 METHODS

GST expression and purification

Human GSTA4-4 and GSTA1-1 were expressed in *E. coli* and purified by affinity chromatography using S-hexylglutathione Sepharose as previously described [28], [262], [272], [273]. Purity of the proteins was confirmed by SDS-PAGE and the purified protein solutions were dialyzed against

100 mM sodium phosphate buffer (NaPi), pH 6.5, to remove glutathione (GSH). Stock solutions of freshly prepared enzymes were finally buffer exchanged with 100 mM NaPi, pH 6.5, and aliquots were stored at –80 °C. The following molar extinction coefficients were used to determine the concentration of GST dimers: ε_{280} = 46,147 $M^{-1}cm^{-1}$ for GSTA4-4 and ε_{280} = 34,300 $M^{-1}cm^{-1}$ for GSTA1-1 [274]. All enzyme concentrations are reported here as concentrations of dimeric species. GSTA1-1 and GSTA4-4 used in the LC-MS analysis was purchased from Sigma-Aldrich and activity was tested via the CDNB activity assay prior to preparing samples.

CDNB activity assay

Enzymatic activity of GSTA4-4 and GSTA1-1 was measured by monitoring the GST-mediated conjugation of reduced L-Glutathione (≥ 98 %) to standard GST substrate, 1-chloro-2.4-dinitrobenzene (CDNB). The GS-DNB conjugate produces a dinitrophenyl ether that can be detected spectroscopically at 340 nm with an extinction coefficient of 9,600 M^{-1} cm^{-1}, as described originally by [275]. Briefly, the reaction of 1 mM GSH with 1.5 mM CDNB by 1-2 μM GSTA4-4 or 125 nM GSTA1-1 was monitored at T = 25°C for 1 min in 100 mM NaPi, pH 6.5, 5% (v/v) ethanol. The concentrations of enzymes were chosen to ensure linear formation of GS-DNB with <10% substrate depletion during 1 min of reaction monitoring time. Enzymatic activity of GSTA4-4 and GSTA1-1 was routinely measured prior to NMR, UV-VIS, and LC-MS assays with nonenal. Storage of GSTs at 4°C did not affect GST activity over a three-day period (data not shown).

Synthesis and purification of GS-nonenal

GS-nonenal product formation was initiated by mixing 500 mL of 1 mM nonenal (97 %, Sigma-Aldrich, St. Louis, MO) with 2 mM GSH in 50 mM KPi, pH 7.0, 2% (v/v) DMSO, at RT. The reaction was monitored by ^{1}H NMR for 6 hours before lowering the pH to 3.0 with 1 M HCl. The reaction mixture was then applied to SPE cartridges (Solid Phase Extraction with Waters

Sep-Pak tC18 6 cc Vac cartridge, 500 mg sorbent) in 25 ml aliquots for bulk separation of reaction mix components. Following loading of each aliquot, the SPE cartridge was washed with 2 x 5 mL 0.1% FA and 3 x 5 ml H_2O and the GS-nonenal product was eluted with 1 mL of 70% ACN. At -20 °C the 70% ACN solution forms two phases, where GS-nonenal is contained in the bottom aqueous layer. The latter was purified by RP-HPLC with a Syncronis aQ, 10x250 mm, 5 µm C18 column (Thermo Scientific) using a 5-74% mobile phase B gradient for 11.5 min at 4 ml/min (A: H_2O + 0.1% FA; B: ACN + 0.1% FA). The isolated LC fractions were analyzed by NMR (1D; 2D COSY, 2D TOCSY) and MS (direct infusion to Waters Synapt G1) to confirm formation of pure GS-nonenal product.

^{1}H NMR peak assignments of nonenal and GS-nonenal

NMR experiments were performed on a Varian Unity-Inova spectrometer with a 500 MHz ^{1}H frequency and a triple-resonance z-axis pulse-field gradient probe (11). NMR spectra of nonenal and GS-nonenal were acquired at a resolution of 32k points in the time domain (16k complex) with 64 accumulations each (sw = 6000 Hz, d1 = 3 s), and sodium 2,2-dimethyl-2-silapentane-5-sulfonate (DSS) as the internal chemical shift reference.

NMR sample preparation and kinetic assays

GST-catalyzed or spontaneous reactions of nonenal with GSH were monitored by ^{1}H NMR over time. NMR spectra were collected with WET water suppression (freq. 177.2 Hz, 4.69 ppm, 299 Hz width, SEDUCE shape) at 25°C in duplicate runs. The amount of water present was minimized by buffer-exchanging all components in deuterated KPi buffer. To make the deuterated buffer, 100 mM KPi in water was dried under vacuum and subsequently dissolved in D_2O "100%" (D, 99.96%, Cambridge Isotope Laboratories).When necessary, suppression of the background signals arising from higher concentrations of protein used, was achieved by relaxation filtering using a $T1_{rho}$ spin-

lock [276]. A 30 ms spin-lock pulse was found to be long enough to effectively remove the enzyme signals without considerably affecting the nonenal resonances.

Spectra were processed in Vnmrj with an exponential apodization function (1 Hz line-broadening) and zero-filling to 32k complex points before Fourier transformation. Following FID processing, Bernstein polynomial baseline correction (polynomial order, 3) was applied to improve peak integration accuracy. Reaction times in the kinetic assays were corrected for the dead time t_0 between sample mixing and spectra acquisition.

H/D exchange at C2 of nonenal

Representative NMR samples for comparing the rate of H/D exchange to that of product formation (measured by the UV assay) were prepared as follows. 10 nM GSTA4-4 was mixed with 20 μM GSH in 100 mM KPi, pH*= 6.76, and the reaction was initiated with 200 μM nonenal in DMSO-d6. Final concentration of DMSO-d6 in the 600 μl sample was 2 % (v/v). Spectra were acquired in 97 increments with nt = 256 scans/increment, t = 1.02236 s, d_1 = 1.0 s, delay = 0 s, ss = 0, t_0 =137 s, and total dead time = 6 m 44 s.

For the GSTA1-1 samples, 10 μM GSTA1-1 was mixed with 40 μM GSH in 100 mM KPi, pD = 6.5, and the reaction was initiated with 200 μM nonenal, 1% (v/v) DMSO. Analogous samples were prepared without enzyme to correct for any spontaneous H/D exchange of nonenal. Spectra were acquired in 150 increments with nt = 256 scans/increment, t_{scan} = 1.02236 s, delay = 0 s, ss = 0, d_1 = 1.0 s, t_0 = 5 m 52 s, and total dead time = 10 m 19 s.

H/D exchange of nonenal is characterized by the transformation of the H1 aldehyde peak from doublet to singlet splitting and the disappearance of the H2 proton peak as deuterium becomes incorporated at the C2 position, instead. The decay of the H2 signal was used to measure the rate of H/D exchange by plotting the area under the H2 peak (peak integration window: 6.080 - 6.155

ppm) against time and fitting the data to a single exponential decay model: $y= Ae^{-kt} + C$, where k is the rate of H/D exchange. Signal decay at H2 also occurs during product formation, but a negligible amount of product is formed at the limiting concentration of GSH used.

GSH dependence of H/D exchange at C2 of nonenal

In a representative experiment, aliquots of GSTA4-4 stock solutions diluted in 100 mM deuterated NaPi buffer at pH* ~ 6.7 were added to freshly made GSH solutions (reduced GSH in 100 mM deuterated NaPi, pH* ~ 6.7, purged with Argon for 1 min) to a final enzyme concentration of 1 μM and GSH concentration of 2.5, 5.0, 10 μM, or 20 μM (in 600 μl total). H/D exchange was initiated by adding 6 μl of 100 mM nonenal stock solution in DMSO-d6 to a final concentration of 1 mM. The final co-solvent concentration in the NMR samples was kept to 1% (v/v). The contribution of the residual GSH present in the enzyme stock solutions was negligible, due to the low protein concentration used for these experiments. Despite careful purging with Argon, the rate of H/D exchange could not be determined at [GSH]<1.5 μM, due to autooxidation of GSH to GSSG. Finally, the rate of H/D exchange could not be reliably measured at higher GSH concentrations due to depletion of a significant molar fraction of nonenal during product formation (data not shown).

GST dependence of H/D exchange at C2 of nonenal

H/D exchange was investigated with 10 nM, 69 nM or 690 nM GSTA4-4 mixed with 100 μM GSH and 1 mM nonenal in 100 mM KPi, pH*=6.5, 2% (v/v) DMSO-d6.

Equilibrium constant of GSH conjugation to nonenal

The reaction of 1 mM nonenal with 2.5 mM GSH in 100 mM KPi, pH* 6.76, was monitored to completion by NMR. The equilibrium constant of the reaction was determined by the ratio of the

H1 aldehyde peak area in nonenal to the sum of peak areas from H1 of nonenal and H1 from the GS-nonenal (hemiacetal peaks: H1', H1'', and H*) product at equilibrium.

UV/VIS kinetic assays of GST-mediated forward and reverse reactions with nonenal

Reaction velocities GSTA4-4- and GSTA1-1-catalyzed GSH conjugation to nonenal were determined in comparable conditions to the ones used in the H/D exchange NMR kinetic assay by monitoring depletion of nonenal at 224 nm via UV spectroscopy using the extinction coefficient: $\varepsilon_{224\ nm}$ = 19,220 $M^{-1}\,cm^{-1}$. Reaction of 20 nM of GSTA4-4 with 20 μM GSH and 200 μM nonenal in 100 mM KPi, pH 6.76, 2% (v/v) ethanol was monitored for 1 min and the reaction velocity was calculated as the amount of nonenal depleted over time in the linear range of the reaction (30s). Reaction of 5 μM GSTA1-1 with 40 μM GSH and 200 μM nonenal in 100 mM KPi, pH 6.5, 1% (v/v) ethanol was monitored for 1 min and the reaction velocity was calculated as the amount of nonenal depleted over time in the first 30 s of the reaction. Dead time of the assay (between initiation and measurement was ~20 s.

The K_m for GSH (nonenal, co-substrate), V_{max}, and k_{cat} kinetic parameters for the forward reaction of GSTA4-4 with nonenal were determined by monitoring depletion of nonenal at varying concentrations of GSH. A mix of 20 nM of GSTA4-4 with 200 μM nonenal was treated with 20 μM – 3 mM of freshly-made reduced GSH to initiate the reaction in 100 mM KPi, pH 6.7, 2%? (v/v) ethanol at 25°C. Due to the high extinction coefficient of nonenal, we were limited to using a subsaturating concentration in the reaction mixture (K_m of nonenal = 180 μM [277]) to avoid saturating the UV detector. Reaction velocities calculated from the amount of nonenal depleted in the linear range (10-30 s) of the reaction were corrected for the contribution of the spontaneous reaction in the range of GSH concentrations used and fit to the Michaelis Menten (MM) model of enzyme kinetics to obtain kinetic parameters in GraphPad Prism.

The K_m, V_{max}, and k_{cat} kinetic parameters for the reverse reaction of GSTA4-4 with nonenal were determined by monitoring appearance of nonenal at 224 nm via UV spectroscopy. GSH, the second product of the reverse reaction, also absorbs at 224 nm but its contribution to absorbance is negligible at the concentrations of GS-nonenal used. 50 nM of GSTA4-4 was treated with 0.5 μM - 200 μM GS-nonenal in 100 mM KPi, pH 6.7, 2% (v/v) ethanol at 25°C. The concentrations of GSTA4-4 and GS-nonenal used were determined from preliminary experiments to allow for linear formation of nonenal in the monitored reaction time (~30s) and an adequate range of GS-nonenal concentrations. As in the forward direction, reaction velocities were corrected for the contribution of the spontaneous reaction, and kinetic parameters were obtaining by fitting the data to the MM model in GraphPad Prism.

LC-MS sample preparation

Samples for GST-catalyzed and spontaneous reactions of nonenal with glutathione in the forward and reverse direction were prepared for preliminary determination of kinetic parameters via LC-MS. In the 'forward reaction' samples, 150 or 160 μl of 50 mM KPi, pH 6.5, and 20 μl of 10x reduced GSH solution freshly prepared in the same buffer were mixed with 20 μl of 10x nonenal stock in 20% ethanol, with or without 10 μl of 20x GST stock solution for a total reaction volume of 200 μl. The final concentration of GSH was kept constant at 1.5 mM for all 'forward reaction' samples. 20 nM GSTA4-4 or 1 μM GSTA1-1 (Sigma-Aldrich) was used in the GST-catalyzed samples. The final concentration of nonenal was 0, 20, 50, 100, 200, 500, 1000, or 1500 μM in the GSTA4-4-catalyzed samples and 0, 5, 10, 20, 50, 100, 200, 500, and 750 μM in the GSTA1-1-catalyzed samples. Nonenal concentrations were chosen based on kinetic parameters obtained by the UV assay. In the 'reverse reaction' samples, 20 μl of 10x GS-nonenal stock solution in 20%

ethanol was added to 170 or 180 µl buffer with or without 10 µl of 20x GST stock solution. The final concentration of GS-nonenal was 0, 5, 10, 20, 50, 100, 200, 500, and 750 µM in the GSTA4-4-catalyzed samples, and 0, 5, 10, 20, 50, 100, 200, 500, 750, and 1000 µM in the GSTA1-1-catalyzed samples. Forward and reverse reaction samples were prepared in duplicate in a well-plate format.

LC-MS assay

Analysis of GS-nonenal (m/z= 448.24) in the reaction mixtures was performed using a Waters Xevo G2-XS QTof instrument. To quantify the amount of GS-nonenal in the samples, a standard curve (0.5-10000 ng/ml) was generated using known amounts of synthesized GS-nonenal. Samples were diluted 1:500 with 80% 100 mM KPi, pH 6.5, 16% MeOH, 4% ethyl acetate prior to injection on LC-MS. LC was performed with an Acquity UPLC, 2.1 x 50 BEH C18, 1.7 µm particle size, column using a 20-100% solvent B gradient (A: 0.1% formic acid, B: acetonitrile, 0.1% formic acid) over ~4 min at 0.3 ml/min. The gradient and column cleaning steps were as follows: 20% B at 0 min, 25% B at 1 min, 80% at 3.5 min, 100% B at 3.8 min, 100% B at 4.5 min, 20% B at 4.6 min. MS acquisition time was 5 min. Peak area analysis was performed with Skyline software.

4.3 RESULTS

Nonenal undergoes solvent H/D exchange in the presence of GST and GSH. For mechanistic investigation of GSTA4 interactions with lipid alkenals, initial NMR studies were done with nonenal, as a model compound for long chain lipid alkenal substrates. The 1D NMR spectrum of nonenal is shown in Figure 4.5.2. When nonenal and a limiting concentration of GSH were incubated with GSTA4-4 in D_2O the NMR signal from the C2 proton of nonenal rapidly

decreased over time (Figure 4.5.3). At the same time, the C1 aldehydic proton of nonenal changed from a doublet to an unexplained singlet without loss of intensity (Figure 4.5.3). Similarly, the C3 proton changed from a well resolved quartet to a poorly resolved broad singlet without any loss of intensity (Figure 4.5.3). The changes in the NMR spectrum were inconsistent with the expected changes during formation of the GS-conjugated nonenal product (GS-nonenal) and occurred without any detectable depletion of nonenal, indicating that nonenal is undergoing H/D solvent exchange at the C2 position. Similar changes in the NMR spectrum were observed when nonenal was incubated with the promiscuous isoform, GSTA1-1, although on a much slower time scale, and only in the presence of high concentrations of enzyme (5-10 μM) (Supporting Figure 4.7.1). NMR spectral changes associated with H/D exchange of nonenal and GS-nonenal product formation are summarized in Table 4.6.1. The observed changes were due to incorporation of solvent deuterons at the C2 position only by measuring the deuterium NMR spectrum of nonenal isolated from incubations with GSTA4-4 (Michele Scian, personal communication). These spectral changes did not occur at any detectable level in the absence of GSH and occurred on a much slower time scale in the absence of enzyme (Figure 4.5.4). When the rate of H/D exchange was determined at variable [GSH], there was dramatic increase in the rates of exchange with increasing [GSH] up to 20 μM (Figure 4.5.4G). Above 20 μM [GSH] the rate of deuterium incorporation became too fast to measure at the concentration of GSTA4-4 tested. Therefore, evidence suggests that the deuterium incorporation at C2 of nonenal is a GST-mediated process that requires a catalytic amount of GSH. To account for this process three possibilities were considered summarized in Figure 4.5.5: 1) A [GST • GS-nonenal] intermediate collapses to GSH and d2-nonenal prior to releasing product, 2) The released GS-nonenal product

is converted by GST to GSH and d2-nonenal in the reverse reaction, 3) A combination of 1) and 2).

H/D exchange is 3–17-fold slower than product formation

A limiting concentration of GSH (20-40 μM) was used in the NMR experiments to slow down the enzymatic reaction so that the kinetics of H/D exchange could be captured in the minutes-hours time scale required for collecting NMR spectra. It was found that at higher concentrations of GSH, a significant molar fraction of nonenal was depleted and spectral changes associated with H/D exchange were confounded with the appearance of NMR signals from the GS-nonenal product. It was not experimentally feasible to directly compare the rate of product formation to the rate of H/D exchange in the same NMR experiment, but it was surmised that product formation is faster than H/D exchange based on the qualitative observation that the H1 signal from GS-nonenal at 9.5 ppm appeared as soon as the first NMR spectrum in the array was recorded and did not change over time while H/D exchange of nonenal was ongoing as indicated by the gradual conversion of the H1 aldehydic doublet to a singlet at 9.2 ppm (Figure 4.5.6). To confirm the qualitative results, we measured the velocity of GSTA4-4- and GSTA1-1-catalyzed product formation by monitoring nonenal depletion at 224 nm via UV spectroscopy in conditions that matched the NMR assay. The velocity of nonenal depletion in the linear range of the reaction was normalized by the concentration of starting nonenal and compared to the rate of H/D exchange obtained from the exponential decay of the H2 proton NMR signal. A summary of the rates of H/D exchange and GS-nonenal formation by GSTA4-4 and GSTA1-1 is shown in Table 4.6.2. GS-nonenal formation was 3.3x faster for GSTA4-4 and 17.4x faster for GSTA1-1. Therefore, H/D exchange proceeds to a greater extent than GS-nonenal formation in the GSTA4-

4 vs. GSTA1-1-catalyzed reaction with nonenal, indicating that GSTA4-4 has a lower commitment to catalysis and/or is more reversible than GSTA1-1.

GSTA4-4 catalyzes the reverse reaction with moderate efficiency

To directly compare reaction reversibility of the two enzymes, steady state kinetic parameters K_m and k_{cat} were characterized for the GSTA4-4- and GSTA1-1-catalyzed forward and reverse reaction with nonenal by UV spectroscopy or LC-MS. Synthesized GS-nonenal product (racemic) was used to characterize the reverse reaction. Preliminary attempts to measure K_m and k_{cat} for the reverse reaction with GSTA1-1 failed by LC-MS and were not attempted by UV due to limited availability of GS-nonenal. Similarly, K_m and k_{cat} for the reverse reaction with GSTA4-4 could not be measured by LC-MS and were obtained by the UV method only. Michaelis Menten plots for both enzymes are shown in Figure 4.5.7. and the calculated kinetic constants are summarized in Table 4.6.3.

The GSTA4-4-catalyzed forward reaction with 20 nM GSTA4-4, 200 μM nonenal, and varying concentrations of GSH (20 μM – 3 mM) in 100 mM KPi, pH 6.7 was monitored by nonenal depletion at 224 nm (Figure 4.5.7A). GSH concentration was varied instead of nonenal because nonenal saturates the UV detector at high concentrations. For the reverse reaction, appearance of nonenal at 224 nm was measured with 50 nM GSTA4-4 and varying concentrations of GS-nonenal (0.5-200 μM) in 100 mM KPi, pH 6.7 (Figure 4.5.7B). Initial velocities in the linear range were plotted against GSH concentration and fit with the Michaelis Menten equation of enzyme kinetics to produce $K_{m\ GSH}$ = 530 μM, k_{cat} = 89 s^{-1}, k_{cat}/K_m = 0.17 s^{-1} μM^{-1} for the forward reaction and $K_{m\ GS\text{-}nonenal}$ = 19 μM, k_{cat} = 1.2 $s^{-}1$, k_{cat}/K_m = 0.06 s^{-1} μM^{-1} for the reverse reaction. When GSH varies, the GSTA4-4- catalyzed forward reaction is only ~2.8x

more efficient than the reverse reaction. However, it should be noted that the concentration of nonenal was not saturating due to high absorbance at 224 nm that saturates the UV detector, and the kinetic constant should be interpreted with caution.

Since GSH is present at mM concentrations in the cell, it is more physiologically relevant to compare catalytic efficiencies of the forward and reverse reactions at saturating GSH concentration. To circumvent the limitations of the UV assay with high concentrations of nonenal, GS-nonenal formation was measured by LC-MS with 20 nM GSTA4-4, 1.5 mM GSH, and varying concentrations of nonenal (20 μM –1.5 mM) in 100 mM KPi, pH 6.5 (Figure 4.5.7C), resulting in the following kinetic parameters: $K_{m\ nonenal}$ = 195 μM, k_{cat} = 1840 s^{-1}. Analogous parameters could not be obtained for the reverse reaction by LC-MS, as it was too slow with the enzyme concentrations tested. Kinetic parameters for the GSTA1-1-catalyzed reaction of nonenal were obtained by LC-MS in the forward direction only with 1 μM GSTA1-1, 1.5 mM GSH and varying concentration of nonenal (5 –750 μM) (Figure 4.5.7D, resulting in $K_{m\ nonenal}$ = 71 μM, k_{cat} = 10.7 s^{-1}. It should be noted that the quantitation of GS-nonenal via the LC-MS assay is problematic as an unknown source of error resulted in overestimated k_{cat} values. This is based on the quantitation of control samples with known amounts of GS-nonenal showing at least a three-fold higher concentration by LC-MS than the known concentration. Thus, the amount of GS-nonenal is likely overestimated in all the samples and the assay and standard curve need repeating. This error should not affect the K_m values.

4.4 Discussion and Future Directions

Although the Haldane Relationship demands specific constraints on kinetic parameters in each direction for a reversible enzyme-catalyzed reaction with substrate and products in equilibrium,

the reverse reaction is not studied in many cases. The ability of GSTs to catalyze *retro* Michael additions has been documented but a detailed analysis of the reaction coordinate has been provided in only one case, wherein rat GSTM isoforms reversibly conjugate GSH to a trans-4-phenyl-3-butene-2-one (PBO) [269]. Because HNE or other lipid alkenals are potential second messengers that regulate antioxidant stress responses, *retro* Michael addition of their GSH conjugates could be an important contribution to the regulatory process and their overall biological effects.

For a general reversible bi uni reaction A+B⇌P, the forward and reverse catalytic constants are related to the overall chemical equilibrium K_{eq} by the Haldane relationship modified for an enzyme with two substrates:

$$\frac{V^f_{max}}{K_{m_A} K_{m_B}} \quad \frac{K_{m_P}}{V^r_{max}} = \frac{[P]_{eq}}{[A]_{eq}\,[B]_{eq}} = K_{eq} \qquad (1)$$

Substituting in (1) the kinetic parameters obtained for the GSTA4-4-catalyzed reaction of nonenal with GSH ($K_{m\ GSH}$ = 530 ± 100 μM, $K_{m\ nonenal}$ = 195 ± 45 μM, $K_{m\ GS\text{-}nonenal}$ = 19 ± 5 μM, k^f_{cat} = 89 ± 6 s^{-1} (UV) and k^r_{cat} = 1.2 ± 0.1 s^{-1}) results in K_{eq} =13.6 ± 5.6 mM^{-1}.

A direct measurement of K_{eq} was provided by NMR with 1 mM nonenal and 2.5 mM GSH using the ratio of peak integrals for the H1 proton in GS-nonenal and nonenal and the 1:1 nonenal to GSH stoichiometric requirement of the reaction. From

$$\frac{H1_{\ GS\text{-}nonenal_{eq}}}{H1_{\ Nonenal_{eq}}} = \frac{[GS\text{-}nonenal]_{eq}}{[Nonenal]_{eq}} = \frac{[GS\text{-}nonenal]_{eq}}{[Nonenal]_{start} - [GS\text{-}nonenal]_{eq}} = \frac{x}{(1\text{-}x)} = 16.7 \qquad (2)$$

and

$$K_{eq} = \frac{[GS\text{-}nonenal]_{eq}}{[GSH]_{eq}\,[Nonenal]_{eq}} = \frac{x}{(2.5\text{-}x)^*\,(1\text{-}x)} \qquad (3)$$

it follows that the K_{eq} of the reaction is 10.7 mM^{-1}, which is in the range of the K_{eq} derived from substituting kinetic parameters into the modified Haldane expression.

While enzymes do not affect the position of the reaction equilibrium, a large K_{eq} highlights the role of the enzyme in accelerating the reverse reaction, as the analogous reaction without enzyme is not favored to occur. The measured K_m for GS-nonenal in the GSTA4-4-catalyzed *retro* Michael reaction is 19 μM, which is ~10x and ~30x lower than the measured K_m values for nonenal and GSH, respectively, suggesting that the moderate catalytic efficiency of the *retro* Michael addition is primarily driven by the low K_m for the GS-nonenal product. The low K_m reflects a tight binding affinity for the product if the reaction mechanism follows a simple model where substrate binding and product release are fast relative to the catalytic step. A similar comparison of the kinetic constants could not be completed with GSTA1-1 due to difficulties in obtaining K_m and k_{cat} values for the reverse reaction. Based on a comparison of H/D exchange of nonenal and GS-nonenal formation that revealed a larger discrepancy between the initial velocity of product formation and the rate of H/D exchange with GSTA1-1, it is expected that the difference in k_{cat}/K_m values of the forward and reverse reactions is even larger than the corresponding difference for GSTA4-4. Accurate determination of kinetic constants is a concern for GSTA1-1 since the enzyme is slow at catalyzing both the forward and reverse reactions with nonenal. Nevertheless, we suggest here that the 'gap' between the forward and reverse reactions is larger for GSTA1-1 than for GSTA4-4 resulting in GSTA4-4 being more reversible than GSTA1-1.

The ability to catalyze the reverse reaction may be advantageous to a regulatory enzyme as it provides a potential pathway for controlling substrate levels. A regulatory role is tied to specificity because efficient regulation necessitates that the enzyme is specific for the substrates

it regulates. By contrast, reversibility provides no advantage to a promiscuous enzyme like GSTA1-1 that has evolved to optimize detoxification of substrates in one direction.

Lastly, the precise mechanism of H/D exchange at C2 of nonenal remains to be resolved. Had H/D exchange been faster than product formation, it would result from reversible GSH conjugation prior to product being released from the active site. However, this is not the case. Measuring the rate of d2-nonenal formation starting from d2-GS-nonenal (instead of nonenal) would provide direct insight into the contribution of the reverse reaction to H/D exchange, although it would be challenging to match the amount of d2-GS-nonenal that is formed in the forward direction.

4.5 FIGURES

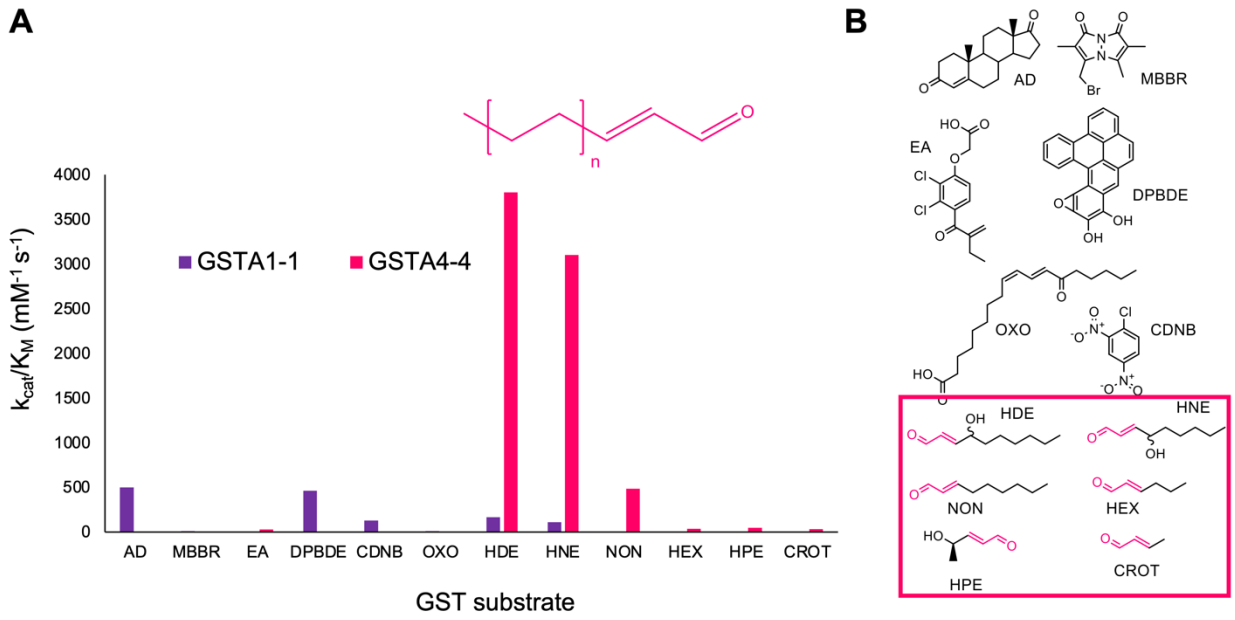

Figure 4.5.1. GSTA4-4 is selective towards lipid alkenal compounds. A) Catalytic efficiency (k_{cat}/K_m) of GSTA1-1 and GSTA4-4 for a range of GST substrates considered in [11]. B) Chemicals structures of GST substrates in A. Substrates containing the lipid alkenal moiety are highlighted in the pink box.

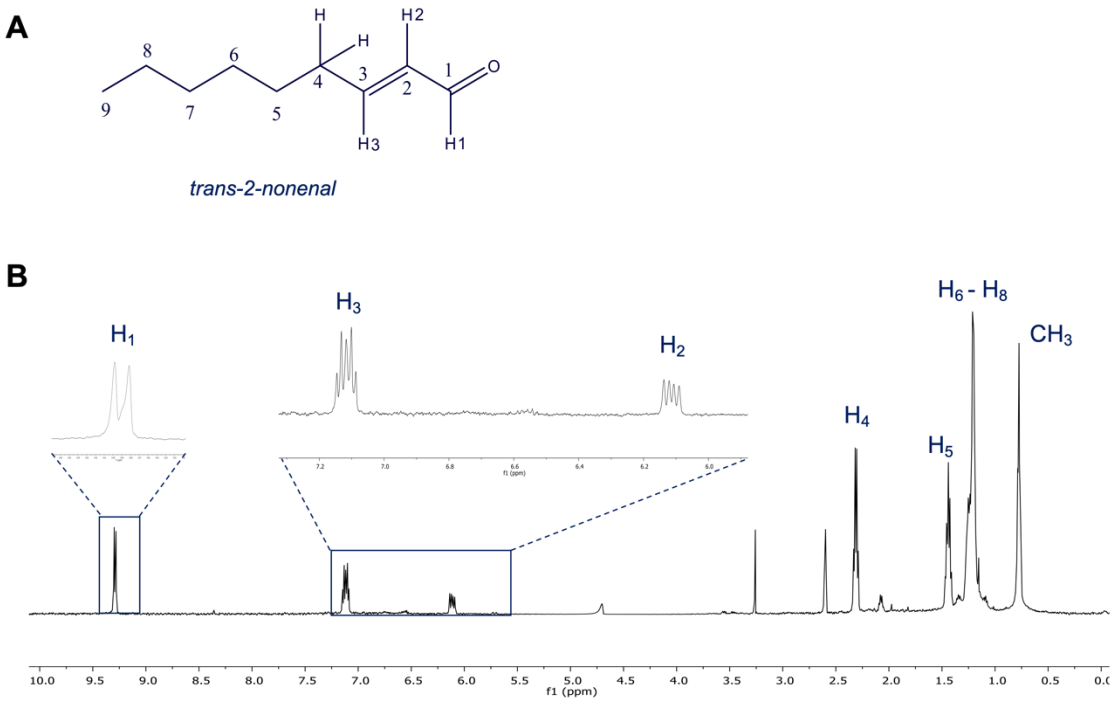

Figure 4.5.2. 1D NMR spectrum of trans-2-nonenal.

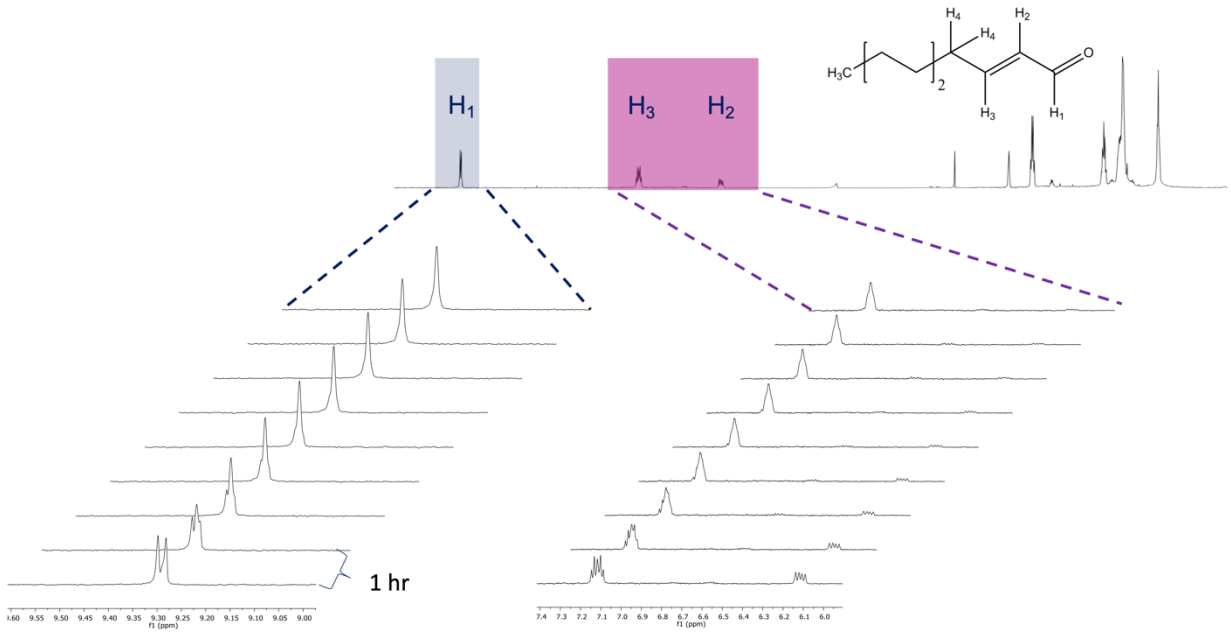

Figure 4.5.3. NMR spectral changes during H/D exchange at C2 of nonenal.

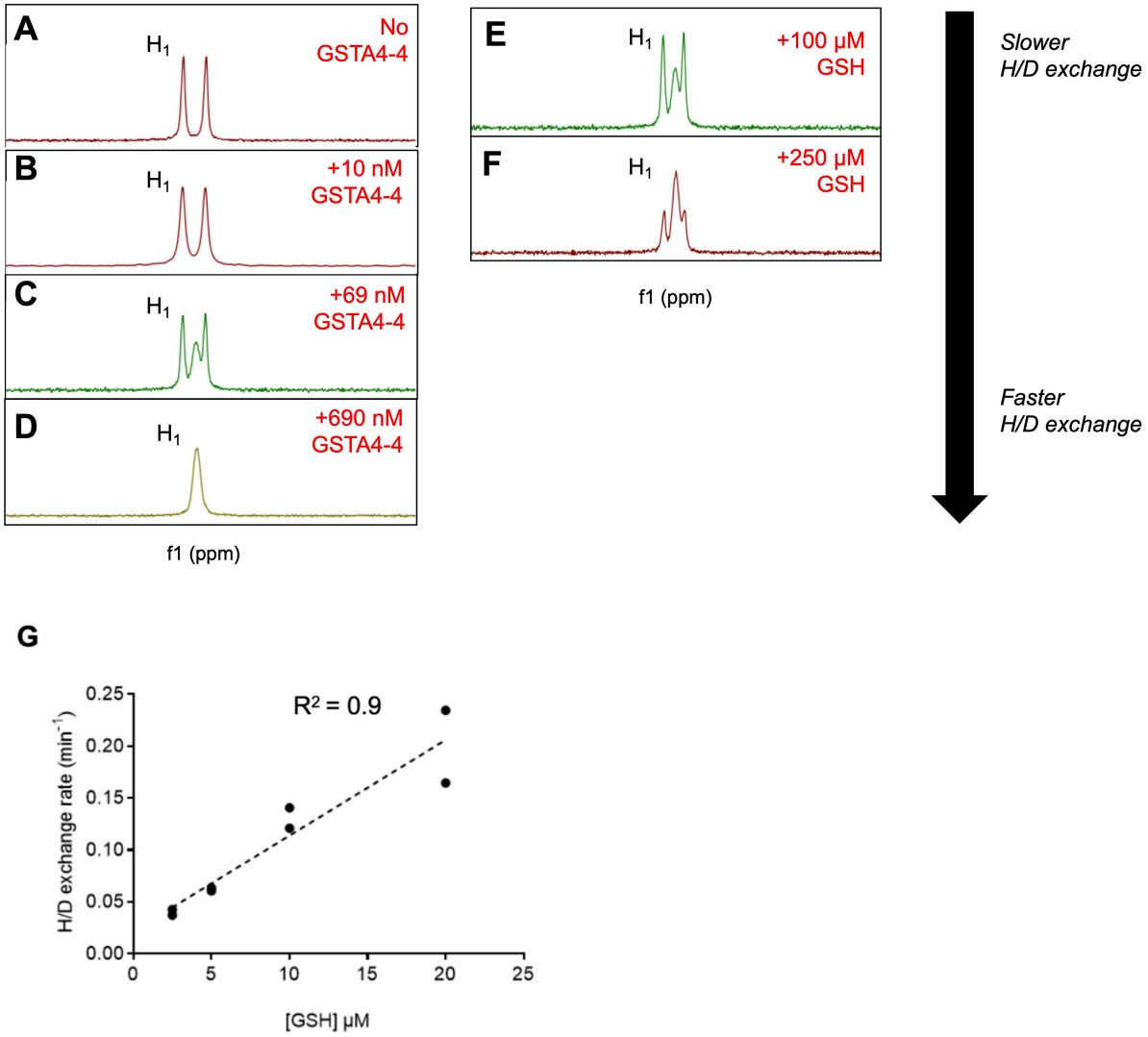

Figure 4.5.4. H/D exchange of nonenal is GSH and GST dependent. A-D) NMR spectra featuring the aldehydic proton H1 of 1 mM nonenal incubated with 100 µM GSH and an increasing concentration of GSTA4-4. **E-F)** NMR spectra of 1 mM nonenal incubated with 69 nM GSTA4-4 in the presence of 100 µM or 250 µM GSH, respectively. **G)** GSH dependence of H/D exchange measured at 2.5, 5, 10, and 20 µM GSH as described in Methods.

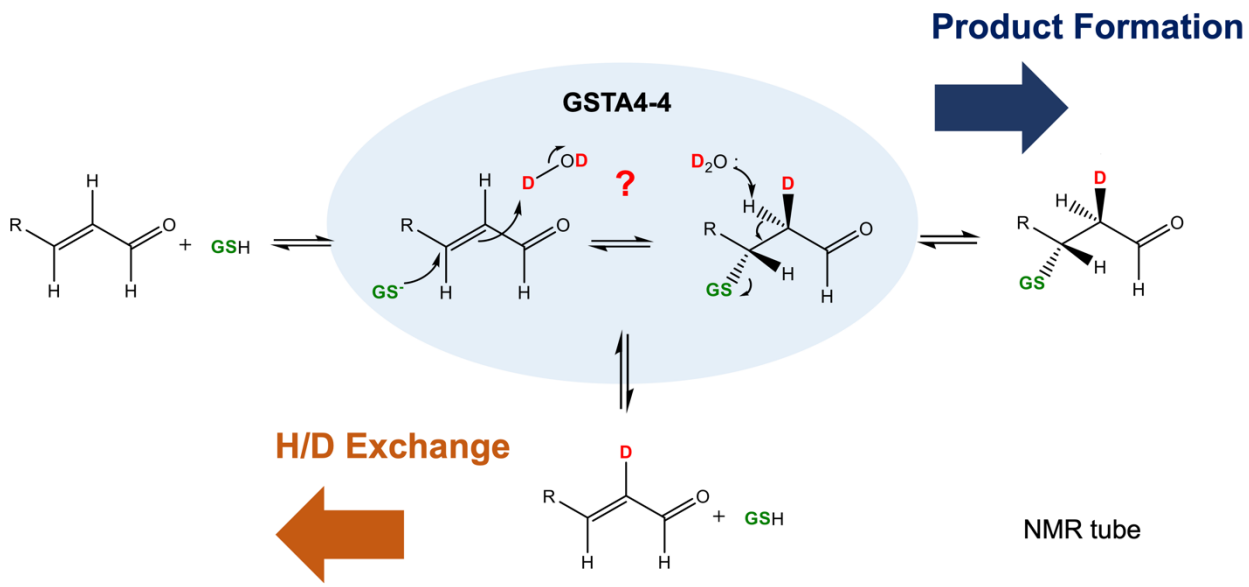

Figure 4.5.5. Schematic representation of H/D exchange and product formation in deuterated solvent.

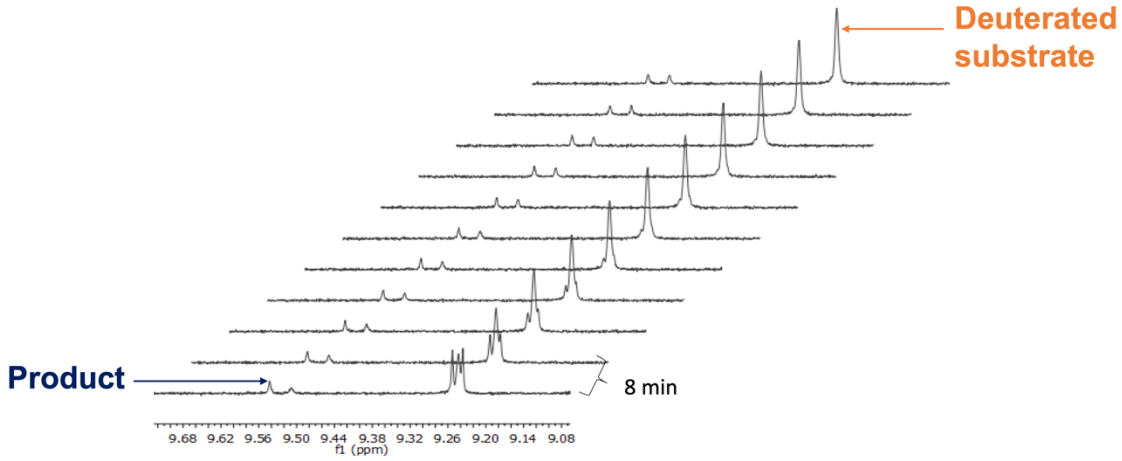

Figure 4.5.6. Product formation appears faster than H/D exchange. NMR spectra of 1 mM nonenal incubated with 69 nM GSTA4-4 and 250 μM GSH featuring the spectral changes at H1 of nonenal (substrate) and GS-nonenal (product).

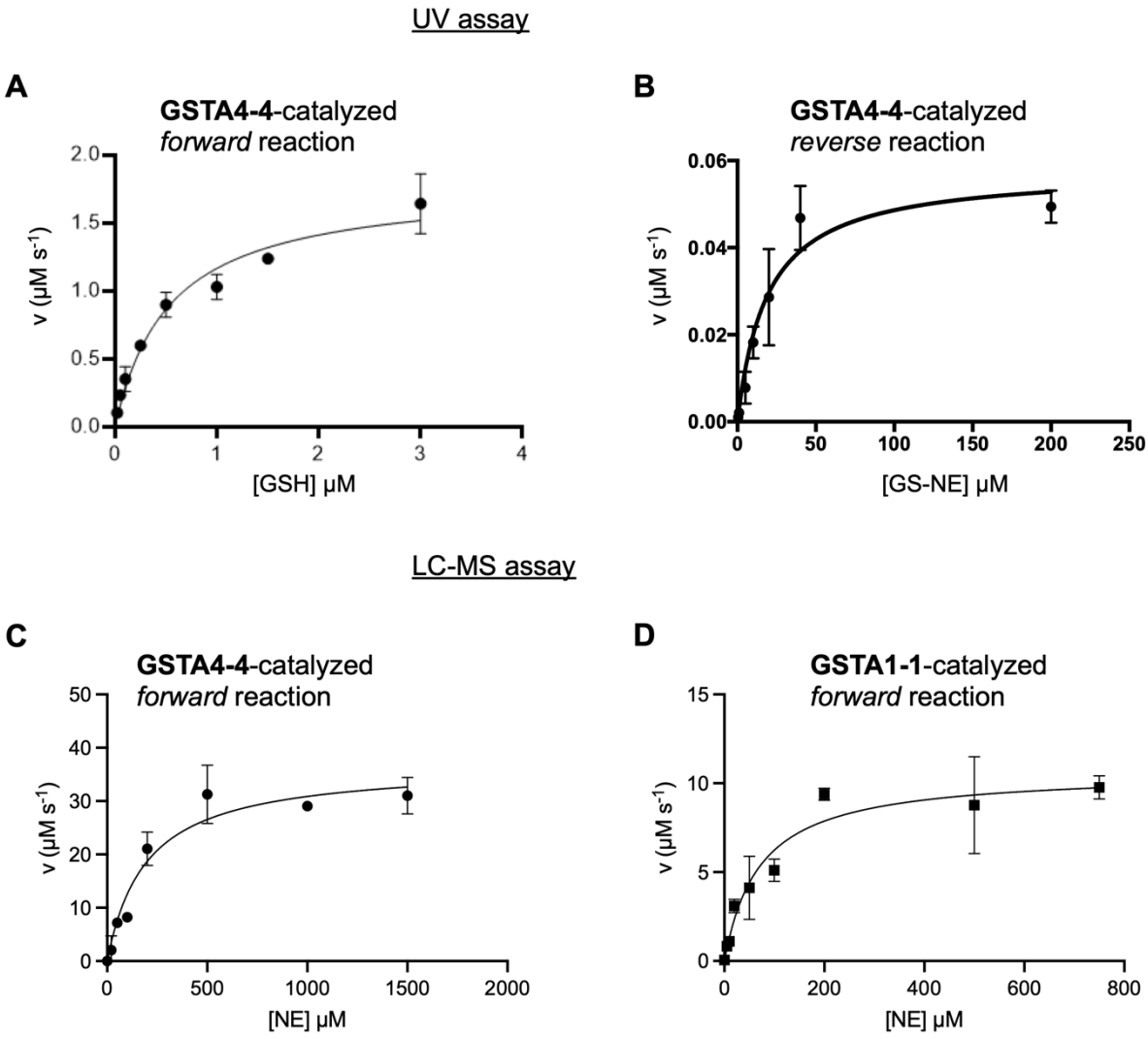

Figure 4.5.7. Steady state kinetics of GSTA1-1 and GSTA4-4 catalyzed reactions.

4.6 TABLES

Table 4.6.1. Summary of NMR spectral changes during H/D exchange and product formation at key protons of nonenal.

	H/D exchange		Product formation	
H1	d (9.2ppm)	s (9.2ppm)	d (9.2ppm)	Pair of s (9.5ppm)
H2	d of d (6.2ppm)	x	d of d (6.2ppm)	Pair of d (2.5ppm)
H3	q (7.1ppm)	Broad s (7.1ppm)	q (7.1ppm)	multiplet (3.2ppm)

Table 4.6.2. Rate of H/D exchange measured by NMR and normalized *v* of product formation measured by UV in matching conditions.

GSTA isoform	H/D exchange (min^{-1})	GS-NE formation (min^{-1})	*Ratio*
GSTA4-4	0.0102	0.0318	*3.3*
GSTA1-1	0.0017	0.0294	*17.4*

Table 4.6.3. Summary of kinetic constants for GSTA4-4 and GSTA1-1 catalyzed reactions.

GSTA isoform	*Forward reaction*			*Reverse reaction*			*Forward/ Reverse*
	K_m (μM) GSH*, nonenal co-substrate; nonenal**, GSH co-substrate	k_{cat} (s^{-1}) *GSH, nonenal co-substrate; **nonenal, GSH co-substrate	k_{cat}/K_m (μM^{-1} s^{-1}) *GSH, nonenal co-substrate; **nonenal, GSH co-substrate	K_m (μM)	k_{cat} (s^{-1})	k_{cat}/K_m (μM^{-1} s^{-1})	*k_{cat}/K_m ratio*
GSTA4-4 (UV)	530 ± 100*	89 ± 6*	0.17*	19 ± 5	1.2 ± 0.1	0.06	*2.8*
GSTA4-4 (LC-MS)	195 ± 49**	1840 ± 140**	9.5**	*NA*	*NA*	*NA*	*NA*
GSTA1-1 (LC-MS)	71 ± 19	10 ± 0.8	0.15	*NA*	*NA*	*NA*	*NA*

4.7 SUPPORTING FIGURES

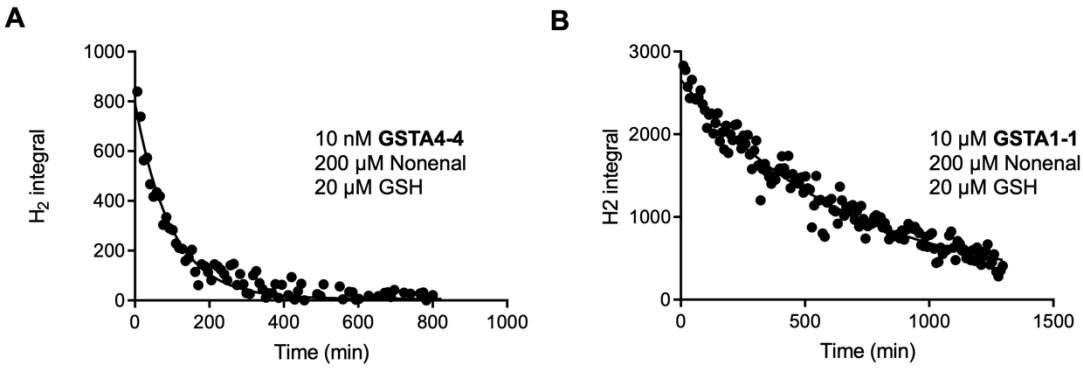

Supporting Figure 4.7.1. H/D exchange of nonenal is slower for GSTA1-1.

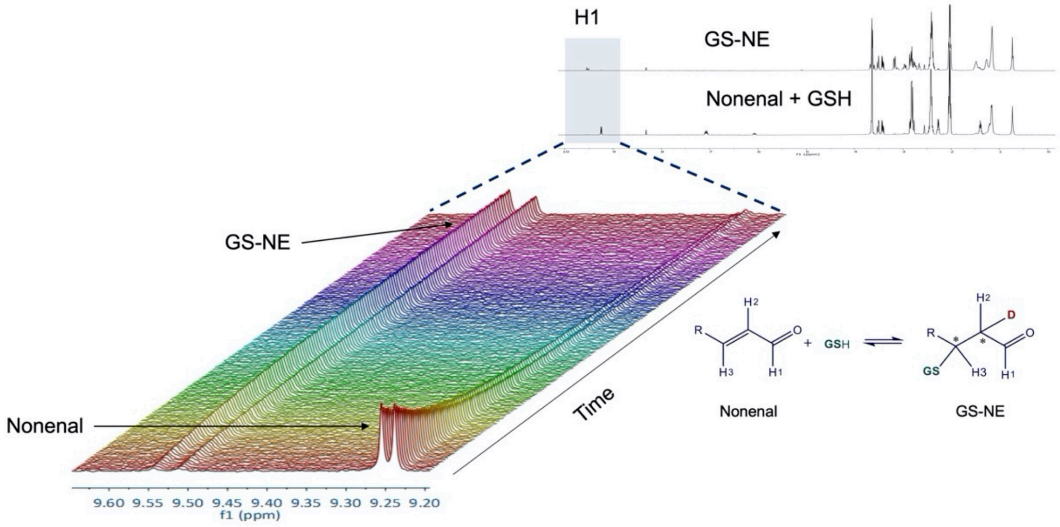

Supporting Figure 4.7.2. GSH and nonenal react spontaneously to form GS-nonenal. NMR spectra of 1mM nonenal incubated with 2.5 mM GSH featuring the spectral changes at H1 of nonenal and GS-nonenal.

BIBLIOGRAPHY

[1] A. Cornish-Bowden, *Fundamentals of Enzyme Kinetics*. John Wiley & Sons, 2013.

[2] O. Khersonsky and D. S. Tawfik, "Enzyme Promiscuity: A Mechanistic and Evolutionary Perspective," *Annu Rev Biochem*, vol. 79, pp. 471–505, 2010, doi: 10.1146/annurev-biochem-030409-143718.

[3] S. D. Copley, "Shining a light on enzyme promiscuity," *Curr. Opin. Struct. Biol.*, vol. 47, pp. 167–175, Dec. 2017, doi: 10.1016/j.sbi.2017.11.001.

[4] T. Zou, V. A. Risso, J. A. Gavira, J. M. Sanchez-Ruiz, and S. B. Ozkan, "Evolution of Conformational Dynamics Determines the Conversion of a Promiscuous Generalist into a Specialist Enzyme," *Mol. Biol. Evol.*, vol. 32, no. 1, pp. 132–143, Jan. 2015, doi: 10.1093/molbev/msu281.

[5] W. M. Atkins, "Biological messiness vs. biological genius: Mechanistic aspects and roles of protein promiscuity," *J. Steroid Biochem. Mol. Biol.*, vol. 151, pp. 3–11, Jul. 2015, doi: 10.1016/j.jsbmb.2014.09.010.

[6] P. J. O'Brien and D. Herschlag, "Catalytic promiscuity and the evolution of new enzymatic activities," *Chem. Biol.*, vol. 6, no. 4, pp. R91–R105, Apr. 1999, doi: 10.1016/S1074-5521(99)80033-7.

[7] C. Pandya, J. D. Farelli, D. Dunaway-Mariano, and K. N. Allen, "Enzyme Promiscuity: Engine of Evolutionary Innovation*," *J. Biol. Chem.*, vol. 289, no. 44, pp. 30229–30236, Oct. 2014, doi: 10.1074/jbc.R114.572990.

[8] "Catalytic Proficiency: The Extreme Case of S–O Cleaving Sulfatases | Journal of the American Chemical Society." https://pubs.acs.org/doi/10.1021/ja208827q (accessed Apr. 11, 2022).

[9] A. Fersht, *Structure and Mechanism in Protein Science: A Guide to Enzyme Catalysis and Protein Folding*. World Scientific, 2017.

[10] K. A. Johnson, "A century of enzyme kinetic analysis, 1913 to 2013," *FEBS Lett.*, vol. 587, pp. 2753–2766, 2013, doi: 10.1016/j.febslet.2013.07.012.

[11] A. Nath and W. M. Atkins, "A Quantitative Index of Substrate Promiscuity," *Biochemistry*, vol. 47, no. 1, pp. 157–166, 2008, doi: 10.1021/bi701448p.

[12] H. Huang *et al.*, "Panoramic view of a superfamily of phosphatases through substrate profiling," *Proc. Natl. Acad. Sci.*, vol. 112, no. 16, pp. E1974–E1983, Apr. 2015, doi: 10.1073/pnas.1423570112.

[13] T. L. Amyes and J. P. Richard, "Specificity in Transition State Binding: The Pauling Model Revisited," *Biochemistry*, vol. 52, no. 12, p. 10.1021/bi301491r, Mar. 2013, doi: 10.1021/bi301491r.

[14] L. Pauling, "Nature of forces between large molecules of biological interest," *Nature*, vol. 161, no. 4097, pp. 707–709, May 1948, doi: 10.1038/161707a0.

[15] D. Herschlag, "The role of induced fit and conformational changes of enzymes in specificity and catalysis," *Bioorganic Chem.*, vol. 16, no. 1, pp. 62–96, Mar. 1988, doi: 10.1016/0045-2068(88)90038-7.

[16] C. B. Post and W. J. Ray, "Reexamination of induced fit as a determinant of substrate specificity in enzymic reactions," *Biochemistry*, vol. 34, no. 49, pp. 15881–15885, Dec. 1995, doi: 10.1021/bi00049a001.

[17] B. Prasad, S. Kamerlin, J. Florián, and A. Warshel, "Prechemistry barriers and checkpoints do not contribute to fidelity and catalysis as long as they are not rate limiting," *Theor. Chem. Acc.*, vol. 131, Dec. 2012, doi: 10.1007/s00214-012-1288-6.

[18] K. A. Johnson, "Role of Induced Fit in Enzyme Specificity: A Molecular Forward/Reverse Switch," *J. Biol. Chem.*, vol. 283, no. 39, pp. 26297–26301, Sep. 2008, doi: 10.1074/jbc.R800034200.

[19] K. A. Johnson, "New standards for collecting and fitting steady state kinetic data," *Beilstein J. Org. Chem.*, vol. 15, pp. 16–29, Jan. 2019, doi: 10.3762/bjoc.15.2.

[20] L. C. James and D. S. Tawfik, "Conformational diversity and protein evolution – a 60-year-old hypothesis revisited," *Trends Biochem. Sci.*, vol. 28, no. 7, pp. 361–368, Jul. 2003, doi: 10.1016/S0968-0004(03)00135-X.

[21] S. J. Benkovic, G. G. Hammes, and S. Hammes-Schiffer, "Free-Energy Landscape of Enzyme Catalysis," *Biochemistry*, vol. 47, no. 11, pp. 3317–3321, Mar. 2008, doi: 10.1021/bi800049z.

[22] P. Chakraborty and E. Di Cera, "Induced Fit Is a Special Case of Conformational Selection," *Biochemistry*, vol. 56, no. 22, pp. 2853–2859, Jun. 2017, doi: 10.1021/acs.biochem.7b00340.

[23] J. B. Stiller, R. Otten, D. Häussinger, P. S. Rieder, D. L. Theobald, and D. Kern, "Structure determination of high-energy states in a dynamic protein ensemble," *Nature*, vol. 603, no. 7901, Art. no. 7901, Mar. 2022, doi: 10.1038/s41586-022-04468-9.

[24] K. A. Henzler-Wildman, M. Lei, V. Thai, S. J. Kerns, M. Karplus, and D. Kern, "A hierarchy of timescales in protein dynamics is linked to enzyme catalysis," *Nature*, vol. 450, no. 7171, Art. no. 7171, Dec. 2007, doi: 10.1038/nature06407.

[25] D. H. Fong and A. M. Berghuis, "Substrate promiscuity of an aminoglycoside antibiotic resistance enzyme via target mimicry," *EMBO J.*, vol. 21, no. 10, pp. 2323–2331, May 2002, doi: 10.1093/emboj/21.10.2323.

[26] J. Skopalík, P. Anzenbacher, and M. Otyepka, "Flexibility of Human Cytochromes P450: Molecular Dynamics Reveals Differences between CYPs 3A4, 2C9, and 2A6, which Correlate with Their Substrate Preferences," *J. Phys. Chem. B*, vol. 112, no. 27, pp. 8165–8173, Jul. 2008, doi: 10.1021/jp800311c.

[27] M. Otyepka, K. Berka, and P. Anzenbacher, "Is there a relationship between the substrate preferences and structural flexibility of cytochromes P450?," *Curr. Drug Metab.*, vol. 13, no. 2, pp. 130–142, Jan. 2012, doi: 10.2174/138920012798918372.

[28] L. Hou *et al.*, "Functional Promiscuity Correlates with Conformational Heterogeneity in A-class Glutathione S-Transferases*," *J. Biol. Chem.*, vol. 282, no. 32, pp. 23264–23274, Aug. 2007, doi: 10.1074/jbc.M700868200.

[29] V. A. Risso, J. A. Gavira, D. F. Mejia-Carmona, E. A. Gaucher, and J. M. Sanchez-Ruiz, "Hyperstability and Substrate Promiscuity in Laboratory Resurrections of Precambrian β-Lactamases," *J. Am. Chem. Soc.*, vol. 135, no. 8, pp. 2899–2902, Feb. 2013, doi: 10.1021/ja311630a.

[30] H. Tao *et al.*, "Molecular insights into the unusually promiscuous and catalytically versatile Fe(II)/α-ketoglutarate-dependent oxygenase SptF," *Nat. Commun.*, vol. 13, no. 1, Art. no. 1, Jan. 2022, doi: 10.1038/s41467-021-27636-3.

[31] J. Luo, B. van Loo, and S. C. L. Kamerlin, "Catalytic promiscuity in Pseudomonas aeruginosa arylsulfatase as an example of chemistry-driven protein evolution," *FEBS Lett.*, vol. 586, no. 11, pp. 1622–1630, 2012, doi: 10.1016/j.febslet.2012.04.012.

[32] M. Gade *et al.*, "Substrate Dynamics Contribute to Enzymatic Specificity in Human and Bacterial Methionine Adenosyltransferases," *JACS Au*, vol. 1, no. 12, pp. 2349–2360, Dec. 2021, doi: 10.1021/jacsau.1c00464.
[33] E. Z. Eisenmesser *et al.*, "Intrinsic dynamics of an enzyme underlies catalysis," *Nature*, vol. 438, no. 7064, Art. no. 7064, Nov. 2005, doi: 10.1038/nature04105.
[34] K. Henzler-Wildman and D. Kern, "Dynamic personalities of proteins," *Nature*, vol. 450, no. 7172, pp. 964–972, Dec. 2007, doi: 10.1038/nature06522.
[35] A. Warshel and R. P. Bora, "Perspective: Defining and quantifying the role of dynamics in enzyme catalysis," *J. Chem. Phys.*, vol. 144, no. 18, p. 180901, May 2016, doi: 10.1063/1.4947037.
[36] R. Nevo, V. Brumfeld, R. Kapon, P. Hinterdorfer, and Z. Reich, "Direct measurement of protein energy landscape roughness," *EMBO Rep.*, vol. 6, no. 5, pp. 482–486, May 2005, doi: 10.1038/sj.embor.7400403.
[37] W. M. Atkins, "Mechanisms of promiscuity among drug metabolizing enzymes and drug transporters," *Febs J.*, vol. 287, no. 7, pp. 1306–1322, Apr. 2020, doi: 10.1111/febs.15116.
[38] N. Tokuriki and D. S. Tawfik, "Protein dynamism and evolvability," *Science*, vol. 324, no. 5924, pp. 203–207, Apr. 2009, doi: 10.1126/science.1169375.
[39] R. A. Jensen, "Enzyme Recruitment in Evolution of New Function," *Annu. Rev. Microbiol.*, vol. 30, no. 1, pp. 409–425, 1976, doi: 10.1146/annurev.mi.30.100176.002205.
[40] N. S. Hatzakis, "Single molecule insights on conformational selection and induced fit mechanism," *Biophys. Chem.*, vol. 186, pp. 46–54, Feb. 2014, doi: 10.1016/j.bpc.2013.11.003.
[41] J. A. Kaczmarski *et al.*, "Altered conformational sampling along an evolutionary trajectory changes the catalytic activity of an enzyme," *Nat. Commun.*, vol. 11, no. 1, Art. no. 1, Nov. 2020, doi: 10.1038/s41467-020-19695-9.
[42] C. M. Miton *et al.*, "Evolutionary repurposing of a sulfatase: A new Michaelis complex leads to efficient transition state charge offset," *Proc. Natl. Acad. Sci. U. S. A.*, vol. 115, no. 31, pp. E7293–E7302, Jul. 2018, doi: 10.1073/pnas.1607817115.
[43] W. B. Jakoby and D. M. Ziegler, "The enzymes of detoxication," *J. Biol. Chem.*, vol. 265, no. 34, pp. 20715–20718, Dec. 1990.
[44] A. Babtie, N. Tokuriki, and F. Hollfelder, "What makes an enzyme promiscuous?," *Curr. Opin. Chem. Biol.*, vol. 14, no. 2, pp. 200–207, Apr. 2010, doi: 10.1016/j.cbpa.2009.11.028.
[45] A. Erijman, Y. Aizner, and J. M. Shifman, "Multispecific Recognition: Mechanism, Evolution, and Design," *Biochemistry*, vol. 50, no. 5, pp. 602–611, Feb. 2011, doi: 10.1021/bi101563v.
[46] K. Bastard *et al.*, "Revealing the hidden functional diversity of an enzyme family," *Nat. Chem. Biol.*, vol. 10, no. 1, Art. no. 1, Jan. 2014, doi: 10.1038/nchembio.1387.
[47] C. Pandya, D. Dunaway-Mariano, Y. Xia, and K. N. Allen, "Structure-guided approach for detecting large domain inserts in protein sequences as illustrated using the haloacid dehalogenase superfamily," *Proteins Struct. Funct. Bioinforma.*, vol. 82, no. 9, pp. 1896–1906, 2014, doi: 10.1002/prot.24543.
[48] J. P. Richard, "Protein Flexibility and Stiffness Enable Efficient Enzymatic Catalysis," *J. Am. Chem. Soc.*, vol. 141, no. 8, pp. 3320–3331, Feb. 2019, doi: 10.1021/jacs.8b10836.

[49] D. Thakur and S. B. Pandit, “Unusual commonality in active site structural features of substrate promiscuous and specialist enzymes,” *J. Struct. Biol.*, vol. 214, no. 1, p. 107835, Mar. 2022, doi: 10.1016/j.jsb.2022.107835.
[50] I. Nobeli, A. D. Favia, and J. M. Thornton, “Protein promiscuity and its implications for biotechnology,” *Nat. Biotechnol. 2009 272*, vol. 27, no. 2, pp. 157–167, Feb. 2009, doi: 10.1038/nbt1519.
[51] M. M. Hann, A. R. Leach, and G. Harper, “Molecular complexity and its impact on the probability of finding leads for drug discovery,” *J. Chem. Inf. Comput. Sci.*, vol. 41, no. 3, pp. 856–864, Jun. 2001, doi: 10.1021/ci000403i.
[52] A. L. Hopkins, J. S. Mason, and J. P. Overington, “Can we rationally design promiscuous drugs?,” *Curr. Opin. Struct. Biol.*, vol. 16, no. 1, pp. 127–136, Feb. 2006, doi: 10.1016/j.sbi.2006.01.013.
[53] M. L. Radhakrishnan and B. Tidor, “Specificity in Molecular Design: A Physical Framework for Probing the Determinants of Binding Specificity and Promiscuity in a Biological Environment,” *J. Phys. Chem. B*, vol. 111, no. 47, pp. 13419–13435, Nov. 2007, doi: 10.1021/jp074285e.
[54] “Conformational analysis of drug-like molecules bound to proteins: an extensive study of ligand reorganization upon binding - PubMed.” https://pubmed.ncbi.nlm.nih.gov/15115393/ (accessed Apr. 17, 2022).
[55] E. Gilberg, M. Gütschow, and J. Bajorath, “Promiscuous Ligands from Experimentally Determined Structures, Binding Conformations, and Protein Family-Dependent Interaction Hotspots,” *ACS Omega*, vol. 4, no. 1, pp. 1729–1737, Jan. 2019, doi: 10.1021/acsomega.8b03481.
[56] V. J. Haupt, S. Daminelli, and M. Schroeder, “Drug promiscuity in PDB: protein binding site similarity is key,” *PLoS One*, p. 65894, 2013.
[57] “Mapping the Limits of Substrate Specificity of the Adenylation Domain of TycA - Villiers - 2009 - ChemBioChem - Wiley Online Library.” https://chemistry-europe.onlinelibrary.wiley.com/doi/10.1002/cbic.200800553 (accessed Apr. 15, 2022).
[58] L. Afriat, C. Roodveldt, G. Manco, and D. S. Tawfik, “The Latent Promiscuity of Newly Identified Microbial Lactonases Is Linked to a Recently Diverged Phosphotriesterase,” *Biochemistry*, vol. 45, no. 46, pp. 13677–13686, Nov. 2006, doi: 10.1021/bi061268r.
[59] O. Khersonsky and D. S. Tawfik, “Structure−Reactivity Studies of Serum Paraoxonase PON1 Suggest that Its Native Activity Is Lactonase,” *Biochemistry*, vol. 44, no. 16, pp. 6371–6382, Apr. 2005, doi: 10.1021/bi047440d.
[60] P. D. Montellano, *Cytochrome P450: structure, mechanism, and biochemistry*. 2005. Accessed: Jun. 03, 2019. [Online]. Available: https://books.google.com/books?hl=en&lr=&id=W5_OPK6tFdYC&oi=fnd&pg=PR19&ots=PUMAuzCy4r&sig=b74Qbo4_T9GCv8uH0jxf-fx9J9c
[61] D. R. Nelson, “Cytochrome P450 diversity in the tree of life,” *Biochim. Biophys. Acta - Proteins Proteomics*, vol. 1866, no. 1, pp. 141–154, Jan. 2018, doi: 10.1016/J.BBAPAP.2017.05.003.
[62] P. R. Ortiz de Montellano, Ed., *Cytochrome P450*. Cham: Springer International Publishing, 2015. doi: 10.1007/978-3-319-12108-6.
[63] I. G. Denisov, A. Y. Shih, and S. G. Sligar, “Structural differences between soluble and membrane bound cytochrome P450s,” *J. Inorg. Biochem.*, vol. 108, pp. 150–158, Mar. 2012, doi: 10.1016/j.jinorgbio.2011.11.026.

[64] O. Gotoh, “Substrate recognition sites in cytochrome P450 family 2 (CYP2) proteins inferred from comparative analyses of amino acid and coding nucleotide sequences.,” *J. Biol. Chem.*, vol. 267, no. 1, pp. 83–90, Jan. 1992, doi: 10.1016/S0021-9258(18)48462-1.

[65] T. C. Pochapsky, S. Kazanis, and M. Dang, “Conformational plasticity and structure/function relationships in cytochromes P450,” *Antioxid. Redox Signal.*, vol. 13, no. 8, pp. 1273–1296, Oct. 2010, doi: 10.1089/ARS.2010.3109.

[66] I. F. Sevrioukova and T. L. Poulos, “Structural basis for regiospecific midazolam oxidation by human cytochrome P450 3A4,” *Proc. Natl. Acad. Sci. U. S. A.*, vol. 114, no. 3, pp. 486–491, Jan. 2017, doi: 10.1073/pnas.1616198114.

[67] Y. Zhao, M. A. White, B. K. Muralidhara, L. Sun, J. R. Halpert, and C. D. Stout, “Structure of microsomal cytochrome P450 2B4 complexed with the antifungal drug bifonazole: insight into P450 conformational plasticity and membrane interaction,” *J. Biol. Chem.*, vol. 281, no. 9, pp. 5973–5981, Mar. 2006, doi: 10.1074/JBC.M511464200.

[68] T. Hendrychová *et al.*, “Flexibility of human cytochrome P450 enzymes: Molecular dynamics and spectroscopy reveal important function-related variations,” *Biochim. Biophys. Acta - Proteins Proteomics*, vol. 1814, no. 1, pp. 58–68, Jan. 2011, doi: 10.1016/j.bbapap.2010.07.017.

[69] D. F. Estrada, A. Kumar, C. S. Campomizzi, and N. Jay, “Crystal Structures of Drug-Metabolizing CYPs,” *Methods Mol. Biol.*, vol. 2342, pp. 171–192, 2021, doi: 10.1007/978-1-0716-1554-6_7.

[70] S. Stoll, Y.-T. Lee, M. Zhang, R. F. Wilson, R. D. Britt, and D. B. Goodin, “Double electron-electron resonance shows cytochrome P450cam undergoes a conformational change in solution upon binding substrate,” *Proc. Natl. Acad. Sci. U. S. A.*, vol. 109, no. 32, pp. 12888–12893, Aug. 2012, doi: 10.1073/pnas.1207123109.

[71] M. D. Paulsen and R. L. Ornstein, “Dramatic differences in the motions of the mouth of open and closed cytochrome P450BM-3 by molecular dynamics simulations,” *Proteins*, vol. 21, no. 3, pp. 237–243, Mar. 1995, doi: 10.1002/prot.340210306.

[72] D. Basudhar, Y. Madrona, S. Kandel, J. N. Lampe, C. R. Nishida, and P. R. Ortiz De Montellano, “Analysis of cytochrome P450 CYP119 ligand-dependent conformational dynamics by two-dimensional NMR and X-ray crystallography,” *J. Biol. Chem.*, vol. 290, no. 16, pp. 10000–10017, Apr. 2015, doi: 10.1074/JBC.M114.627935.

[73] T. Y. Hargrove *et al.*, “Binding of a physiological substrate causes large-scale conformational reorganization in cytochrome P450 51,” *J. Biol. Chem.*, vol. 293, no. 50, pp. 19344–19353, Dec. 2018, doi: 10.1074/JBC.RA118.005850.

[74] H. Li and T. L. Poulos, “The structure of the cytochrome p450BM-3 haem domain complexed with the fatty acid substrate, palmitoleic acid,” *Nat. Struct. Biol.*, vol. 4, no. 2, Art. no. 2, Feb. 1997, doi: 10.1038/nsb0297-140.

[75] K. D. Dubey, B. Wang, and S. Shaik, “Molecular Dynamics and QM/MM Calculations Predict the Substrate-Induced Gating of Cytochrome P450 BM3 and the Regio- and Stereoselectivity of Fatty Acid Hydroxylation,” *J. Am. Chem. Soc.*, vol. 138, no. 3, pp. 837–845, Jan. 2016, doi: 10.1021/jacs.5b08737.

[76] B. C. Monk *et al.*, “Architecture of a single membrane spanning cytochrome P450 suggests constraints that orient the catalytic domain relative to a bilayer”, doi: 10.1073/pnas.1324245111.

[77] J. Li, Y. Chen, Y. Tang, W. Li, and Y. Tu, “Homotropic Cooperativity of Midazolam Metabolism by Cytochrome P450 3A4: Insight from Computational Studies,” *J. Chem. Inf. Model.*, vol. 61, no. 5, pp. 2418–2426, May 2021, doi: 10.1021/acs.jcim.1c00266.

[78] M. Redhair, J. C. Hackett, R. D. Pelletier, and W. M. Atkins, “Dynamics and Location of the Allosteric Midazolam Site in Cytochrome P4503A4 in Lipid Nanodiscs,” *Biochemistry*, vol. 59, no. 6, pp. 766–779, Feb. 2020, doi: 10.1021/acs.biochem.9b01001.

[79] X. Yu, V. Cojocaru, and R. C. Wade, “Conformational diversity and ligand tunnels of mammalian cytochrome P450s,” *Biotechnol. Appl. Biochem.*, vol. 60, no. 1, pp. 134–145, Feb. 2013, doi: 10.1002/BAB.1074.

[80] M. Šrejber *et al.*, “Membrane-attached mammalian cytochromes P450: An overview of the membrane’s effects on structure, drug binding, and interactions with redox partners,” *J. Inorg. Biochem.*, vol. 183, pp. 117–136, Jun. 2018, doi: 10.1016/j.jinorgbio.2018.03.002.

[81] A. Sündermann and C. Oostenbrink, “Molecular dynamics simulations give insight into the conformational change, complex formation, and electron transfer pathway for cytochrome P450 reductase,” *Protein Sci. Publ. Protein Soc.*, vol. 22, no. 9, pp. 1183–1195, Sep. 2013, doi: 10.1002/PRO.2307.

[82] P. C. Nair, R. A. McKinnon, and J. O. Miners, “Cytochrome P450 structure–function: insights from molecular dynamics simulations,” *Drug Metab. Rev.*, vol. 48, no. 3, pp. 434–452, Jul. 2016, doi: 10.1080/03602532.2016.1178771.

[83] X. Yu, V. Cojocaru, and R. C. Wade, “Conformational diversity and ligand tunnels of mammalian cytochrome P450s,” *Biotechnol. Appl. Biochem.*, vol. 60, no. 1, pp. 134–145, Feb. 2013, doi: 10.1002/bab.1074.

[84] M. Paloncýová, V. Navrátilová, K. Berka, A. Laio, and M. Otyepka, “Role of Enzyme Flexibility in Ligand Access and Egress to Active Site: Bias-Exchange Metadynamics Study of 1,3,7-Trimethyluric Acid in Cytochrome P450 3A4,” *J. Chem. Theory Comput.*, vol. 12, no. 4, pp. 2101–2109, Apr. 2016, doi: 10.1021/ACS.JCTC.6B00075/SUPPL_FILE/CT6B00075_SI_002.ZIP.

[85] * Hwangseo Park, * and Sangyoub Lee, and J. Suh, “Structural and Dynamical Basis of Broad Substrate Specificity, Catalytic Mechanism, and Inhibition of Cytochrome P450 3A4,” 2005, doi: 10.1021/JA053809Q.

[86] J. Liu, G. J. Tawa, and A. Wallqvist, “Identifying cytochrome P450 functional networks and their allosteric regulatory elements,” *PLoS ONE*, vol. 8, no. 12, Dec. 2013, doi: 10.1371/journal.pone.0081980.

[87] D. Fishelovitch, C. Hazan, H. Hirao, H. J. Wolfson, R. Nussinov, and S. Shaik, “QM/MM study of the active species of the human cytochrome P450 3A4, and the influence thereof of the multiple substrate binding.,” *J. Phys. Chem. B*, vol. 111, no. 49, pp. 13822–32, Dec. 2007, doi: 10.1021/jp076401j.

[88] D. Fishelovitch, S. Shaik, H. J. Wolfson, and R. Nussinov, “How does the reductase help to regulate the catalytic cycle of cytochrome P450 3A4 using the conserved water channel?,” *J. Phys. Chem. B*, vol. 114, no. 17, pp. 5964–70, May 2010, doi: 10.1021/jp101894k.

[89] D. Fishelovitch, S. Shaik, H. J. Wolfson, and R. Nussinov, “Theoretical characterization of substrate access/exit channels in the human cytochrome P450 3A4 enzyme: involvement of phenylalanine residues in the gating mechanism.,” *J. Phys. Chem. B*, vol. 113, no. 39, pp. 13018–25, Oct. 2009, doi: 10.1021/jp810386z.

[90] D. R. Davydov, J. R. Halpert, J. P. Renaud, and G. Hui Bon Hoa, “Conformational heterogeneity of cytochrome P450 3A4 revealed by high pressure spectroscopy,” *Biochem. Biophys. Res. Commun.*, vol. 312, no. 1, pp. 121–130, 2003, doi: 10.1016/j.bbrc.2003.09.247.

[91] D. R. Davydov, J. A. O. Rumfeldt, E. V. Sineva, H. Fernando, N. Y. Davydova, and J. R. Halpert, “Peripheral Ligand-binding Site in Cytochrome P450 3A4 Located with Fluorescence Resonance Energy Transfer (FRET),” *J. Biol. Chem.*, vol. 287, no. 9, pp. 6797–6809, Feb. 2012, doi: 10.1074/jbc.M111.325654.

[92] G. I. Lepesheva, M. Seliskar, C. G. Knutson, N. V. Stourman, D. Rozman, and M. R. Waterman, “Conformational dynamics in the F/G segment of CYP51 from Mycobacterium tuberculosis monitored by FRET,” *Arch. Biochem. Biophys.*, vol. 464, no. 2, pp. 221–227, Aug. 2007, doi: 10.1016/J.ABB.2007.05.017.

[93] G. Di Nardo *et al.*, “Dynamics and flexibility of human aromatase probed by FTIR and time resolved fluorescence spectroscopy,” *PloS One*, vol. 8, no. 12, p. e82118, 2013, doi: 10.1371/journal.pone.0082118.

[94] A. Nath, P. K. Koo, E. Rhoades, and W. M. Atkins, “Allosteric effects on substrate dissociation from cytochrome P450 3A4 in nanodiscs observed by ensemble and single-molecule fluorescence spectroscopy,” *J. Am. Chem. Soc.*, vol. 130, no. 47, pp. 15746–15747, 2008, doi: 10.1021/ja805772r.

[95] D. F. Estrada, J. S. Laurence, and E. E. Scott, “Substrate-modulated cytochrome P450 17A1 and cytochrome b5 interactions revealed by NMR,” *J. Biol. Chem.*, vol. 288, no. 23, pp. 17008–17018, Jun. 2013, doi: 10.1074/jbc.M113.468926.

[96] M. Zhang *et al.*, “Reconstitution of the Cytb5–CytP450 Complex in Nanodiscs for Structural Studies using NMR Spectroscopy,” *Angew. Chem. Int. Ed.*, vol. 55, no. 14, pp. 4497–4499, 2016, doi: 10.1002/anie.201600073.

[97] K. P. Ravindranathan, E. Gallicchio, A. E. McDermott, and R. M. Levy, “Conformational Dynamics of Substrate in the Active Site of Cytochrome P450 BM-3/NPG Complex: Insights from NMR Order Parameters,” *J. Am. Chem. Soc.*, vol. 129, no. 3, pp. 474–475, Jan. 2007, doi: 10.1021/ja0672371.

[98] B. Krishnarjuna, T. Yamazaki, G. M. Anantharamaiah, and A. Ramamoorthy, “Nanodisc reconstitution of flavin mononucleotide binding domain of cytochrome-P450-reductase enables high-resolution NMR probing,” *Chem. Commun.*, vol. 57, no. 39, pp. 4819–4822, May 2021, doi: 10.1039/d1cc01018b.

[99] T. C. Pochapsky, “A dynamic understanding of cytochrome P450 structure and function through solution NMR,” *Curr. Opin. Biotechnol.*, vol. 69, pp. 35–42, Jun. 2021, doi: 10.1016/j.copbio.2020.11.007.

[100] A. G. Roberts *et al.*, “NMR Studies of Ligand Binding to P450 eryF Provides Insight into the Mechanism of,” *Society*, no. 8, pp. 1673–1684, 2006.

[101] L. N. Jeffreys *et al.*, “Characterization of the structure and interactions of P450 BM3 using hybrid mass spectrometry approaches,” *J. Biol. Chem.*, vol. 295, no. 22, pp. 7595–7607, May 2020, doi: 10.1074/JBC.RA119.011630.

[102] N. A. Treuheit *et al.*, “Membrane Interactions, Ligand-Dependent Dynamics, and Stability of Cytochrome P4503A4 in Lipid Nanodiscs,” *Biochemistry*, vol. 55, no. 7, pp. 1058–1069, Feb. 2016, doi: 10.1021/acs.biochem.5b01313.

[103] L. Paço, F. Zarate-Perez, A. F. Clouser, W. M. Atkins, and J. C. Hackett, “Dynamics and Mechanism of Binding of Androstenedione to Membrane-Associated Aromatase,”

Biochemistry, vol. 59, no. 33, pp. 2999–3009, Aug. 2020, doi: 10.1021/acs.biochem.0c00460.

[104] K. W. Anderson, N. Mast, J. W. Hudgens, J. B. Lin, I. V. Turko, and I. A. Pikuleva, "Allosteric site in CYP46A1 Cholesterol Hydroxylase CYP46A1: Mapping of the Allosteric Site for Efavirenz, a Drug that Stimulates Enzyme Activity," 2016, doi: 10.1074/jbc.M116.723577.

[105] J. Ducharme, I. F. Sevrioukova, C. J. Thibodeaux, and K. Auclair, "Structural Dynamics of Cytochrome P450 3A4 in the Presence of Substrates and Cytochrome P450 Reductase," *Biochemistry*, vol. 60, no. 28, pp. 2259–2271, Jul. 2021, doi: 10.1021/ACS.BIOCHEM.1C00178.

[106] A. H. Follmer, S. Tripathi, and T. L. Poulos, "Ligand and Redox Partner Binding Generates a New Conformational State in Cytochrome P450cam (CYP101A1)," *J. Am. Chem. Soc.*, 2019, doi: 10.1021/jacs.8b13079.

[107] Y.-T. Lee, E. C. Glazer, R. F. Wilson, C. D. Stout, and D. B. Goodin, "Three clusters of conformational states in p450cam reveal a multistep pathway for closing of the substrate access channel," *Biochemistry*, vol. 50, no. 5, pp. 693–703, Feb. 2011, doi: 10.1021/bi101726d.

[108] T. L. Poulos, B. C. Finzel, and A. J. Howard, "High-resolution crystal structure of cytochrome P450cam," *J. Mol. Biol.*, vol. 195, no. 3, pp. 687–700, Jun. 1987, doi: 10.1016/0022-2836(87)90190-2.

[109] T. L. Poulos, B. C. Finzel, and A. J. Howard, "Crystal structure of substrate-free Pseudomonas putida cytochrome P-450," *Biochemistry*, vol. 25, no. 18, pp. 5314–5322, Sep. 1986, doi: 10.1021/bi00366a049.

[110] T. L. Poulos, B. C. Finzel, I. C. Gunsalus, G. C. Wagner, and J. Kraut, "The 2.6-A crystal structure of Pseudomonas putida cytochrome P-450," *J. Biol. Chem.*, vol. 260, no. 30, pp. 16122–16130, Dec. 1985.

[111] L. Banci, I. Bertini, L. D. Eltis, and R. Pierattelli, "Spectroscopic characterization of a newly isolated cytochrome P450 from Rhodococcus rhodochrous," *Biophys. J.*, vol. 65, no. 2, pp. 806–813, Aug. 1993, doi: 10.1016/S0006-3495(93)81122-6.

[112] L. Banci, I. Bertini, S. Marconi, R. Pierattelli, and S. G. Sligar, "Cytochrome P450 and Aromatic Bases: A 1H NMR Study," *ACS Publications*, May 01, 2002. https://pubs.acs.org/doi/pdf/10.1021/ja00090a035 (accessed May 09, 2022).

[113] E. K. Asciutto and T. C. Pochapsky, "Some Surprising Implications of NMR-directed Simulations of Substrate Recognition and Binding by Cytochrome P450cam (CYP101A1)," *J. Mol. Biol.*, vol. 430, no. 9, pp. 1295–1310, Apr. 2018, doi: 10.1016/j.jmb.2018.03.014.

[114] A. M. Colthart, D. R. Tietz, Y. Ni, J. L. Friedman, M. Dang, and T. C. Pochapsky, "Detection of substrate-dependent conformational changes in the P450 fold by nuclear magnetic resonance," *Sci. Rep.*, vol. 6, Feb. 2016, doi: 10.1038/SREP22035.

[115] M. Dang, S. S. Pochapsky, and T. C. Pochapsky, "Spring-loading the active site of cytochrome P450cam," *Met. Integr. Biometal Sci.*, vol. 3, no. 4, p. 339, Apr. 2011, doi: 10.1039/C0MT00065E.

[116] B. OuYang, S. S. Pochapsky, M. Dang, and T. C. Pochapsky, "A Functional Proline Switch in Cytochrome P450cam," *Structure*, vol. 16, no. 6, pp. 916–923, Jun. 2008, doi: 10.1016/J.STR.2008.03.011.

[117] S. S. Pochapsky, T. C. Pochapsky, and J. W. Wei, “A model for effector activity in a highly specific biological electron transfer complex: the cytochrome P450(cam)-putidaredoxin couple,” *Biochemistry*, vol. 42, no. 19, pp. 5649–5656, May 2003, doi: 10.1021/bi034263s.

[118] S. P. Skinner, A. H. Follmer, M. Ubbink, T. L. Poulos, J. J. Houwing-Duistermaat, and E. Paci, “Partial Opening of Cytochrome P450cam (CYP101A1) Is Driven by Allostery and Putidaredoxin Binding,” *Biochemistry*, vol. 60, no. 39, pp. 2932–2942, Oct. 2021, doi: 10.1021/acs.biochem.1c00406.

[119] Y.-T. Lee, R. F. Wilson, I. Rupniewski, and D. B. Goodin, “P450cam visits an open conformation in the absence of substrate,” *Biochemistry*, vol. 49, no. 16, pp. 3412–3419, Apr. 2010, doi: 10.1021/bi100183g.

[120] S.-W. Chuo, L.-P. Wang, R. D. Britt, and D. B. Goodin, “An Intermediate Conformational State of Cytochrome P450cam-CN in Complex with Putidaredoxin,” *Biochemistry*, vol. 58, no. 18, pp. 2353–2361, May 2019, doi: 10.1021/acs.biochem.9b00192.

[121] D. F. Estrada, A. L. Skinner, J. S. Laurence, and E. E. Scott, “Human cytochrome P450 17A1 conformational selection: Modulation by ligand and cytochrome b5,” *J. Biol. Chem.*, vol. 289, no. 20, pp. 14310–14320, May 2014, doi: 10.1074/jbc.M114.560144.

[122] W. Zhang, S. S. Pochapsky, T. C. Pochapsky, and N. U. Jain, “Solution NMR Structure of Putidaredoxin–Cytochrome P450cam Complex via a Combined Residual Dipolar Coupling–Spin Labeling Approach Suggests a Role for Trp106 of Putidaredoxin in Complex Formation,” *J. Mol. Biol.*, vol. 384, no. 2, pp. 349–363, Dec. 2008, doi: 10.1016/j.jmb.2008.09.037.

[123] E. Anzenbacherová *et al.*, “Flexibility and stability of the structure of cytochromes P450 3A4 and BM-3,” *Eur. J. Biochem.*, vol. 267, no. 10, pp. 2916–2920, May 2000, doi: 10.1046/J.1432-1327.2000.01305.X.

[124] T. Hendrychova, K. Berka, V. Navratilova, P. Anzenbacher, and M. Otyepka, “Dynamics and hydration of the active sites of mammalian cytochromes P450 probed by molecular dynamics simulations,” *Curr. Drug Metab.*, vol. 13, no. 2, pp. 177–189, Feb. 2012, doi: 10.2174/138920012798918408.

[125] Y. Hamuro, K. S. Molnar, S. J. Coales, B. OuYang, A. K. Simorellis, and T. C. Pochapsky, “Hydrogen–deuterium exchange mass spectrometry for investigation of backbone dynamics of oxidized and reduced cytochrome P450cam,” *J. Inorg. Biochem.*, vol. 102, no. 2, pp. 364–370, Feb. 2008, doi: 10.1016/j.jinorgbio.2007.10.001.

[126] P. R. Wilderman *et al.*, “Plasticity of Cytochrome P450 2B4 as Investigated by Hydrogen-Deuterium Exchange Mass Spectrometry and X-ray Crystallography,” *J. Biol. Chem.*, vol. 285, no. 49, p. 38602, Dec. 2010, doi: 10.1074/JBC.M110.180646.

[127] J. L. Baylon, I. L. Lenov, S. G. Sligar, and E. Tajkhorshid, “Characterizing the Membrane-Bound State of Cytochrome P450 3A4: Structure, Depth of Insertion, and Orientation,” 2013, doi: 10.1021/ja4003525.

[128] P. a Williams, “Crystal Structures of Human Cytochrome P450 3A4 Bound to Metyrapone and Progesterone,” *Science*, vol. 305, no. 5684, pp. 683–686, 2004, doi: 10.1126/science.1099736.

[129] M. Ekroos and T. Sjogren, “Structural basis for ligand promiscuity in cytochrome P450 3A4,” *Proc. Natl. Acad. Sci.*, vol. 103, no. 37, pp. 13682–13687, 2006, doi: 10.1073/pnas.0603236103.

[130] I. F. Sevrioukova and T. L. Poulos, “Structure and mechanism of the complex between cytochrome P4503A4 and ritonavir,” *Proc. Natl. Acad. Sci. U. S. A.*, vol. 107, no. 43, pp. 18422–18427, Oct. 2010, doi: 10.1073/PNAS.1010693107.
[131] J. K. Yano, M. R. Wester, G. A. Schoch, K. J. Griffin, C. D. Stout, and E. F. Johnson, “The structure of human microsomal cytochrome P450 3A4 determined by X-ray crystallography to 2.05-A resolution,” *J. Biol. Chem.*, vol. 279, no. 37, pp. 38091–38094, Sep. 2004, doi: 10.1074/JBC.C400293200.
[132] M. J. Dabrowski, M. L. Schrag, L. C. Wienkers, and W. M. Atkins, “Pyrene-pyrene complexes at the active site of cytochrome P450 3A4: evidence for a multiple sustrate binding site,” *J. Am. Chem. Soc.*, vol. 124, pp. 11866–11867, 2002.
[133] W. M. Atkins, “Non-Michaelis-Menten Kinetics in Cytochrome P450-Catalyzed Reactions,” *Annu. Rev. Pharmacol. Toxicol.*, vol. 45, no. 1, pp. 291–310, 2005, doi: 10.1146/annurev.pharmtox.45.120403.100004.
[134] G. A. Schoch, J. K. Yano, S. Sansen, P. M. Dansette, C. D. Stout, and E. F. Johnson, “Determinants of cytochrome P450 2C8 substrate binding: structures of complexes with montelukast, troglitazone, felodipine, and 9-cis-retinoic acid,” *J. Biol. Chem.*, vol. 283, no. 25, pp. 17227–17237, Jun. 2008, doi: 10.1074/JBC.M802180200.
[135] D. Becker, P. V. Bharatam, and H. Gohlke, “F/G Region Rigidity is Inversely Correlated to Substrate Promiscuity of Human CYP Isoforms Involved in Metabolism,” *J. Chem. Inf. Model.*, vol. 61, no. 8, pp. 4023–4030, Aug. 2021, doi: 10.1021/ACS.JCIM.1C00558/SUPPL_FILE/CI1C00558_SI_001.PDF.
[136] D. Ghosh, J. Griswold, M. Erman, and W. Pangborn, “Structural basis for androgen specificity and oestrogen synthesis in human aromatase,” *Nature*, vol. 457, no. 7226, pp. 219–223, 2009, doi: 10.1038/nature07614.
[137] S. E. Bulun, “AROMATASE DEFICIENCY,” *Fertil. Steril.*, vol. 101, no. 2, pp. 323–329, Feb. 2014, doi: 10.1016/j.fertnstert.2013.12.022.
[138] G. D. Nardo *et al.*, “Evidence for an Elevated Aspartate pK a in the Active Site of Human Aromatase *,” 2014, doi: 10.1074/jbc.M114.595108.
[139] D. Ghosh, C. Egbuta, and J. Lo, “Testosterone complex and non-steroidal ligands of human aromatase.,” *J. Steroid Biochem. Mol. Biol.*, vol. 181, pp. 11–19, 2018, doi: 10.1016/j.jsbmb.2018.02.009.
[140] D. Ghosh *et al.*, “Novel aromatase inhibitors by structure-guided design.,” *J. Med. Chem.*, vol. 55, no. 19, pp. 8464–76, Oct. 2012, doi: 10.1021/jm300930n.
[141] W. Jiang and D. Ghosh, “Motion and Flexibility in Human Cytochrome P450 Aromatase,” *PLoS ONE*, vol. 7, no. 2, p. 32565, 2012, doi: 10.1371/journal.pone.0032565.
[142] W. J. Lu, Z. Desta, and D. A. Flockhart, “Tamoxifen metabolites as active inhibitors of aromatase in the treatment of breast cancer,” *Breast Cancer Res. Treat.*, 2012, doi: 10.1007/s10549-011-1428-z.
[143] A. Magistrato, J. Sgrignani, R. Krause, and A. Cavalli, “Single or Multiple Access Channels to the CYP450s Active Site? An Answer from Free Energy Simulations of the Human Aromatase Enzyme,” *J. Phys. Chem. Lett.*, vol. 8, no. 9, pp. 2036–2042, May 2017, doi: 10.1021/acs.jpclett.7b00697.
[144] L. C. Wienkers, “Problems associated with in vitro assessment of drug inhibition of CYP3A4 and other P-450 enzymes and its impact on drug discovery,” *J. Pharmacol. Toxicol. Methods*, vol. 45, no. 1, pp. 79–84, Feb. 2001, doi: 10.1016/s1056-8719(01)00121-6.

[145] D. G. Bailey, J. Malcolm, O. Arnold, and J. David Spence, “Grapefruit juice–drug interactions,” *Br. J. Clin. Pharmacol.*, vol. 46, no. 2, pp. 101–110, Aug. 1998, doi: 10.1046/j.1365-2125.1998.00764.x.
[146] K. Fujita, “Food-drug interactions via human cytochrome P450 3A (CYP3A).,” *Drug Metabol. Drug Interact.*, vol. 20, no. 4, pp. 195–217, 2004.
[147] L. Basheer and Z. Kerem, “Interactions between CYP3A4 and Dietary Polyphenols,” *Oxid. Med. Cell. Longev.*, vol. 2015, p. e854015, Jun. 2015, doi: 10.1155/2015/854015.
[148] T. Lynch and A. P. Neff, “The Effect of Cytochrome P450 Metabolism on Drug Response, Interactions, and Adverse Effects,” *Am. Fam. Physician*, vol. 76, no. 3, pp. 391–396, Aug. 2007.
[149] H. Fernando, D. R. Davydov, C. C. Chin, and J. R. Halpert, “Role of subunit interactions in P450 oligomers in the loss of homotropic cooperativity in the cytochrome P450 3A4 mutant L211F/D214E/F304W,” *Arch. Biochem. Biophys.*, vol. 460, no. 1, pp. 129–140, Apr. 2007, doi: 10.1016/J.ABB.2006.12.025.
[150] D. R. Davydov, N. Y. Davydova, E. V. Sineva, I. Kufareva, and J. R. Halpert, “Pivotal role of P450-P450 interactions in CYP3A4 allostery: the case of α-naphthoflavone.,” *Biochem. J.*, vol. 453, no. 2, pp. 219–30, 2013, doi: 10.1042/BJ20130398.
[151] H. Yamazaki, W. W. Johnson, Y. F. Ueng, T. Shimada, and F. P. Guengerich, “Lack of electron transfer from cytochrome b5 in stimulation of catalytic activities of cytochrome P450 3A4: Characterization of a reconstituted cytochrome P450 3A4/NADPH-cytochrome P450 reductase system and studies with apo-cytochrome b5,” *J. Biol. Chem.*, vol. 271, no. 44, pp. 27438–27444, 1996, doi: 10.1074/jbc.271.44.27438.
[152] M. Šrejber *et al.*, “Membrane-attached mammalian cytochromes P450: An overview of the membrane’s effects on structure, drug binding, and interactions with redox partners,” *J. Inorg. Biochem.*, vol. 183, pp. 117–136, Jun. 2018, doi: 10.1016/J.JINORGBIO.2018.03.002.
[153] C. Barnaba *et al.*, “Cytochrome-P450-Induced Ordering of Microsomal Membranes Modulates Affinity for Drugs,” *Angew. Chem. - Int. Ed.*, vol. 57, no. 13, pp. 3391–3395, Mar. 2018, doi: 10.1002/anie.201713167.
[154] C. Barnaba, K. Gentry, N. Sumangala, and A. Ramamoorthy, “The catalytic function of cytochrome P450 is entwined with its membrane-bound nature.,” *F1000Research*, vol. 6, p. 662, 2017, doi: 10.12688/f1000research.11015.1.
[155] J. Easterbrook, C. Lu, Y. Sakai, and A. P. Li, “Effects of organic solvents on the activities of cytochrome P450 isoforms, UDP-dependent glucuronyl transferase, and phenol sulfotransferase in human hepatocytes,” *Drug Metab. Dispos. Biol. Fate Chem.*, vol. 29, no. 2, pp. 141–144, Feb. 2001.
[156] M. Iwase, N. Kurata, R. Ehana, Y. Nishimura, T. Masamoto, and H. Yasuhara, “Evaluation of the effects of hydrophilic organic solvents on CYP3A-mediated drug-drug interaction in vitro,” *Hum. Exp. Toxicol.*, vol. 25, no. 12, pp. 715–721, Dec. 2006, doi: 10.1177/0960327106071979.
[157] I. Nobeli, A. D. Favia, and J. M. Thornton, “Protein promiscuity and its implications for biotechnology,” *Nat. Biotechnol.*, vol. 27, no. 2, pp. 157–167, Feb. 2009, doi: 10.1038/nbt1519.
[158] J. K. Yano, M. R. Wester, G. A. Schoch, K. J. Griffin, C. D. Stout, and E. F. Johnson, “The structure of human microsomal cytochrome P450 3A4 determined by X-ray

crystallography to 2.05-A resolution.," *J. Biol. Chem.*, vol. 279, no. 37, pp. 38091–4, Sep. 2004, doi: 10.1074/jbc.C400293200.

[159] E. E. Scott, M. A. White, Y. A. He, E. F. Johnson, C. D. Stout, and J. R. Halpert, "Structure of mammalian cytochrome P450 2B4 complexed with 4-(4-chlorophenyl)imidazole at 1.9-A resolution: insight into the range of P450 conformations and the coordination of redox partner binding," *J. Biol. Chem.*, vol. 279, no. 26, pp. 27294–27301, Jun. 2004, doi: 10.1074/JBC.M403349200.

[160] Y. Zhao, M. A. White, B. K. Muralidhara, L. Sun, J. R. Halpert, and C. D. Stout, "Structure of Microsomal Cytochrome P450 2B4 Complexed with the Antifungal Drug Bifonazole," *J. Biol. Chem.*, vol. 281, no. 9, pp. 5973–5981, Mar. 2006, doi: 10.1074/jbc.M511464200.

[161] J. C. Hackett, "Membrane-embedded substrate recognition by cytochrome P450 3A4.," *J. Biol. Chem.*, vol. 293, no. 11, pp. 4037–4046, Jan. 2018, doi: 10.1074/jbc.RA117.000961.

[162] D. R. Davydov, Z. Yang, N. Davydova, J. R. Halpert, and W. L. Hubbell, "Conformational Mobility in Cytochrome P450 3A4 Explored by Pressure-Perturbation EPR Spectroscopy," *Biophys. J.*, vol. 110, no. 7, pp. 1485–1498, Apr. 2016, doi: 10.1016/j.bpj.2016.02.026.

[163] M. Redhair, J. C. Hackett, R. D. Pelletier, and W. M. Atkins, "Dynamics and Location of the Allosteric Midazolam Site in Cytochrome P4503A4 in Lipid Nanodiscs," 2020, doi: 10.1021/acs.biochem.9b01001.

[164] H. Park, S. Lee, and J. Suh, "Structural and dynamical basis of broad substrate specificity, catalytic mechanism, and inhibition of cytochrome P450 3A4," *J. Am. Chem. Soc.*, vol. 127, no. 39, pp. 13634–13642, Oct. 2005, doi: 10.1021/JA053809Q/SUPPL_FILE/JA053809QSI20050804_013830.PDF.

[165] P. J. Mak, I. G. Denisov, Y. V. Grinkova, S. G. Sligar, and J. R. Kincaid, "Defining CYP3A4 Structural Responses to Substrate Binding. Raman Spectroscopic Studies of a Nanodisc-Incorporated Mammalian Cytochrome P450," *J. Am. Chem. Soc.*, vol. 133, no. 5, pp. 1357–1366, Feb. 2011, doi: 10.1021/ja105869p.

[166] K. D. Dubey and S. Shaik, "Cytochrome P450-The Wonderful Nanomachine Revealed through Dynamic Simulations of the Catalytic Cycle," *Acc. Chem. Res.*, vol. 52, no. 2, pp. 389–399, Feb. 2019, doi: 10.1021/ACS.ACCOUNTS.8B00467.

[167] L. Konermann, J. Pan, and Y.-H. Liu, "Hydrogen exchange mass spectrometry for studying protein structure and dynamics," *Chem Soc Rev*, vol. 40, no. 3, pp. 1224–1234, Feb. 2011, doi: 10.1039/C0CS00113A.

[168] G. R. Masson *et al.*, "Recommendations for performing, interpreting and reporting hydrogen deuterium exchange mass spectrometry (HDX-MS) experiments," *Nat. Methods*, vol. 16, no. 7, pp. 595–602, 2019, doi: 10.1038/s41592-019-0459-y.

[169] "Ritonavir | C37H48N6O5S2 - PubChem." https://pubchem.ncbi.nlm.nih.gov/compound/392622 (accessed Jan. 11, 2022).

[170] "Nifedipine | C17H18N2O6 - PubChem." https://pubchem.ncbi.nlm.nih.gov/compound/4485 (accessed Jan. 11, 2022).

[171] "Bromocriptine | C32H40BrN5O5 - PubChem." https://pubchem.ncbi.nlm.nih.gov/compound/31101 (accessed Jan. 11, 2022).

[172] "Miconazole | C18H14Cl4N2O - PubChem." https://pubchem.ncbi.nlm.nih.gov/compound/4189 (accessed Jan. 11, 2022).

[173] "Azamulin | C24H38N4O4S - PubChem." https://pubchem.ncbi.nlm.nih.gov/compound/16072188 (accessed Jan. 11, 2022).
[174] "Testosterone | C19H28O2 - PubChem." https://pubchem.ncbi.nlm.nih.gov/compound/6013 (accessed Jan. 11, 2022).
[175] C. M. Woods, C. Fernandez, K. L. Kunze, and W. M. Atkins, "Allosteric Activation of Cytochrome P450 3A4 by α-Naphthoflavone: Branch Point Regulation Revealed by Isotope Dilution Analysis," *Biochemistry*, vol. 50, no. 46, p. 10041, 2011, doi: 10.1021/BI2013454.
[176] B. J. Baas, I. G. Denisov, and S. G. Sligar, "Homotropic cooperativity of monomeric cytochrome P450 3A4 in a nanoscale native bilayer environment," *Arch. Biochem. Biophys.*, vol. 430, no. 2, pp. 218–228, 2004, doi: 10.1016/j.abb.2004.07.003.
[177] "Nanodisc Technology: Protocols for Preparation of Nanodiscs | Sligar Lab." https://publish.illinois.edu/sligar-lab/nanodisc-technology-protocols-for-preparation-of-nanodiscs/ (accessed Jan. 04, 2022).
[178] E. M. J. Gillam, T. Baba, B. R. Kim, S. Ohmori, and F. P. Guengerich, "Expression of modified human cytochrome P450 3A4 in Escherichia coli and purification and reconstitution of the enzyme," *Arch. Biochem. Biophys.*, vol. 305, no. 1, pp. 123–131, 1993, doi: 10.1006/ABBI.1993.1401.
[179] T. OMURA and R. SATO, "THE CARBON MONOXIDE-BINDING PIGMENT OF LIVER MICROSOMES. I. EVIDENCE FOR ITS HEMOPROTEIN NATURE.," *J. Biol. Chem.*, vol. 239, pp. 2370–8, Jul. 1964.
[180] † Timothy H. Bayburt, † and Yelena V. Grinkova, and † Stephen G. Sligar* ‡,§, "Self-Assembly of Discoidal Phospholipid Bilayer Nanoparticles with Membrane Scaffold Proteins," 2002, doi: 10.1021/NL025623K.
[181] C. M. Hebling, C. R. Morgan, D. W. Stafford, J. W. Jorgenson, K. D. Rand, and J. R. Engen, "Conformational analysis of membrane proteins in phospholipid bilayer nanodiscs by hydrogen exchange mass spectrometry," *Anal. Chem.*, vol. 82, no. 13, pp. 5415–5419, Jul. 2010, doi: 10.1021/AC100962C.
[182] T. A. Murphree, C. Vorauer, M. Brzoska, and M. Guttman, "Imidazolium Compounds as Internal Exchange Reporters for Hydrogen/Deuterium Exchange by Mass Spectrometry," *Anal. Chem.*, vol. 92, no. 14, pp. 9830–9837, Jul. 2020, doi: 10.1021/ACS.ANALCHEM.0C01328.
[183] M. Guttman, T. E. Wales, D. Whittington, J. R. Engen, J. M. Brown, and K. K. Lee, "Tuning a High Transmission Ion Guide to Prevent Gas-Phase Proton Exchange During H/D Exchange MS Analysis," *J. Am. Soc. Mass Spectrom.*, vol. 27, no. 4, pp. 662–668, Apr. 2016, doi: 10.1007/S13361-015-1330-8.
[184] M. Guttman, D. D. Weis, J. R. Engen, and K. K. Lee, "Analysis of overlapped and noisy hydrogen/deuterium exchange mass spectra," *J. Am. Soc. Mass Spectrom.*, vol. 24, no. 12, pp. 1906–1912, Dec. 2013, doi: 10.1007/s13361-013-0727-5.
[185] I. R. Möller *et al.*, "Conformational dynamics of the human serotonin transporter during substrate and drug binding," *Nat. Commun.*, vol. 10, no. 1, Dec. 2019, doi: 10.1038/S41467-019-09675-Z.
[186] D. Dai *et al.*, "Identification of Variants of CYP3A4 and Characterization of Their Abilities to Metabolize Testosterone and Chlorpyrifos." Accessed: Jun. 03, 2020. [Online]. Available: http://jpet.aspetjournals.org

[187] X.-Y. Zhou *et al.*, “Enzymatic Activities of CYP3A4 Allelic Variants on Quinine 3-Hydroxylation In Vitro,” *Front. Pharmacol.*, vol. 10, p. 591, May 2019, doi: 10.3389/fphar.2019.00591.
[188] I. F. Sevrioukova, “High-Level Production and Properties of the Cysteine-Depleted Cytochrome P450 3A4,” *Biochemistry*, vol. 56, no. 24, pp. 3058–3067, Jun. 2017, doi: 10.1021/ACS.BIOCHEM.7B00334.
[189] E. Prade *et al.*, “A Minimal Functional Complex of Cytochrome P450 and FBD of Cytochrome P450 Reductase in Nanodiscs,” *Angew. Chem. Int. Ed Engl.*, vol. 57, no. 28, pp. 8458–8462, Jul. 2018, doi: 10.1002/ANIE.201802210.
[190] B. Wen, J. N. Lampe, A. G. Roberts, W. M. Atkins, A. David Rodrigues, and S. D. Nelson, “Cysteine 98 in CYP3A4 Contributes to Conformational Integrity Required for P450 Interaction with CYP Reductase,” *Arch. Biochem. Biophys.*, vol. 454, no. 1, p. 42, Oct. 2006, doi: 10.1016/J.ABB.2006.08.003.
[191] D. F. Estrada, J. S. Laurence, and E. E. Scott, “Substrate-modulated cytochrome P450 17A1 and cytochrome b5 interactions revealed by NMR,” *J. Biol. Chem.*, vol. 288, no. 23, pp. 17008–17018, Jun. 2013, doi: 10.1074/jbc.M113.468926.
[192] D. F. Estrada, J. S. Laurence, and E. E. Scott, “Cytochrome P450 17A1 Interactions with the FMN Domain of Its Reductase as Characterized by NMR,” *J. Biol. Chem.*, vol. 291, no. 8, pp. 3990–4003, Feb. 2016, doi: 10.1074/JBC.M115.677294.
[193] I. Ritacco, A. Spinello, E. Ippoliti, and A. Magistrato, “Post-Translational Regulation of CYP450s Metabolism As Revealed by All-Atoms Simulations of the Aromatase Enzyme,” *J. Chem. Inf. Model.*, vol. 59, no. 6, pp. 2930–2940, Jun. 2019, doi: 10.1021/ACS.JCIM.9B00157.
[194] G. Mukherjee, P. P. Nandekar, and R. C. Wade, “An electron transfer competent structural ensemble of membrane-bound cytochrome P450 1A1 and cytochrome P450 oxidoreductase,” *Commun. Biol.*, vol. 4, no. 1, Dec. 2021, doi: 10.1038/S42003-020-01568-Y.
[195] T. Shimizu, T. Tateishi, M. Hatano, and Y. Fujii-Kuriyama, “Probing the role of lysines and arginines in the catalytic function of cytochrome P450d by site-directed mutagenesis. Interaction with NADPH-cytochrome P450 reductase,” *J. Biol. Chem.*, vol. 266, no. 6, pp. 3372–3375, Feb. 1991, doi: 10.1016/S0021-9258(19)67801-4.
[196] C. Kenaan, H. Zhang, E. V. Shea, and P. F. Hollenberg, “Uncovering the role of hydrophobic residues in cytochrome P450-cytochrome P450 reductase interactions,” *Biochemistry*, vol. 50, no. 19, pp. 3957–3967, May 2011, doi: 10.1021/BI1020748.
[197] K. A. Gentry, G. M. Anantharamaiah, and A. Ramamoorthy, “Probing protein-protein and protein-substrate interactions in the dynamic membrane-associated ternary complex of cytochromes P450,: B 5, and reductase,” *Chem. Commun.*, vol. 55, no. 89, pp. 13422–13425, 2019, doi: 10.1039/c9cc05904k.
[198] N. N. Bumpus and P. F. Hollenberg, “Cross-linking of human cytochrome P450 2B6 to NADPH-cytochrome P450 reductase: Identification of a potential site of interaction,” *J. Inorg. Biochem.*, vol. 104, no. 4, pp. 485–488, Apr. 2010, doi: 10.1016/J.JINORGBIO.2009.12.017.
[199] I. F. Sevrioukova, “Structural Insights into the Interaction of Cytochrome P450 3A4 with Suicide Substrates: Mibefradil, Azamulin and 6’,7’-Dihydroxybergamottin,” *Int. J. Mol. Sci.*, vol. 20, no. 17, Sep. 2019, doi: 10.3390/IJMS20174245.

[200] I. F. Sevrioukova and T. L. Poulos, “Structural and Mechanistic Insights into the Interaction of Cytochrome P4503A4 with Bromoergocryptine, a Type I Ligand,” *J. Biol. Chem.*, vol. 287, no. 5, p. 3510, Jan. 2012, doi: 10.1074/JBC.M111.317081.
[201] N. Skar-Gislinge *et al.*, “Small-angle scattering determination of the shape and localization of human cytochrome P450 embedded in a phospholipid nanodisc environment”, doi: 10.1107/S1399004715018702.
[202] K. Berka, M. Paloncýová, P. Anzenbacher, and M. Otyepka, “Behavior of human cytochromes P450 on lipid membranes,” *J. Phys. Chem. B*, vol. 117, no. 39, pp. 11556–11564, Oct. 2013, doi: 10.1021/JP4059559.
[203] W. D. McClary, J. P. Sumida, M. Scian, L. Paço, and W. M. Atkins, “Membrane Fluidity Modulates Thermal Stability and Ligand Binding of Cytochrome P4503A4 in Lipid Nanodiscs,” *Biochemistry*, vol. 55, no. 45, pp. 6258–6268, Nov. 2016, doi: 10.1021/acs.biochem.6b00715.
[204] M. J. Chalmers, S. A. Busby, B. D. Pascal, G. M. West, and P. R. Griffin, “Differential hydrogen/deuterium exchange mass spectrometry analysis of protein–ligand interactions,” *Expert Rev. Proteomics*, vol. 8, no. 1, p. 43, Feb. 2011, doi: 10.1586/EPR.10.109.
[205] C. S. Ernest, S. D. Hall, and D. R. Jones, “Mechanism-Based Inactivation of CYP3A by HIV Protease Inhibitors,” *J. Pharmacol. Exp. Ther.*, vol. 312, no. 2, pp. 583–591, Feb. 2005, doi: 10.1124/JPET.104.075416.
[206] K. E. Kenworthy, S. E. Clarke, J. Andrews, and J. B. Houston, “Multisite Kinetic Models for Cyp3a4 : Simultaneous Activation and Inhibition of Diazepam and Testosterone Metabolism Abstract :,” *Drug Metab. Dispos.*, vol. 29, no. 12, pp. 1644–1651, 2001.
[207] A. Nath, Y. V. Grinkova, S. G. Sligar, and W. M. Atkins, “Ligand binding to cytochrome P450 3A4 in phospholipid bilayer nanodiscs: the effect of model membranes.,” *J. Biol. Chem.*, vol. 282, no. 39, pp. 28309–20, Sep. 2007, doi: 10.1074/jbc.M703568200.
[208] S. Rendic, “Summary of information on human CYP enzymes: human P450 metabolism data,” *Drug Metab. Rev.*, vol. 34, no. 1–2, pp. 83–448, May 2002, doi: 10.1081/dmr-120001392.
[209] S. Rendic and F. P. Guengerich, “Survey of Human Oxidoreductases and Cytochrome P450 Enzymes Involved in the Metabolism of Xenobiotic and Natural Chemicals,” *Chem. Res. Toxicol.*, vol. 28, no. 1, pp. 38–42, Jan. 2015, doi: 10.1021/TX500444E.
[210] A. Fischer and M. Smieško, “Spontaneous Ligand Access Events to Membrane-Bound Cytochrome P450 2D6 Sampled at Atomic Resolution,” *Sci. Rep.*, vol. 9, no. 1, Dec. 2019, doi: 10.1038/S41598-019-52681-W.
[211] K. J. Ryan, “Conversion of androstenedione to estrone by placental microsomes,” *Biochim. Biophys. Acta*, vol. 27, no. 3, pp. 658–659, 1958, doi: 10.1016/0006-3002(58)90408-6.
[212] E. A. Thompson and P. K. Siiteri, “Utilization of oxygen and reduced nicotinamide adenine dinucleotide phosphate by human placental microsomes during aromatization of androstenedione,” *J. Biol. Chem.*, vol. 249, no. 17, pp. 5364–5372, Sep. 1974.
[213] H. J. Brodie, K. J. Kripalani, and G. Possanza, “Mechanism of estrogen biosynthesis. VI. The stereochemistry of hydrogen elimination at C-2 during aromatization,” *J. Am. Chem. Soc.*, vol. 91, no. 5, pp. 1241–1242, Feb. 1969, doi: 10.1021/ja01033a050.
[214] J. D. Townsley and H. J. Brodie, “Mechanism of estrogenbiosynthesis. III. Stereochemistry of aromatization of C19 and C18 steroids,” *Biochemistry*, vol. 7, no. 1, pp. 33–40, Jan. 1968, doi: 10.1021/bi00841a005.

[215] E. di Salle, G. Ornati, D. Giudici, M. Lassus, T. R. Evans, and R. C. Coombes, "Exemestane (FCE 24304), a new steroidal aromatase inhibitor," *J. Steroid Biochem. Mol. Biol.*, vol. 43, no. 1–3, pp. 137–143, Sep. 1992, doi: 10.1016/0960-0760(92)90198-r.
[216] R. W. Brueggemeier, J. C. Hackett, and E. S. Diaz-Cruz, "Aromatase inhibitors in the treatment of breast cancer," *Endocr. Rev.*, vol. 26, no. 3, pp. 331–345, May 2005, doi: 10.1210/er.2004-0015.
[217] R. J. Santen, H. Brodie, E. R. Simpson, P. K. Siiteri, and A. Brodie, "History of aromatase: saga of an important biological mediator and therapeutic target," *Endocr. Rev.*, vol. 30, no. 4, pp. 343–375, Jun. 2009, doi: 10.1210/er.2008-0016.
[218] A. U. Buzdar, W. Jonat, A. Howell, and P. V. Plourde, "ARIMIDEX: a potent and selective aromatase inhibitor for the treatment of advanced breast cancer," *J. Steroid Biochem. Mol. Biol.*, vol. 61, no. 3–6, pp. 145–149, Apr. 1997.
[219] S. E. Bulun *et al.*, "Aromatase in endometriosis and uterine leiomyomata," *J. Steroid Biochem. Mol. Biol.*, vol. 95, no. 1–5, pp. 57–62, May 2005, doi: 10.1016/j.jsbmb.2005.04.012.
[220] R. Słopień and B. Męczekalski, "Aromatase inhibitors in the treatment of endometriosis," *Menopause Rev. Menopauzalny*, vol. 15, no. 1, pp. 43–47, 2016, doi: 10.5114/pm.2016.58773.
[221] B. Usluogullari, C. Duvan, and C. Usluogullari, "Use of aromatase inhibitors in practice of gynecology," *J. Ovarian Res.*, vol. 8, p. 4, Feb. 2015, doi: 10.1186/s13048-015-0131-9.
[222] M. Ciebiera *et al.*, "Alternative Oral Agents in Prophylaxis and Therapy of Uterine Fibroids—An Up-to-Date Review," *Int. J. Mol. Sci.*, vol. 18, no. 12, Art. no. 12, Dec. 2017, doi: 10.3390/ijms18122586.
[223] R. S. Legro, "Ovulation induction in polycystic ovary syndrome: Current options," *Best Pract. Res. Clin. Obstet. Gynaecol.*, vol. 37, pp. 152–159, Nov. 2016, doi: 10.1016/j.bpobgyn.2016.08.001.
[224] M. A. Ribeiro *et al.*, "Aromatase inhibitors in the treatment of oligozoospermic or azoospermic men: a systematic review of randomized controlled trials," *JBRA Assist. Reprod.*, vol. 20, no. 2, pp. 82–88, May 2016, doi: 10.5935/1518-0557.20160019.
[225] A. Kawashima and Y. Satta, "Substrate-dependent evolution of cytochrome P450: rapid turnover of the detoxification-type and conservation of the biosynthesis-type," *PloS One*, vol. 9, no. 6, p. e100059, 2014, doi: 10.1371/journal.pone.0100059.
[226] A. Bar-Even *et al.*, "The Moderately Efficient Enzyme: Evolutionary and Physicochemical Trends Shaping Enzyme Parameters," *Biochemistry*, vol. 50, no. 21, pp. 4402–4410, May 2011, doi: 10.1021/bi2002289.
[227] N. Skar-Gislinge *et al.*, "Elliptical Structure of Phospholipid Bilayer Nanodiscs Encapsulated by Scaffold Proteins: Casting the Roles of the Lipids and the Protein," *J. Am. Chem. Soc.*, vol. 132, no. 39, pp. 13713–13722, Oct. 2010, doi: 10.1021/ja1030613.
[228] F. Zárate-Pérez and J. C. Hackett, "Conformational selection is present in ligand binding to cytochrome P450 19A1 lipoprotein nanodiscs," *J. Inorg. Biochem.*, vol. 209, p. 111120, Aug. 2020, doi: 10.1016/j.jinorgbio.2020.111120.
[229] N. Kagawa, H. Hori, M. R. Waterman, and S. Yoshioka, "Characterization of stable human aromatase expressed in E. coli," *Steroids*, vol. 69, no. 4, pp. 235–243, Apr. 2004, doi: 10.1016/j.steroids.2004.01.002.

[230] M. Redhair, J. C. Hackett, R. D. Pelletier, and W. M. Atkins, "Dynamics and Location of the Allosteric Midazolam Site in Cytochrome P4503A4 in Lipid Nanodiscs," *Biochemistry*, vol. 59, no. 6, pp. 766–779, Feb. 2020, doi: 10.1021/acs.biochem.9b01001.

[231] R. J. Chalkley *et al.*, "Comprehensive analysis of a multidimensional liquid chromatography mass spectrometry dataset acquired on a quadrupole selecting, quadrupole collision cell, time-of-flight mass spectrometer: II. New developments in Protein Prospector allow for reliable and comprehensive automatic analysis of large datasets," *Mol. Cell. Proteomics MCP*, vol. 4, no. 8, pp. 1194–1204, Aug. 2005, doi: 10.1074/mcp.D500002-MCP200.

[232] D. D. Weis, J. R. Engen, and I. J. Kass, "Semi-automated data processing of hydrogen exchange mass spectra using HX-Express," *J. Am. Soc. Mass Spectrom.*, vol. 17, no. 12, pp. 1700–1703, Dec. 2006, doi: 10.1016/j.jasms.2006.07.025.

[233] M. H. M. Olsson, C. R. Søndergaard, M. Rostkowski, and J. H. Jensen, "PROPKA3: Consistent Treatment of Internal and Surface Residues in Empirical pKa Predictions," *J. Chem. Theory Comput.*, vol. 7, no. 2, pp. 525–537, Feb. 2011, doi: 10.1021/ct100578z.

[234] M. A. Lomize, I. D. Pogozheva, H. Joo, H. I. Mosberg, and A. L. Lomize, "OPM database and PPM web server: resources for positioning of proteins in membranes," *Nucleic Acids Res.*, vol. 40, no. Database issue, pp. D370-376, Jan. 2012, doi: 10.1093/nar/gkr703.

[235] K. Sen and J. C. Hackett, "Coupled Electron Transfer and Proton Hopping in the Final Step of CYP19-Catalyzed Androgen Aromatization," *Biochemistry*, vol. 51, no. 14, pp. 3039–3049, Apr. 2012, doi: 10.1021/bi300017p.

[236] J. Comer, J. C. Gumbart, J. Hénin, T. Lelièvre, A. Pohorille, and C. Chipot, "The Adaptive Biasing Force Method: Everything You Always Wanted To Know but Were Afraid To Ask," *J. Phys. Chem. B*, vol. 119, no. 3, pp. 1129–1151, Jan. 2015, doi: 10.1021/jp506633n.

[237] G. Di Nardo *et al.*, "Evidence for an elevated aspartate pK(a) in the active site of human aromatase," *J. Biol. Chem.*, vol. 290, no. 2, pp. 1186–1196, Jan. 2015, doi: 10.1074/jbc.M114.595108.

[238] J. Lo *et al.*, "Structural basis for the functional roles of critical residues in human cytochrome p450 aromatase," *Biochemistry*, vol. 52, no. 34, pp. 5821–5829, Aug. 2013, doi: 10.1021/bi400669h.

[239] D. D. Weis, T. E. Wales, J. R. Engen, M. Hotchko, and L. F. Ten Eyck, "Identification and Characterization of EX1 Kinetics in H/D Exchange Mass Spectrometry by Peak Width Analysis," *J. Am. Soc. Mass Spectrom.*, vol. 17, no. 11, pp. 1498–1509, Nov. 2006, doi: 10.1016/j.jasms.2006.05.014.

[240] H. Xiao *et al.*, "Mapping protein energy landscapes with amide hydrogen exchange and mass spectrometry: I. A generalized model for a two-state protein and comparison with experiment," *Protein Sci. Publ. Protein Soc.*, vol. 14, no. 2, pp. 543–557, Feb. 2005, doi: 10.1110/ps.041001705.

[241] Y. Miao, V. A. Feher, and J. A. McCammon, "Gaussian Accelerated Molecular Dynamics: Unconstrained Enhanced Sampling and Free Energy Calculation," *J. Chem. Theory Comput.*, vol. 11, no. 8, pp. 3584–3595, Aug. 2015, doi: 10.1021/acs.jctc.5b00436.

[242] Y. Wang, P. R. L. Markwick, C. A. F. de Oliveira, and J. A. McCammon, "Enhanced Lipid Diffusion and Mixing in Accelerated Molecular Dynamics," *J. Chem. Theory Comput.*, vol. 7, no. 10, pp. 3199–3207, Oct. 2011, doi: 10.1021/ct200430c.

[243] P. J. Winn, S. K. Ludemann, R. Gauges, V. Lounnas, and R. C. Wade, “Comparison of the dynamics of substrate access channels in three cytochrome P450s reveals different opening mechanisms and a novel functional role for a buried arginine,” *Proc. Natl. Acad. Sci.*, vol. 99, no. 8, pp. 5361–5366, Apr. 2002, doi: 10.1073/pnas.082522999.

[244] V. Cojocaru, P. J. Winn, and R. C. Wade, “Multiple, ligand-dependent routes from the active site of cytochrome P450 2C9,” *Curr. Drug Metab.*, vol. 13, no. 2, pp. 143–154, Feb. 2012, doi: 10.2174/138920012798918462.

[245] S. K. Lüdemann, V. Lounnas, and R. C. Wade, “How do substrates enter and products exit the buried active site of cytochrome P450cam? 1. Random expulsion molecular dynamics investigation of ligand access channels and mechanisms,” *J. Mol. Biol.*, vol. 303, no. 5, pp. 797–811, Nov. 2000, doi: 10.1006/jmbi.2000.4154.

[246] R. G. McAllister and L. Konermann, “Challenges in the interpretation of protein H/D exchange data: A molecular dynamics simulation perspective,” *Biochemistry*, vol. 54, no. 16, pp. 2683–2692, Apr. 2015, doi: 10.1021/ACS.BIOCHEM.5B00215.

[247] S. W. Englander and N. R. Kallenbach, “Hydrogen exchange and structural dynamics of proteins and nucleic acids,” *Q. Rev. Biophys.*, vol. 16, no. 4, pp. 521–655, Nov. 1983, doi: 10.1017/s0033583500005217.

[248] B. F. Shaw *et al.*, “Neutralizing positive charges at the surface of a protein lowers its rate of amide hydrogen exchange without altering its structure or increasing its thermostability,” *J. Am. Chem. Soc.*, vol. 132, no. 49, pp. 17411–17425, Dec. 2010, doi: 10.1021/JA9067035.

[249] N. Mast, M. A. White, I. Bjorkhem, E. F. Johnson, C. D. Stout, and I. A. Pikuleva, “Crystal structures of substrate-bound and substrate-free cytochrome P450 46A1, the principal cholesterol hydroxylase in the brain,” *Proc. Natl. Acad. Sci. U. S. A.*, vol. 105, no. 28, pp. 9546–9551, Jul. 2008, doi: 10.1073/pnas.0803717105.

[250] N. Mast, A. J. Annalora, D. T. Lodowski, K. Palczewski, C. D. Stout, and I. A. Pikuleva, “Structural basis for three-step sequential catalysis by the cholesterol side chain cleavage enzyme CYP11A1,” *J. Biol. Chem.*, vol. 286, no. 7, pp. 5607–5613, Feb. 2011, doi: 10.1074/jbc.M110.188433.

[251] N. Strushkevich, F. MacKenzie, T. Cherkesova, I. Grabovec, S. Usanov, and H.-W. Park, “Structural basis for pregnenolone biosynthesis by the mitochondrial monooxygenase system,” *Proc. Natl. Acad. Sci. U. S. A.*, vol. 108, no. 25, pp. 10139–10143, Jun. 2011, doi: 10.1073/pnas.1019441108.

[252] C. Fusi *et al.*, “Steroidal and non-steroidal third-generation aromatase inhibitors induce pain-like symptoms via TRPA1,” *Nat. Commun.*, vol. 5, no. 1, Art. no. 1, Dec. 2014, doi: 10.1038/ncomms6736.

[253] Y. Hong, B. Yu, M. Sherman, Y.-C. Yuan, D. Zhou, and S. Chen, “Molecular Basis for the Aromatization Reaction and Exemestane-Mediated Irreversible Inhibition of Human Aromatase,” 2007, doi: 10.1210/me.2006-0281.

[254] H. T. Mouridsen, “Incidence and management of side effects associated with aromatase inhibitors in the adjuvant treatment of breast cancer in postmenopausal women,” *Curr. Med. Res. Opin.*, vol. 22, no. 8, pp. 1609–1621, Aug. 2006, doi: 10.1185/030079906X115667.

[255] C. Connor and D. Attai, “Adjuvant Endocrine Therapy for the Surgeon: Options, Side Effects, and their Management,” *Ann. Surg. Oncol.*, vol. 20, no. 10, pp. 3188–3193, Oct. 2013, doi: 10.1245/s10434-013-3177-1.

[256] A.-R. Ibrahim and Y. J. Abul-Hajj, “Aromatase inhibition by flavonoids,” *J. Steroid Biochem. Mol. Biol.*, vol. 37, no. 2, pp. 257–260, Oct. 1990, doi: 10.1016/0960-0760(90)90335-I.

[257] J. T. Kellis and L. E. Vickery, “Inhibition of Human Estrogen Synthetase (Aromatase) by Flavones,” *Science*, vol. 225, no. 4666, pp. 1032–1034, Sep. 1984, doi: 10.1126/science.6474163.

[258] U. Shah *et al.*, “Role of Natural and Synthetic Flavonoids as Potential Aromatase Inhibitors in Breast Cancer: Structure-Activity Relationship Perspective,” *Anticancer Agents Med. Chem.*, Oct. 2021, doi: 10.2174/1871520621666211026101252.

[259] N. Suvannang, C. Nantasenamat, C. Isarankura-Na-Ayudhya, and V. Prachayasittikul, “Molecular Docking of Aromatase Inhibitors,” *Molecules*, vol. 16, no. 5, pp. 3597–3617, Apr. 2011, doi: 10.3390/molecules16053597.

[260] J. Park, L. Czapla, and R. E. Amaro, “Molecular Simulations of Aromatase Reveal New Insights Into the Mechanism of Ligand Binding,” *J. Chem. Inf. Model.*, vol. 53, no. 8, pp. 2047–2056, Aug. 2013, doi: 10.1021/ci400225w.

[261] J. Sgrignani and A. Magistrato, “Influence of the membrane lipophilic environment on the structure and on the substrate access/egress routes of the human aromatase enzyme. A computational study,” *J. Chem. Inf. Model.*, vol. 52, no. 6, pp. 1595–1606, Jun. 2012, doi: 10.1021/ci300151h.

[262] I. Hubatsch, M. Ridderström, and B. Mannervik, “Human glutathione transferase A4-4: an alpha class enzyme with high catalytic efficiency in the conjugation of 4-hydroxynonenal and other genotoxic products of lipid peroxidation.,” *Biochem. J.*, vol. 330 (Pt 1), no. Pt 1, pp. 175–9, Feb. 1998.

[263] R. M. LoPachin, T. Gavin, D. R. Petersen, and D. S. Barber, “Molecular mechanisms of 4-hydroxy-2-nonenal and acrolein toxicity: nucleophilic targets and adduct formation,” *Chem. Res. Toxicol.*, vol. 22, no. 9, pp. 1499–1508, Sep. 2009, doi: 10.1021/tx900147g.

[264] M. Csala *et al.*, “On the role of 4-hydroxynonenal in health and disease,” 2015, doi: 10.1016/j.bbadis.2015.01.015.

[265] R. J. Schaur, W. Siems, N. Bresgen, and P. M. Eckl, “4-Hydroxy-nonenal-A Bioactive Lipid Peroxidation Product,” *Biomolecules*, vol. 5, no. 4, pp. 2247–2337, Sep. 2015, doi: 10.3390/biom5042247.

[266] H. J. Forman, J. M. Fukuto, T. Miller, H. Zhang, A. Rinna, and S. Levy, “The chemistry of cell signaling by reactive oxygen and nitrogen species and 4-hydroxynonenal,” *Arch. Biochem. Biophys.*, vol. 477, no. 2, pp. 183–195, Sep. 2008, doi: 10.1016/j.abb.2008.06.011.

[267] Y. C. Awasthi *et al.*, “Regulation of 4-hydroxynonenal-mediated signaling by glutathione S-transferases,” *Free Radic. Biol. Med.*, vol. 37, no. 5, pp. 607–619, Sep. 2004, doi: 10.1016/J.FREERADBIOMED.2004.05.033.

[268] S. Someya and M. J. Kim, “Cochlear detoxification: Role of alpha class glutathione transferases in protection against oxidative lipid damage, ototoxicity, and cochlear aging,” *Hear. Res.*, vol. 402, Mar. 2021, doi: 10.1016/J.HEARES.2020.108002.

[269] J. Chen and R. N. Armstrong, “Stereoselective catalysis of a retro-Michael reaction by class mu glutathione transferases. Consequences for the internal distribution of products in the active site.,” *Chem. Res. Toxicol.*, vol. 8, no. 4, pp. 580–5, Jun. 1995.

[270] F. A. Armstrong and J. Hirst, “Reversibility and efficiency in electrocatalytic energy conversion and lessons from enzymes,” *Proc. Natl. Acad. Sci.*, vol. 108, no. 34, pp. 14049–14054, Aug. 2011, doi: 10.1073/pnas.1103697108.

[271] J. Alary, Y. Fernandez, L. Debrauwer, E. Perdu, and F. Guéraud, “Identification of Intermediate Pathways of 4-Hydroxynonenal Metabolism in the Rat”, doi: 10.1021/tx025671k.

[272] P. G. Board, “Identification of cDNAs encoding two human alpha class glutathione transferases (GSTA3 and GSTA4) and the heterologous expression of GSTA4-4.,” *Biochem. J.*, vol. 330, no. Pt 2, pp. 827–831, Mar. 1998.

[273] C. A. Ibarra, P. Chowdhury, J. W. Petrich, and W. M. Atkins, “The anomalous pKa of Tyr-9 in glutathione S-transferase A1-1 catalyzes product release.,” *J. Biol. Chem.*, vol. 278, no. 21, pp. 19257–65, May 2003, doi: 10.1074/jbc.M301566200.

[274] I. Hubatsch and B. Mannervik, “A Highly Acidic Tyrosine 9 and a Normally Titrating Tyrosine 212 Contribute to the Catalytic Mechanism of Human Glutathione Transferase A4-4,” *Biochem. Biophys. Res. Commun.*, vol. 280, no. 3, pp. 878–882, Jan. 2001, doi: 10.1006/bbrc.2000.4230.

[275] W. H. Habig, M. J. Pabst, and W. B. Jakoby, “Glutathione S-Transferases: THE FIRST ENZYMATIC STEP IN MERCAPTURIC ACID FORMATION,” *J. Biol. Chem.*, vol. 249, no. 22, pp. 7130–7139, Nov. 1974, doi: 10.1016/S0021-9258(19)42083-8.

[276] P. J. Hajduk, E. T. Olejniczak, and S. W. Fesik, “One-Dimensional Relaxation- and Diffusion-Edited NMR Methods for Screening Compounds That Bind to Macromolecules,” *J. Am. Chem. Soc.*, vol. 119, no. 50, pp. 12257–12261, Dec. 1997, doi: 10.1021/ja9715962.

[277] L. O. Nilsson, A. Gustafsson, and B. Mannervik, “Redesign of substrate-selectivity determining modules of glutathione transferase A1-1 installs high catalytic efficiency with toxic alkenal products of lipid peroxidation,” *Proc. Natl. Acad. Sci. U. S. A.*, vol. 97, no. 17, pp. 9408–9412, Aug. 2000, doi: 10.1073/pnas.150084897.

VITA

[A short bio of the author is required for a Ph.D. dissertation at the University of Washington. The vita section does not go into the Table of Contents. The formatting style follows the text of the dissertation.]